

# UNIVERSITÀ DEGLI STUDI DI MILANO

Department of Bioscience

PhD course in Molecular and Cellular Biology

XXXIII Cycle



***Guanylate Cyclase Activating Protein 1 monomer-dimer  
equilibrium controlled by  $Ca^{2+}$  or  $Mg^{2+}$  binding:  
hints to understand retinal Guanylate Cyclase regulation***

Francesco Bonì

PhD Thesis

Tutor: Dr. Mario Milani

Co-tutor: Prof. Martino Bolognesi

Academic year: 2020 - 2021



<b>UNIVERSITÀ DEGLI STUDI DI MILANO .....</b>	<b>1</b>
<b>ABSTRACT.....</b>	<b>5</b>
<b>RIASSUNTO.....</b>	<b>7</b>
<b>1. INTRODUCTION.....</b>	<b>9</b>
1.1 NEURONAL CALCIUM-SENSOR PROTEINS .....	9
1.2 THE EF-HAND MOTIF .....	11
1.3 PHOTOTRANSDUCTION.....	12
1.4 GUANYLATE CYCLASE ACTIVATING PROTEIN 1 (GCAP1) .....	14
1.5 GCAPs QUATERNARY ASSEMBLY .....	16
1.6 GCAP1 PATHOLOGICAL MUTANTS: THE CONE DYSFUNCTION SYNDROMES .....	16
<b>2. AIM OF THE PROJECT.....</b>	<b>19</b>
<b>3. RESULTS AND DISCUSSION .....</b>	<b>21</b>
3.1 HGCAP1 EXPRESSION AND PURIFICATION IN A SOLUBLE FORM.....	21
3.1.1 ION EXCHANGE CHROMATOGRAPHY.....	21
3.1.2 SIZE EXCLUSION CHROMATOGRAPHY .....	22
3.2 CIRCULAR DICHROISM ANALYSIS: ASSESSING THE PROTEIN SECONDARY STRUCTURE .....	24
3.3 FROM DIMER TO MONOMER: THE ANALYTIC SEC APPROACH .....	25
3.4 FROM MONOMER TO DIMER: THE MST APPROACH .....	30
3.5 CHICKEN GCAP1: AN EVOLUTIONARY CONSERVED MONOMER-DIMER EQUILIBRIUM .....	32
3.6 GCAP1 DIMERIZATION IS AFFECTED BY IONIC STRENGTH.....	36
3.7 CRYSTALLIZATION TRIALS OF THE HUMAN AND CHICKEN GCAP1: AN ENGINEERED CONSTRUCT.....	42
3.7.1 FULL LENGTH GCAP1.....	42
3.7.2 LIMITED PROTEOLYSIS: A STABLE FRAGMENT OF HGCAP1 .....	44
3.7.3 GCAP1 WT $\Delta$ 12 Q58C/A118C: STABILIZATION OF GCAP1 WITH A DISULFIDE BRIDGE .....	46
3.8 SMALL ANGLE X-RAY SCATTERING (SAXS): A LOW-RESOLUTION MODEL OF THE HGCAP1 DIMERIC ASSEMBLY	49
3.9 RETINAL GUANYLATE CYCLASE 1: EFFORTS TO PRODUCE THE RETGC1/GCAP1 COMPLEX .....	50
3.10 IDENTIFICATION OF EF1-TARGETED COMPOUNDS: A PRELIMINARY SCREENING .....	55

<b>4. CONCLUSIONS AND FUTURE PERSPECTIVES.....</b>	<b>60</b>
<b>5. MATERIALS AND METHODS .....</b>	<b>64</b>
5.1 PLASMIDS FOR EXPRESSION OF MYRISTOYLATED GCAP1 IN <i>E. COLI</i> :.....	64
5.2 SITE DIRECTED MUTAGENESIS (SDM).....	66
5.3 GCAP1 EXPRESSION AND PURIFICATION.....	68
5.3.1 CELL LYSIS .....	68
5.3.2 ION EXCHANGE CHROMATOGRAPHY .....	69
5.3.3 SIZE EXCLUSION CHROMATOGRAPHY .....	69
5.3.4 ANALYTIC SIZE EXCLUSION CHROMATOGRAPHY .....	69
5.4 SEC-MALS.....	70
5.5 TRYPSIN MEDIATED LIMITED PROTEOLYSIS.....	71
5.6 CHEMICAL CROSS-LINKING .....	71
5.7 SECOND HARMONIC GENERATION (SHG).....	71
5.8 CRYSTALLIZATION TRIALS .....	72
5.9 RECOMBINANT BACULOVIRUS PRODUCTION FOR THE EXPRESSION OF THE CYTOPLASMIC DOMAIN OF RETINAL GUANYLATE CYCLASE .....	73
<b>REFERENCES .....</b>	<b>77</b>
<b>INTRODUCTION TO PAPER 1.....</b>	<b>80</b>
<b>INTRODUCTION TO PAPER 2.....</b>	<b>81</b>

# Abstract

Neuronal calcium sensors play a crucial role in different pathways of  $\text{Ca}^{2+}$ -mediated neurotransmission. Among them guanylate cyclase-activating protein 1 (GCAP1) is expressed only in photoreceptors and activates or inhibits retinal guanylate cyclase 1 (retGC1) depending on cellular  $\text{Ca}^{2+}$  concentrations during phototransduction. To date, 22 pathogenic mutations responsible for retinal dystrophy have been associated to GCAP1, but a complete picture of the molecular determinants of the disease is still missing. The only crystal structure available so far is the *wt*  $\text{Ca}^{2+}$ -bound monomeric homologue from chicken and no cure exists for retinal dystrophy.

In this work I report for the first time that the recombinant human GCAP1 is characterized by a highly dynamic monomer-dimer equilibrium, whose dissociation constant is influenced by salt concentration and by the nature of the divalent ion bound. Surprisingly, I discovered that also the chicken protein shows a similar mechanism, suggesting that this property could be potentially functional for GCAP1 activity and conserved among different species. Despite the large number of crystallization trials, no diffracting crystal of the human GCAP1 was obtained, probably due to the flexible C-terminal tail and the intrinsic dynamicity of the protein. To overcome this issue, I produced a construct lacking the 12 C-term residues and stabilized by a disulfide bridge between the N- and C-term domains which was successfully crystallized. We showed that such engineered construct is able to regulate retGC1 as well as the *wt* protein.

By combining SAXS, protein-protein docking and molecular dynamics simulation we propose two novel three-dimensional models of  $\text{Ca}^{2+}$ -bound GCAP1 dimer which are stabilized by some of the residues involved in the interaction with the retGC1.

We used a biophysical and biochemical approach to thoroughly investigate three pathogenic variants (D100G, E155A and E155G) characterized by mutations in residues directly involved in  $\text{Ca}^{2+}$ -coordination. All the three variants were able to form oligomers in solutions, showing a decreased affinity for  $\text{Ca}^{2+}$  and constitutively activating retGC1 at physiological calcium concentrations. Besides local structural effects, the mutations perturb also the oligomeric state of GCAP1 suggesting that the multimeric assembly of the protein could affect its proper biological function.

A recombinant baculovirus for the expression of the cytoplasmic domain of retGC1 in insect cells was produced with the aim to get atomic structural information on the GCAP1/retGC1

complex. This will facilitate the identification of drug candidates able to recognize the binding region of the pathogenic GCAP1 mutants with the cyclase and to competitively inhibit the constitutive retGC1 activation, restoring the homeostasis of second messengers which is impaired in retinal degenerative diseases. A preliminary molecular docking based on the crystal structure of the chicken protein was performed and I identified four molecules able to bind the *wt* human GCAP1 in the millimolar/micromolar range.

Together these results shed new light on the quaternary assembly of the *wt* human GCAP1, showing how the structural changes related to the presence of  $\text{Ca}^{2+}$  or  $\text{Mg}^{2+}$  are reflected in the different measured dimerization constant. Such conformational changes are in turn likely related to the regulatory mechanism of GCAP1 in the modulation of the retGC1 activity.

The differences between the oligomerization state of D100G, E155G and E155A variants suggest a correlation between the altered quaternary assembly of GCAP1 and the aberrant activity of the mutants, representing a step forward to dissect the structural bases of the altered regulatory mechanism of GCAP1 in retinal dystrophies.

# Riassunto

I sensori neuronali del calcio svolgono un ruolo cruciale in diversi processi di neurotrasmissione regolati dal calcio. Tra essi la proteina *guanylate cyclase-activating protein 1* (GCAP1) è espressa nei fotorecettori e durante la fototrasduzione, a seconda della concentrazione del calcio in cellula, agisce da attivatore o inibitore della guanilato ciclasi retinica (retGC1). Ad oggi 22 mutazioni patologiche che causano distrofia della retina sono state associate a GCAP1, ma ancora manca un completo quadro dei determinanti molecolari alla base della patologia. L'unica struttura cristallografica di GCAP1 disponibile è l'omologa di pollo, nella quale la proteina è legata al calcio, ovvero si trova nello stato inibitorio della retGC1.

Ancora nessuna cura esiste per la distrofia della retina.

In questo studio mostro per la prima volta che la GCAP1 umana è caratterizzata da un equilibrio monomero-dimero molto dinamico, la cui costante di dissociazione è influenzata dalla concentrazione di sale e dalla natura dello ione bivalente legato dalla proteina.

Ho inoltre scoperto che anche la proteina omologa di pollo presenta un meccanismo simile, il quale suggerisce che l'equilibrio monomero-dimero potrebbe essere funzionale all'attività di GCAP1 essendo conservata tra specie diverse. Nonostante il grande numero di prove di cristallizzazione eseguite, non è stato ottenuto nessun cristallo della GCAP1 umana che abbia prodotto un segnale di diffrazione ai raggi X, probabilmente anche a causa della flessibilità della regione C-terminale e dell'intrinseca dinamicità della proteina. Per superare questo problema ho prodotto un costrutto in cui mancano i 12 residui C-terminali e con 2 mutazioni utili ad introdurre un ponte disolfuro tra i domini N- e C-terminale, il quale è stato cristallizzato con successo. Abbiamo provato che tale costrutto ingegnerizzato è in grado di regolare la retGC1 allo stesso modo della proteina nativa.

Combinando SAXS, docking molecolare proteina-proteina e simulazioni di dinamica molecolare, proponiamo due nuovi modelli del dimero di GCAP1 umana legata al calcio, i quali sono stabilizzati dagli stessi residui coinvolti nella comunicazione con la retGC1.

Abbiamo utilizzato un approccio biofisico e biochimico per studiare in modo approfondito tre mutanti patologici (D100G, E155A ed E155G) caratterizzati da mutazioni che colpiscono residui direttamente coinvolti nella coordinazione del calcio. Tutte e tre le varianti sono in grado di formare oligomeri in soluzione, mostrando una minore affinità per il calcio e attivando costitutivamente la retGC1 a concentrazioni di calcio fisiologiche. Oltre ad effetti strutturali

locali, queste mutazioni perturbano anche la struttura quaternaria di GCAP1, lasciando intendere che la formazione di complessi multimerici della proteina potrebbe influire sulla sua attività biologica.

Ho inoltre prodotto un baculovirus ricombinante per esprimere il dominio citoplasmatico della retGC1 in cellule di insetto con lo scopo di ottenere informazioni strutturali a livello atomico sul complesso tra GCAP1 e retGC1. Ciò contribuirà ad identificare piccole molecole in grado di riconoscere e legare l'interfaccia di interazione dei mutanti patogenici di GCAP1 con la ciclasi e di inibire competitivamente l'attivazione costitutiva di retGC1, ripristinando l'omeostasi dei secondi messaggeri, la cui alterazione è alla base dei disturbi degenerativi della retina.

È stato eseguito un docking molecolare preliminare sulla struttura cristallografica della GCAP1 di pollo e sono state identificate quattro molecole in grado di legare la proteina umana nativa nel range millimolare/micromolare.

L'insieme di questi risultati getta una nuova luce sull'organizzazione della struttura quaternaria della GCAP1 *wt* umana, dimostrando come i riarrangiamenti strutturali che dipendono dalla presenza di  $\text{Ca}^{2+}$  o  $\text{Mg}^{2+}$  si riflettono nelle differenti costanti di dimerizzazione misurate. Questi cambiamenti conformazionali sono verosimilmente legati al meccanismo regolatorio di GCAP1 nella modulazione dell'attività della retGC1. Il differente stato oligomerico osservato per le varianti D100G, E155G ed E155A suggerisce una correlazione tra l'alterazione della struttura quaternaria di GCAP1 e l'attività aberrante dei mutanti, rappresentando un passo in avanti nel comprendere più dettagliatamente le basi strutturali dell'alterato meccanismo regolatorio di GCAP1 nelle distrofie alla retina.

# 1. Introduction

## 1.1 Neuronal calcium-sensor proteins

Many biological processes from millisecond regulation of ion channels to long term gene expression are regulated by intracellular free calcium concentration ( $[Ca^{2+}]$ ) [1]. Different effects of changes in  $[Ca^{2+}]$  are related to the different magnitude, duration and localization of the  $Ca^{2+}$  signal [2]. In neurons, in particular, intracellular calcium variations are detected and mediated by specialized  $Ca^{2+}$ -binding proteins called Neuronal Calcium Sensors (NCS). NCS have been identified in many organisms ranging from yeast to human. In the human genome there are 14 genes encoding NCS (table 1.1), each one involved in different pathways of calcium-mediated neurotransmission.

NCS protein	Function
NCS-1	regulation of neurotransmission
Neurocalcin $\delta$	endocytosis
Hippocalcin	anti-apoptotic, MAP kinase signalling
VILIP-1	guanylyl cyclase and adenylyl cyclase modulation, traffic of nicotinic receptors
VILIP-2	binding to presynaptic P/Q-type calcium channel
VILIP-3	MAPK signaling modulation
Recoverin	inhibition of rhodopsin kinase in photoreceptors
GCAP-1	regulation of guanylyl cyclase in photoreceptors
GCAP-2	regulation of guanylyl cyclase in photoreceptors
GCAP-3	regulation of guanylyl cyclase in photoreceptors
KChIP1	potassium channels, repression of transcription
KChIP2	potassium channels, repression of transcription
KChIP3	potassium channels, presenilin-binding
KChIP4	potassium channels, repression of transcription

Table 1.1: NCS proteins identified in mammalian genome. Adaptation from ref. [1].

All the NCS share a high sequence homology (fig.1.1) and a common tertiary structure composed of four EF-hand motifs, three of them (two in the case of recoverin and KChIP1)

able to bind divalent ions. Eleven of the mammalian NCS are myristoylated at the N-terminal: the corresponding EF-hand domain does not have the capability to bind  $\text{Ca}^{2+}$ . The structure of several NCS have been solved by X-ray crystallography or NMR, including the  $\text{Ca}^{2+}$ -bound forms of yeast and human NCS-1 [3] [4], GCAP2 [5], neurocalcin  $\delta$  [6], KChIP1 [7] and recoverin [8].

The NCS are characterized by a conformational change that occurs upon calcium binding. For many of them (*i.e.* recoverin, hippocalcin, neurocalcin  $\delta$ , VILIP1 and VILIP3) a  $\text{Ca}^{2+}$ /myristoyl switch has been described.

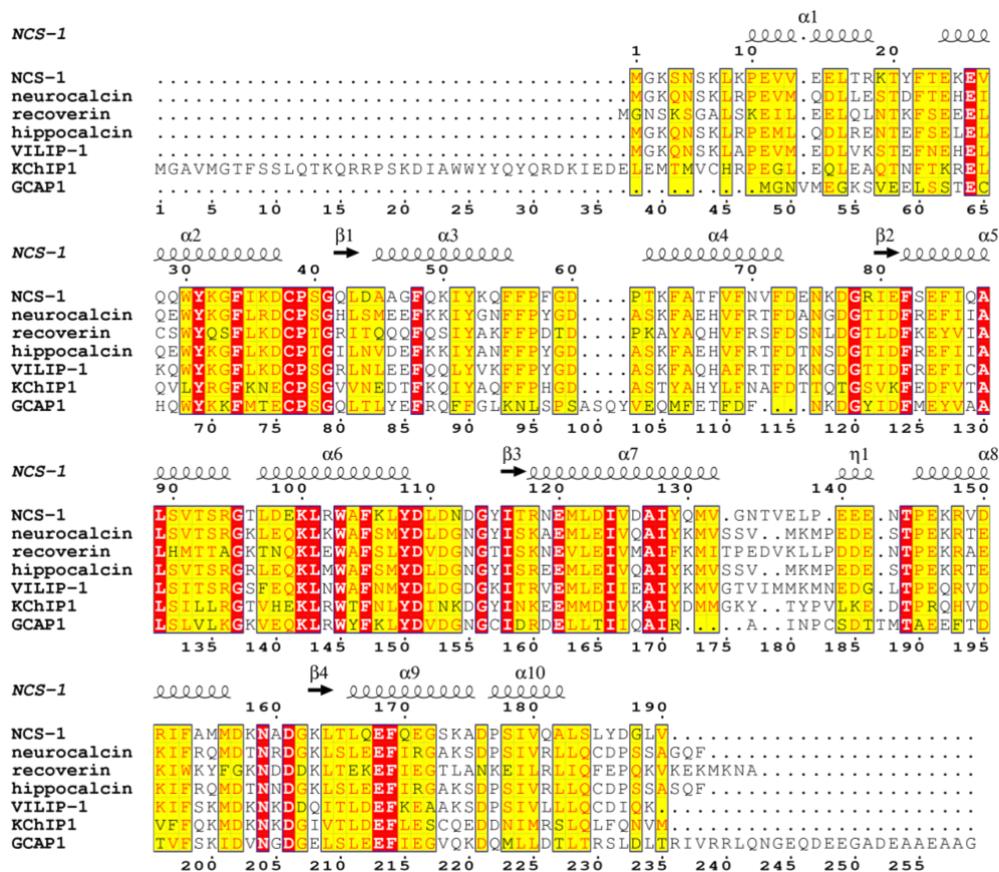


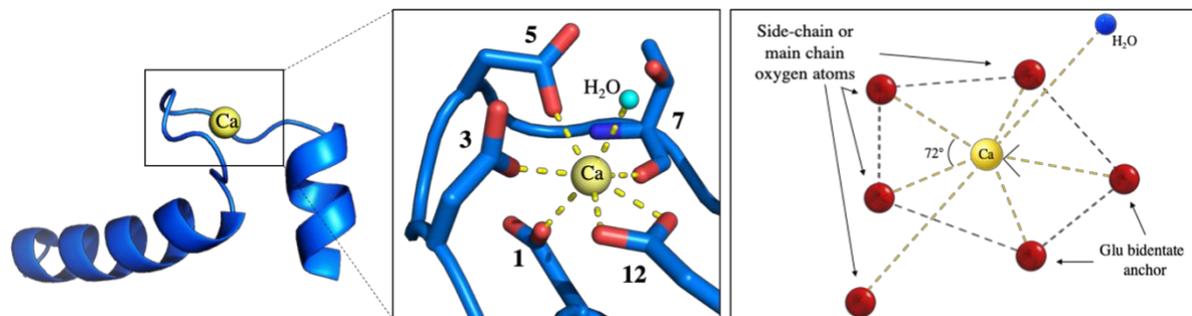
Figure 1.1 NCS sequence alignment from reference [9].

Recoverin, for example, extrudes the myristic moiety from its hydrophobic cleft upon  $\text{Ca}^{2+}$  binding [8], allowing its translocation from the cytosol to the disc membrane of rod cells [10] in order to modulate the activity of the retinal rhodopsin kinase.

Nevertheless, the  $\text{Ca}^{2+}$ /myristoyl switch is not extended to all the NCS. Indeed GCAP1, although characterized by conformational changes upon binding to calcium or magnesium, does not extrude the myristic acid which is sequestered in the hydrophobic core of the protein [11] both in the  $\text{Ca}^{2+}$ -bound (inhibitory state) [12] and  $\text{Ca}^{2+}$ -free (activator state) [13].

## 1.2 The EF-hand motif

The EF-hand motif is a super secondary structure characterized by a helix-loop-helix topology (fig.1.2) shared by most of the NCS [14]. The EF-hand motifs are able to coordinate divalent ions such as  $Zn^{2+}$ ,  $Cu^{2+}$ ,  $Fe^{2+}$  and  $Mg^{2+}$ , but they display a higher affinity for  $Ca^{2+}$  [15].



EF-loop position	1	2	3	4	5	6	7	8	9	10	11	12
most common	Asp (100%)	Lys (29%)	Asp (76%)	Gly (56%)	Asp (52%)	Gly (96%)	Thr (23%)	Ile (68%)	Asp (32%)	Phe (23%)	Glu (29%)	Glu (92%)
also observed		Ala Gln Thr Val Ile Ser Glu Arg	Asn	Lys Arg Asn	Ser Asn		Phe Lys Gln Tyr Glu Arg	Val Leu	Ser Thr Glu Asn Gly Gln	Tyr Ala Thr Leu Glu Lys	Asp Lys Ala Pro Asn	Asp

**Figure 1.2** The coordination of a calcium ion within the EF-hand motif (isolated EF-hand from calmodulin, pdb-id:1CLL) Readaptation from [16]. The table below reports the most common amino acids observed at each position with the corresponding percentage of occurrence.

The amino acids responsible for the coordination of the cations are located in the loop between the two alpha helices. The spatial orientation of the side-chains allows to form a coordination network characterized by a pentagonal bi-pyramidal geometry of negative charges provided by the residues in position 1, 3, 5, 9, a water molecule, the backbone C=O of residue 7 and the residue 12 which provides a bidentate coordination with the ion [15].

The affinity for calcium is not the same among different  $Ca^{2+}$ -sensors because of the different aminoacidic sequence of the EF-loops. Indeed, bigger side chains in position 9 and 12, such as Glu or Gln, determine a higher  $Ca^{2+}$  affinity of the EF-hand motif with respect to the smaller residues Asp or Asn, that require an additional water molecule to complete the coordination network [17]. In general, the EF-hand motifs exhibit an affinity reduced by 4-5 orders of magnitude for  $Mg^{2+}$  respect to that for  $Ca^{2+}$ . This is likely due to the greater ionic diameter and the more complex network required for  $Mg^{2+}$  coordination, that includes six ligands arranged

in a octahedron [15]. Indeed, upon hydration the increase of the radius of  $Mg^{2+}$  is 16-fold higher respect to the increase shown by  $Ca^{2+}$ , involving a higher energy of binding and causing the residue in position 12 to provide a monodentate coordination [18].

### 1.3 Phototransduction

The phototransduction cascade is a cluster of biophysical and biochemical reactions that convert an external light stimulus into an electrical signal in the retina, which eventually allows the elaboration of the vision in the brain visual cortex.

The starting point of this complex process is the outer nuclear layer of the retina which accommodates specialized photoreceptors: cones and rods (fig. 1.3).

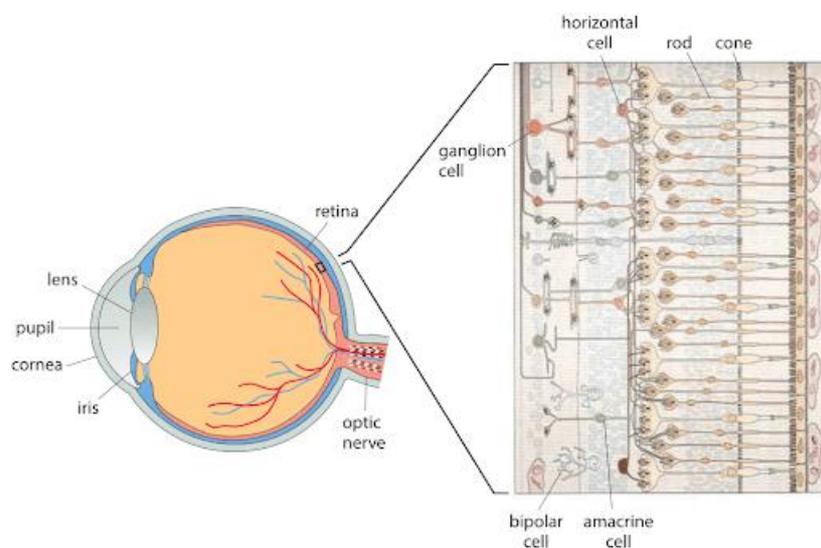


**Figure 1.3** Schematic representation of retinal layers with rods and cones on the right [19].

Two second messengers, cGMP and  $Ca^{2+}$ , are responsible for the fine modulation of the phototransduction cascade, both involved in the activation, amplification and deactivation of the light signal. For this reason, photoreceptors take advantage of several different NCS in order to process the light stimulus, each one with its specific physiological function [20].

The first step in phototransduction is the absorption of a photon by the G-protein coupled receptor rhodopsin (fig. 1.4). The activated rhodopsin causes its associated G-protein transducin to exchange GDP with GTP, hence releasing the activated  $\alpha$ -subunit which promotes the hydrolysis of cGMP to 5'-GMP by phosphodiesterase. Because of the drop in cGMP concentration, cyclic nucleotide gated (CNG) channels close and prevent  $Ca^{2+}$  and  $Na^{+}$  ions from entering the cytoplasm. At the same time the  $Na^{+}/Ca^{2+}$ ,  $K^{+}$  exchangers (NCKX)

continue to extrude  $\text{Ca}^{2+}$  from cytoplasm, causing a drop in intracellular  $\text{Ca}^{2+}$  concentration from 600-500 nM to 100 nM [21]. This condition triggers the hyperpolarization of cones and rods which leads to a decreased release of glutamate at the synapse, allowing photoreceptors to transmit the signal to second-order cells of the retina and ultimately to the ganglion cells.

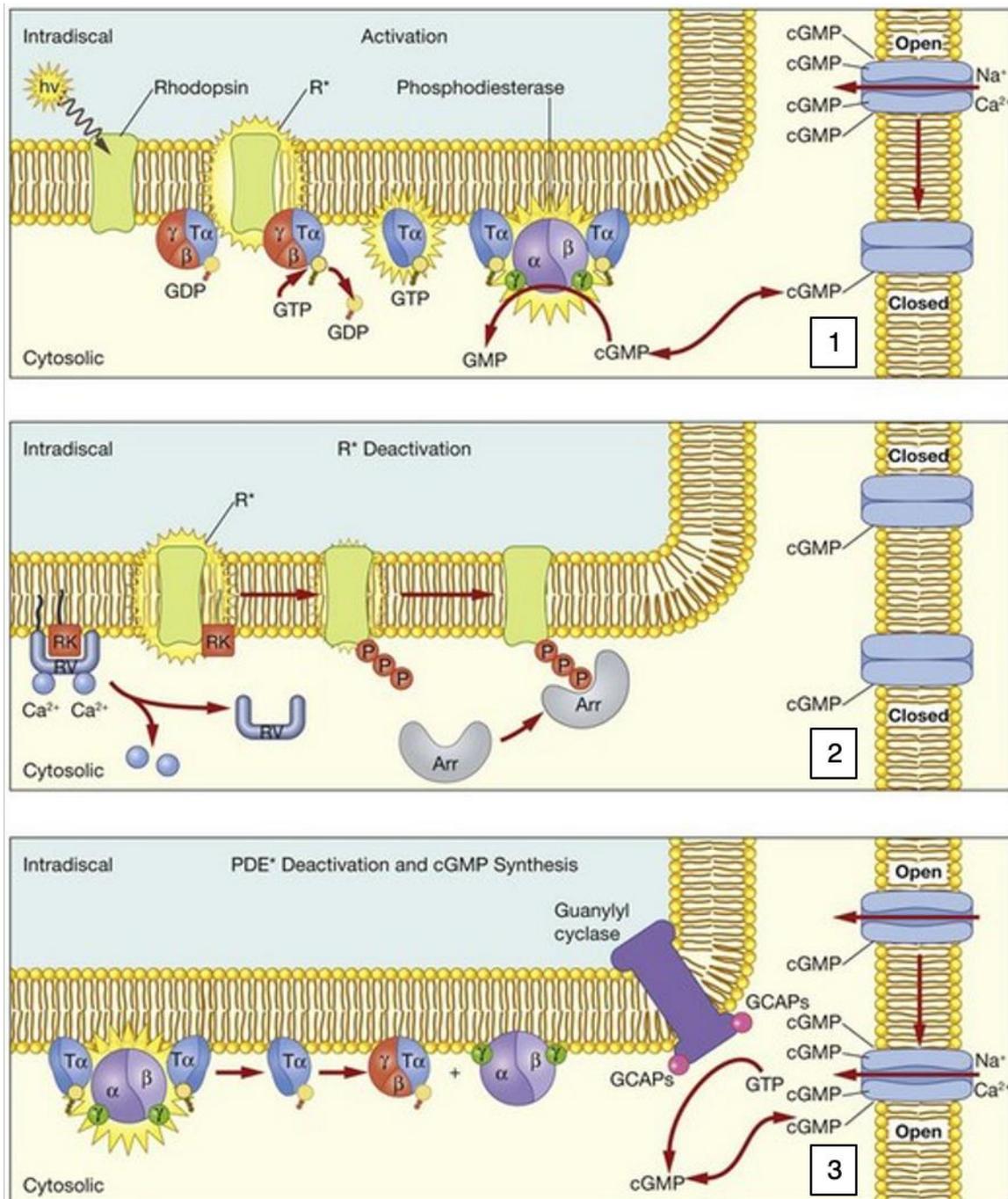


**Figure 1.4** The main steps of the phototransduction cascade from [22]. 1 - signal activation by rhodopsin; 2 - Rhodopsin negative regulation by Recoverin; 3 - Guanylate cyclase modulation by GCAPs.

NCS play a crucial role in the modulation of the light signal since they are sensitive to the changes in intracellular calcium concentration. In particular, at low  $[Ca^{2+}]$  recoverin activates protein Rho kinase, which allows the binding of the phosphorylated Rho to arrestin [23]. At the same time GCAPs activate the guanylate cyclase protein which is responsible to replenish the cytoplasmic cGMP level and the dark-currents through the re-opening of the CNG channels [24].

## 1.4 Guanylate cyclase activating protein 1 (GCAP1)

In photoreceptor cells the activity of retinal guanylate cyclase (retGC) is modulated by a family of NCS called guanylate cyclase activating proteins (GCAPs). In the human genome there are three genes coding for different isoforms of GCAPs: *GUCA1A* and *GUCA1B* located on 6p21.1 coding respectively for GCAP1 and GCAP2 proteins which are expressed both in cones and rods [25]; *GUCA1C* is located on a different chromosome (3q13.1) and codes for GCAP3 which is expressed exclusively in cones. GCAP3, unlike GCAP1 and GCAP2, seems not to be involved in the phototransduction cascade [26].

GCAP1 is a 23 kDa protein mainly composed of the repetition of four EF-hand motifs arranged in two semiglobular domains. The EF-hand motifs of GCAP1 can bind both magnesium and calcium ions: in particular EF2, 3 and 4 are able to bind up to three  $Ca^{2+}$  ions (fig. 1.5) with a sub-micromolar affinity, while EF2 and putatively EF3 can bind up to two  $Mg^{2+}$  ions with a sub-millimolar affinity [24]. GCAP1 acts both as the activator or inhibitor of retGC1 and the ability of EF2 and EF3 to perform the  $Ca^{2+}/Mg^{2+}$  exchange is an essential component for the inhibition/activation mechanism through a  $Ca^{2+}$  - mediated negative feedback regulation [11].

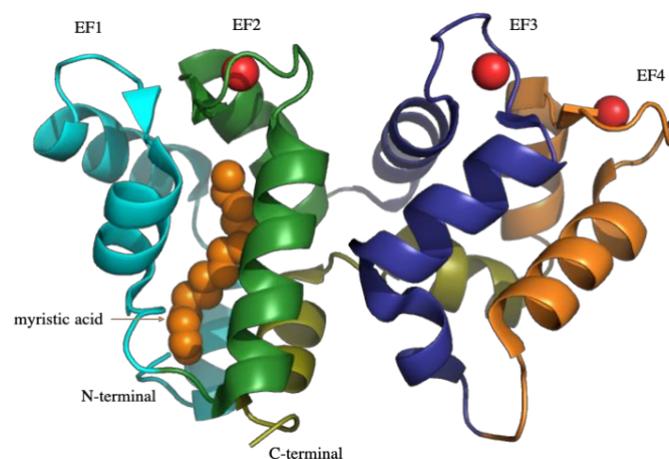


**Figure 1.5** Crystal structure of  $Ca^{2+}$ -bound chicken GCAP1 (pdb-id: 2R2I). Myristoylated (orange spheres) N-ter domain composed of EF1 (cyan) and EF2 (green); C-ter domain with EF3 (purple) and EF4 (orange). Calcium ions are shown as red spheres.

Unlike the other EF-hand motifs, EF1 is characterized by an amino acidic sequence (a Cys followed by Pro) that impairs its ability to coordinate  $\text{Ca}^{2+}$  in all NCS [27]. The  $\alpha$ -helices of EF1 and EF2 define a hydrophobic cleft which hosts a molecule of myristic acid covalently bound to the N-terminal glycine. Although a  $\text{Ca}^{2+}$ /myristoyl switch mechanism has never been observed for GCAP1, the myristic acid in combination with EF1 play a pivotal role in the interaction with the target protein retGC1 [11] and in the modulation of the affinity for the cations [28].

retGC1 and retGC2 are two isoforms of guanylate cyclase expressed in retinal cells. Both the GCs are involved in the phototransduction pathway [29] and are composed of an extracellular domain, a trans-membrane  $\alpha$ -helix, a juxta-membrane domain (JMD) followed by a dimerization domain (DD) and a catalytic domain (CD) which is active only upon GC dimerization. In the dark-adapted photoreceptors at high  $[\text{Ca}^{2+}]_i$  (600-500 nM) GCAP1 binds three  $\text{Ca}^{2+}$  ions and adopts an inhibitory conformation which keeps the retGC1 activity at basal level (fig. 1.6). When the phototransduction cascade starts after the absorption of a photon,  $[\text{Ca}^{2+}]_i$  drops to 100 nM, GCAP1 exchanges  $\text{Ca}^{2+}$  (firstly from EF3, then EF2 and finally from EF4) with  $\text{Mg}^{2+}$  and becomes an activator of retGC1 [11][30].

During phototransduction, the activity of GCAP1 is complemented by GCAP2 [24][30], which activates the GCs in the case of a prolonged light stimulus that further decreases  $[\text{Ca}^{2+}]_i$ .

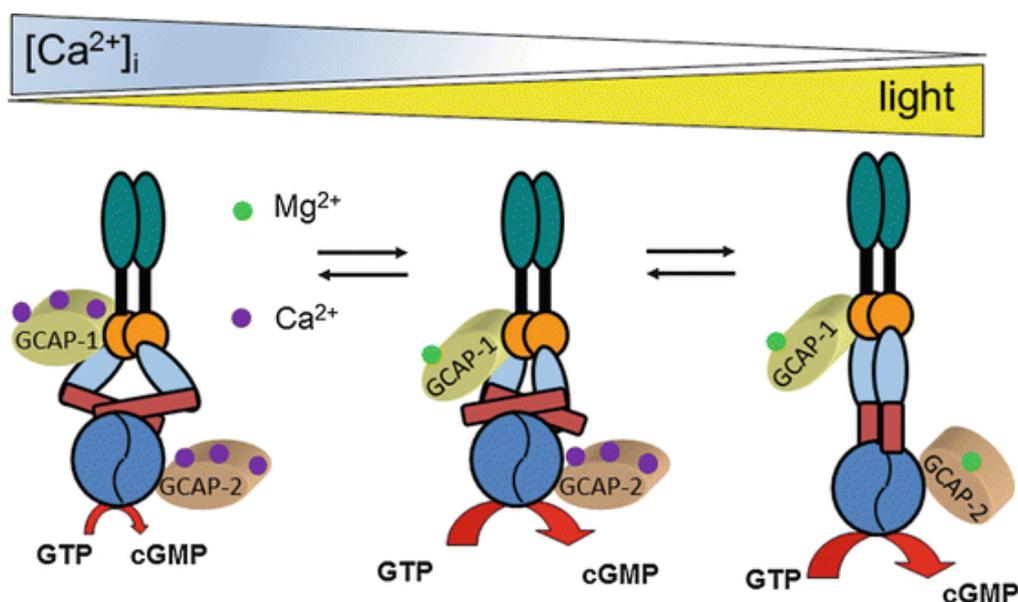


**Figure 1.6**  $\text{Ca}^{2+}$ -relay model: retGC modulation by GCAP1 and GCAP2 during phototransduction from [30].

## 1.5 GCAPs quaternary assembly

In 1999 it was first described that human GCAP2 forms stable dimers in solution, in particular the  $\text{Ca}^{2+}$ -loaded monomer undergoes reversible dimerization upon dissociation of  $\text{Ca}^{2+}$ . The dimerization of GCAP2 correlates with its ability to modulate the retGC1 activity in vitro: the GCAP2 E80Q/E116Q/D158N mutant forms indeed a stable dimer even at low  $\text{Ca}^{2+}$  concentrations which constitutively activates the retGC1. Interestingly, mutations aimed at restoring the inhibitory activity of the GCAP2 variant also restore its ability to form dimers [31]. Recently, it was reported that GCAP2 is able to dimerize both in the  $\text{Ca}^{2+}$ -free and  $\text{Ca}^{2+}$ -bound states [5]. The GCAP2 homodimer model obtained by chemical cross-linking and high-resolution mass spectrometry is stabilized by polar interactions of charged residues K98, L167, V171, R175, K183, Q186 and D188 [32].

Similarly to GCAP2, GCAP1 is able to form dimers in solution but its dimerization was originally reported to be  $\text{Ca}^{2+}$ -independent [31]. The bovine homologue was investigated with double elector-electron resonance (DEER) experiments in order to produce a structural model of the dimeric GCAP1 assembly. The residues involved in the dimerization interface of GCAP2 are unrelated to those identified in the interface of GCAP1 dimer. In particular, the bovine homologue was described as symmetric or non-symmetric dimer stabilized by hydrophobic intermolecular contacts involving residues H19, Y22, V77 and W94. Moreover, side directed mutagenesis of these residues hamper the dimerization of the protein and completely abolish its ability to regulate the retGC1, which in turn needs to dimerize in order to be active. The structural differences between GCAP2 and GCAP1 dimeric assemblies could explain their functional different mechanism in the allosteric regulation of retGC1 in photoreceptors [33].

## 1.6 GCAP1 pathological mutants: the cone dysfunction syndromes

The cone dysfunction syndromes are a group of heterogeneous disorders characterized by autosomal dominant (AD) transmission affecting the retina, causing reduced central and/or peripheral vision, abnormalities in colour perception, nystagmus, hemeralopia, photophobia and ultimately leading to blindness [34]. Depending on the type of photoreceptors involved and on the area of the retina affected, retinal dystrophies can be classified as Cone dystrophy (COD), Cone-Rod dystrophy (CORD) and Macular dystrophy (MD).

COD and CORD are two inherited diseases that can start in early infancy, whose progression eventually led to photoreceptors degeneration [35].

From 1998 to date, thanks to Next Generation Sequencing development, 22 mutations of the *GUCAlA* gene have been described in patients affected by retinal dystrophies: P50L, L84F, G86R, E89K, Y99C/S/N, D100G/E, E102H, E111V, N104K, I107T, T114I, I143N/T, D148E, L151F, E155A/G, G159V, L176F (table 1.3).

Although an accurate molecular mechanism has not been described and extended to all the GCAP1 variants responsible for COD/CORD, most of the pathological mutants display an altered  $\text{Ca}^{2+}$  affinity, resulting in an impaired inhibition of retGC catalytic activity [36]. This condition provokes the accumulation of cGMP determining an increase of intracellular  $\text{Ca}^{2+}$  influx mediated by CNG channels. The excess of cGMP could indeed trigger cytotoxic effects [37]; at the same time an uncontrolled increase of  $\text{Ca}^{2+}$  concentration in the inner segment of photoreceptors may perturb the membrane potential of mitochondria. Consequently, the Cytochrome C would be released activating the caspase-dependent apoptosis pathway [38].

Even though the decreased affinity for  $\text{Ca}^{2+}$  is a common feature shared by the pathological GCAP1 mutants, the L84F and L176F variants show a *wt*-like  $\text{Ca}^{2+}$  affinity and peculiar changes in protein conformation [39] [40] suggesting that the impaired  $\text{Ca}^{2+}$  sensitivity could not be the only cause for COD and CORD. Moreover, the  $\text{Ca}^{2+}/\text{Mg}^{2+}$  roles in regulating protein activity suggest that GCAP1 function is exerted by a complex mechanism controlling the interaction with the retGC. The mutations of GCAP1 residues participating in the binding to retGC indeed cause the abolition of the cyclase activity but surprisingly preserves the ability of mutated GCAP1 to bind the retGC showing competition with the *wt* protein [41].

Although mutations affecting the amino acids involved in  $\text{Ca}^{2+}$  coordination can be expected to cause conformational structural changes, biochemical and biophysical analyses assessed a native-like fold for several mutants [42].

Together these data indicate a complex pathological phenotype at the base of retinal dystrophies that still requires further investigations. In general, the molecular mechanisms leading to COD/CORD seem not to be shared by all the pathological GCAP1 variants, leaving many issues to be solved in order to achieve a complete understanding of the molecular basis of retinal dystrophies. Currently no cure for COD and CORD is available.

nucleotide change	GCAP1 variant	region	phenotype
C.149C>T	<b>P50L</b>	EF1-EF2 link	COD, CORD
C.250C>T	<b>L84F</b>	EF2 helix F	COD, CORD
C.256G>C	<b>G86R</b>	EF2-EF3 link	CORD
C.265G>A	<b>E89K</b>	EF2-EF3 link	COD, MD; COD CORD
C.295T>A	<b>Y99N</b>	EF3 helix E	COD, CORD
C.296A>G	<b>Y99C</b>	EF3 helix E	COD, CORD
C.296A>C	<b>Y99S</b>	EF3 helix E	COD, CORD
C.299A>G	<b>D100G</b>	calcium binding EF3 loop	CORD, MD
C.300T>A	<b>D100E</b>	calcium binding EF3 loop	COD
C.304G>C	<b>D102H</b>	calcium binding EF3 loop	CORD
C.312C>A	<b>N104K</b>	calcium binding EF3 loop	COD; COD, CORD; MD
C.320T>C	<b>I107T</b>	EF3 loop	MD
C.322A>T	<b>E111V</b>	EF3 helix F	CORD
C.341C>T	<b>T114I</b>	EF3 helix F	atypical RP
C.428delTinsACAC	<b>I143T/N</b>	EF3 helix E	COD
C.444T>A	<b>D148E</b>	EF4 loop	COD
C.451C>T	<b>L151F</b>	EF4 loop	COD
C.464A>G	<b>E155G</b>	calcium binding EF4 loop	COD
C.464A>C	<b>E155A</b>	calcium binding EF4 loop	CORD
C.476G>T	<b>G159V</b>	EF4 helix F	COD, CORD
C.526C>T	<b>L176F</b>	C-terminal	MD

**Table 1.3** pathological GCAP1 variants associated with retinal dystrophies. Adaptation from [43], updated with [44], [45], [46].

## 2. Aim of the project

The present PhD project was focused on the study of the recombinant human GCAP1 and of some pathological variants responsible for COD/CORD. The described work was done in the context of the project “*Cone dystrophies and retinal degeneration from protein structures to biological networks. Toward the design of therapeutic molecules.*” funded by the Italian Telethon foundation (GGP16010 grant) and carried out at the *Biophysics Institute (IBF)* of the *National Research Council (CNR – Milan)*.

COD and CORD are severe inherited retinal dystrophies affecting photoreceptors, whose dysfunction can lead to decreased central vision, reduced colour vision, photophobia and blindness. The biological activity of GCAP1 is exerted with a mechanism composed of at least three components:  $\text{Ca}^{2+}$ -binding, retGC1-binding and modulation of retGC1 activity. Although pathogenic GCAP1 mutations often exhibit an impaired  $\text{Ca}^{2+}$ - sensitivity and constitutively activate retGC1, this aberrant mechanism is still under investigation. For instance, L176F mutant is known to increase the binding affinity for retGC1 but it simultaneously reduces the sensitivity of cyclase regulation [28]. Moreover, the point mutation of some residues (like M26, K85 and W94) of the putative cyclase binding region does not prevent GCAP1 co-localization with retGC1 [41].

Most of the pathogenic GCAP1 mutants show a native-like fold, while some of them still lack a thorough biophysical characterization and in some instances their biochemical and structural analysis did not reveal a clear correlation with the pathological consequences, thus preventing a unified description of the molecular features responsible for photoreceptor degeneration.

To date the only crystallographic structure of wild type GCAP1 available is the  $\text{Ca}^{2+}$ -bound myristoylated homologue from chicken that represents the retGC1-inhibiting form; high resolution data on the retGC1-activating form and/or COD/CORD-associated mutants are still missing. A dimeric assembly of the homologue bovine GCAP1 was recently reported, but the quaternary structure of the human protein, although observed in the past, has never been investigated. Such lack of information prevents the analysis of features, such as the allosteric mechanisms regulated by  $\text{Ca}^{2+}/\text{Mg}^{2+}$ -binding as well as the GCAP1/retGC1 interaction or the possible biological role of GCAP1 dimerization, that might be crucial in determining the molecular basis of the disease and planning an effective strategy to find a cure.

Therefore, the aim of the present PhD project was to investigate the molecular determinants of the wild type human GCAP1 and shed light on its quaternary organization and its potential role

in the regulation of retGC1 (data reported and published in **paper 1**). At the same time, three pathological mutants D100G, E155A and E155G were produced in order to analyse the structural and functional effects of missense mutations affecting EF3 and EF4 loops (data reported and published in **paper 2**). The final purpose of this project was to identify suitable molecules able to interfere with the abnormal regulation of the retGC1.

During the three years of this PhD project, I set up robust production and purification protocols to obtain the recombinant myristoylated wild type human GCAP1 and its pathological variants in a soluble form. Exhaustive biochemical analyses were carried out *in vitro* to characterize the quaternary assembly of GCAP1 and analyse the monomer-dimer equilibrium with a combined approach based on analytic size exclusion chromatography (SEC) and MicroScale Thermophoresis (MST). Unfortunately, despite the huge number of crystallization trials using also different constructs of GCAP1 in both the apo and olo forms, no diffracting crystals were obtained. To overcome this problem several experiments of Small Angle X-ray Scattering (SAXS) coupled with SEC were carried out at *European Radiation Synchrotron Facility* (Grenoble) and *Diamond Light Source* (Oxford) allowing to produce low resolution models of the human dimer.

MST was used on the *wt* human GCAP1 in order to measure the binding affinity of 10 compounds identified with *in silico* docking, identifying four molecules with  $K_d$  in the high micromolar range to be tested hereafter in retGC1 activity essays to assess their possible influence on GCAP1 biological role.

Finally, I exploited *Sf9* insect cells in order to obtain a baculovirus containing the cytoplasmic domain of retGC1 with the aim to produce a soluble construct suitable to collect structural information of the retGC1/GCAP1 complex.

## 3. Results and discussion

### 3.1 hGCAP1 expression and purification in a soluble form

The sequence coding for the human *wt* GCAP1 was cloned into a pET11a plasmid in order to express the recombinant protein in *E. coli* cells. The pathological variants D100G and E155G were obtained by site-directed mutagenesis. All the three constructs were kindly provided by Prof. Daniele Dell'Orco (University of Verona) and carry the E6S mutation in order to have a consensus sequence for the post-translational myristoylation. The E155A mutation was obtained by site-directed mutagenesis using the *wt* template at our institute.

In order to produce a myristoylated recombinant GCAP1, a pBB131 plasmid carrying a yeast N-myristoyl transferase 1 (NMT-1) is commonly used to co-transform *E. coli* BL21 cells for each construct. So far, this system resulted in the overexpression of an insoluble myristoylated GCAP1, forcing its refolding from the inclusion bodies.

From the very first preliminary expression trials conducted in our laboratory, we found that using the *E. coli* BL21 *CodonPlus RP* strain is possible to overexpress a recombinant myristoylated GCAP1 in a soluble form which allowed its purification from the soluble clarified cell extract (CE). Since the purification protocol used to isolate the full-length human *wt* GCAP1 (hGCAP1) was the same used for the production of the D100G, E155G and E155A variants, the following results are to be considered extended to all the constructs mentioned.

#### 3.1.1 Ion exchange chromatography

Due to the N-terminal myristoylation which characterize GCAP1 and since the plasmids provided did not contain any C-terminal fusion tag, the low theoretical isoelectric point (4.4) of GCAP1 was exploited to separate the protein from all the other *E. coli* contaminants with an ion exchange chromatography (IEC) as the first purification step.

The CE resulting from cell lysis and centrifugation was loaded on a HiPrep™*TMQ* XL 16/10 column as reported in 5.3.2. A linear NaCl gradient from 0.2 M to 1 M was used to elute GCAP1 from the resin with a 2 ml/min flow rate.

As reported in the corresponding chromatogram (fig. 3.1), most of the contaminants eluted in the flow through (FT). At 20% of the elution buffer the first peak (A) consisted of other

contaminants less charged with respect to hGCAP1. The recombinant protein eluted in the two peaks at 50% of elution buffer: the first one (B1) contains a small amount of the recombinant protein with still many other contaminants, while the second one (B2) consists mainly of GCAP1. A third peak (C) containing small fragments not detectable in SDS-PAGE eluted at 100% buffer B. All the fractions collected were analysed by SDS-PAGE in order to identify those containing hGCAP1 to collect and use for the second chromatographic passage.

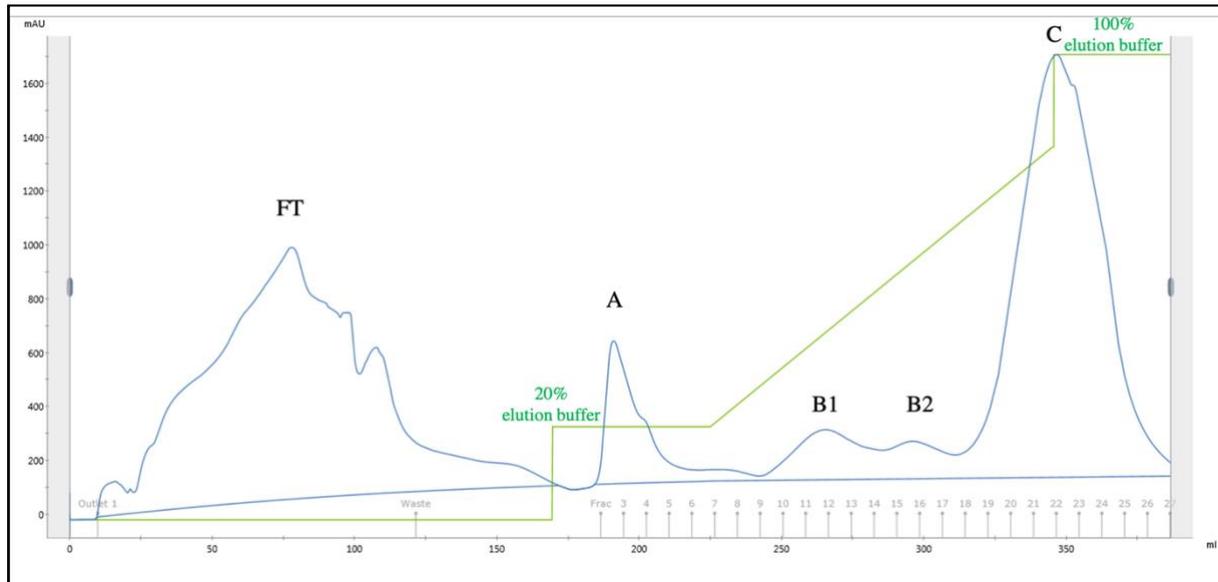


**Figure 3.1:** hGCAP1 *wt* IEC. Elution volume (ml) is reported on the x axis, absorbance at 280 nm (mAU) is reported on the y axis. The green line represents the elution buffer gradient from 20% to 100%.

### 3.1.2 Size exclusion chromatography

Fractions from IEC corresponding to hGCAP1 (peak B2) were pooled and concentrated to 3 ml volume. A size exclusion chromatography (SEC) was performed as reported in 5.3.3 in order to separate the protein of interest from other contaminants based on the hydrodynamic radius with. The chromatogram in figure 3.2 reports the elution profile corresponding to the hGCAP1 *wt* (similar to what obtained with the studied pathological variants). As confirmed by SDS-PAGE, the main peak contains GCAP1 with a high level of purity as reported in fig. 3.3. In denaturant conditions GCAP1 is detected as a single band with an associated molecular weight (MW) close to the green line of the protein ladder (22 kDa) which is compatible with the GCAP1 monomer (23 kDa).

The fractions corresponding to the purified protein were pooled and concentrated for the successive biochemical and biophysical characterization.

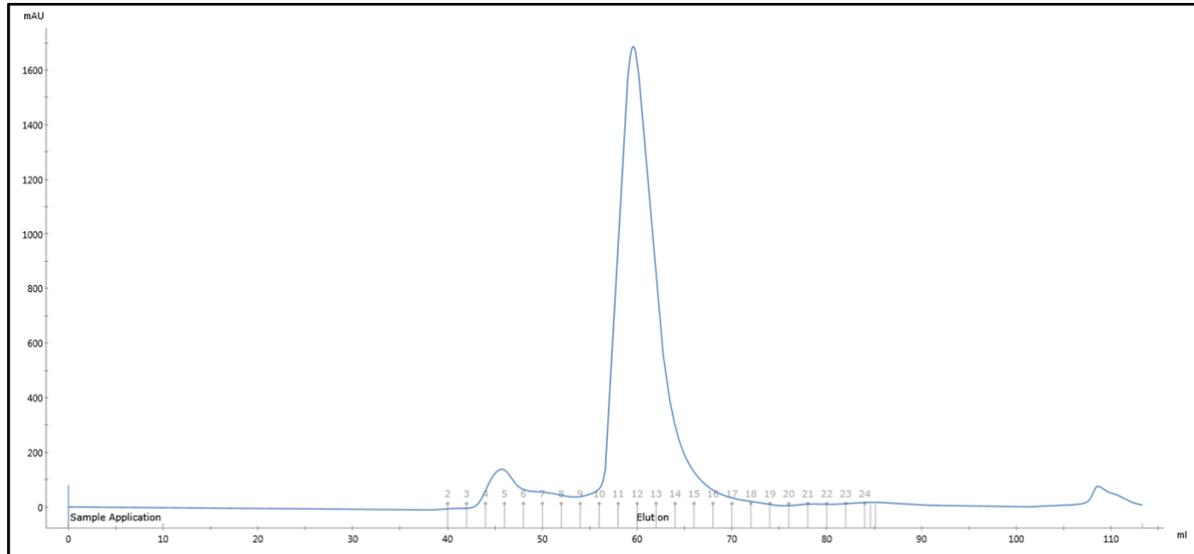


**Figure 3.2:** hGCAP1 $_{wt}$  SEC. Elution volume (ml) is reported on the x axis, absorbance at 280 nm (mAU) is reported on the y axis. The main peak corresponds to the isolated hGCAP1.

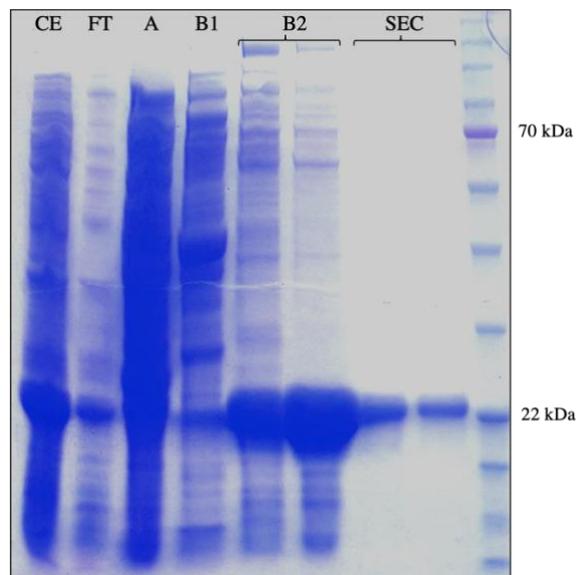


**Figure 3.3:** SDS-PAGE corresponding to the purification steps of hGCAP1  $_{wt}$ . Fractions are reported on the top (CE: clarified extract; FT: flow-through; A, B1 and B2 correspond to the elution peaks reported in the IEC chromatogram; SEC: fractions corresponding to the main elution peak reported in the SEC chromatogram; last lane: reference protein ladder).

### **3.2 Circular dichroism analysis: assessing the protein secondary structure**

Circular dichroism (CD) spectra were collected on the hGCAP1 *wt* in the far (200-250 nm) UV to check the correct folding of the purified recombinant protein in terms of secondary structure and monitor structural changes between the apo form and the Ca<sup>2+</sup>-bound protein.

The UV spectra (fig. 3.4, top panel) monitored at 25°C confirm that the hGCAP1 is characterized by a strong  $\alpha$ -helix signal at 210-220 nm, suggesting that the purified recombinant hGCAP1 is correctly folded.

Removing Ca<sup>2+</sup> from the buffer does not perturb the secondary structure content, indicating that probably all the EF-hand motifs preserve their correct fold also in the apo form.

Thermal denaturation profiles (fig. 3.4, bottom panel) were collected at the same conditions, monitoring the ellipticity at 220 nm while raising the temperature from 20°C to 95°C. The ellipticity signal of the apo protein becomes stable at 55°C suggesting a complete transition to the final state; conversely, the Ca<sup>2+</sup>-bound GCAP1 shows an incomplete transition of the thermal denaturation profile, indicative of a Ca<sup>2+</sup>-induced structure stabilization. This evidence shows that most of the  $\alpha$ -helical structures are conserved in both forms suggesting possible structural integrity of EF-hand motifs that could be functional also at extreme conditions.

The CD spectra and thermal denaturation analysis related to the D100G, E155G and E155A pathological mutants were performed by Prof. Dell'Orco group and exhaustively presented in **paper 2**.

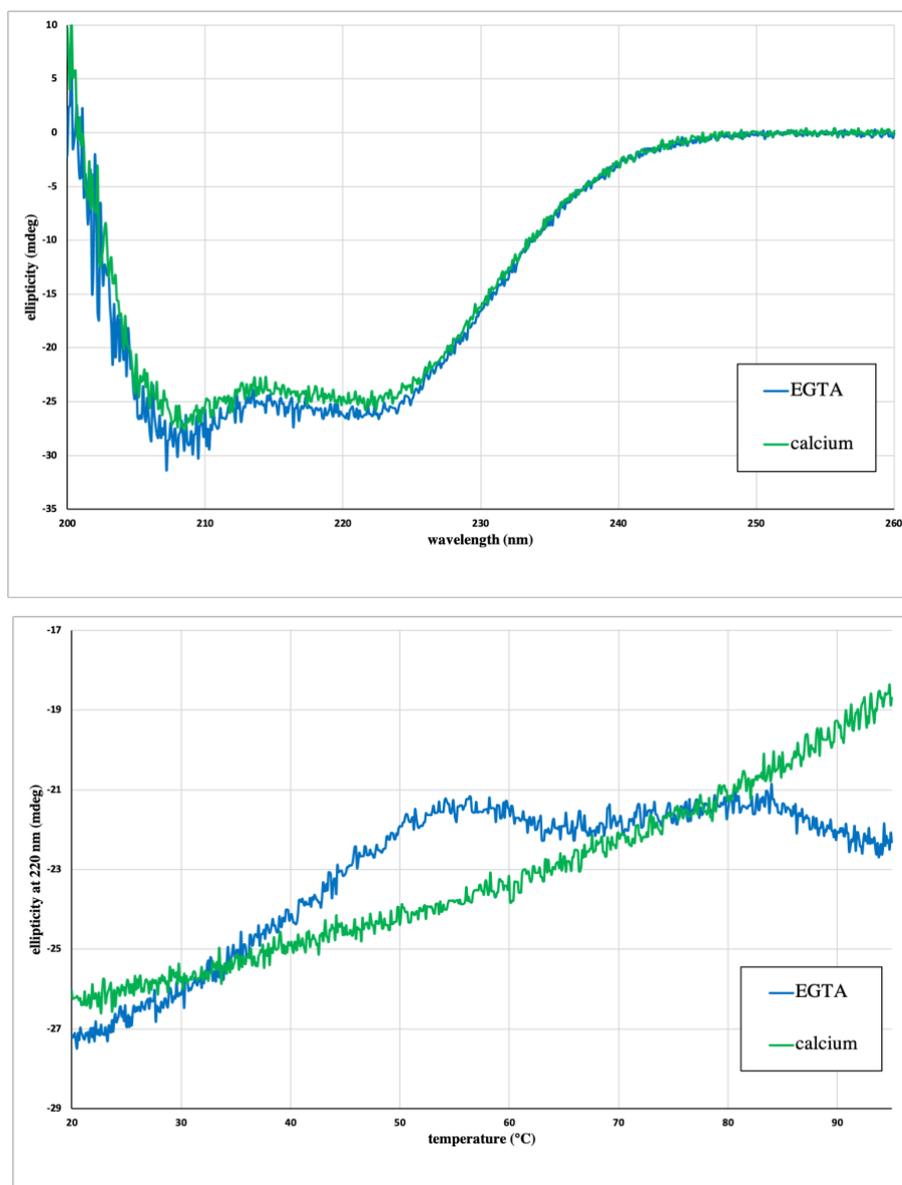


**Figure 3.4.** Top panel: far UV spectra collected with CD spectroscopy of the hGCAP1 with (green line) and without (blue line) calcium. Bottom panel: thermal denaturation of hGCAP1 with (green line) and without (blue line) calcium using CD spectroscopy, monitoring the ellipticity signal at 220 nm.

### 3.3 From dimer to monomer: the analytic SEC approach

During a preliminary optimization of the SEC purification protocol, from a comparison with the elution volume of other proteins, I observed that the elution peak of the hGCAP1 corresponded to a protein with a MW higher than the monomer. This observation induced me to suppose that hGCAP1 might form oligomeric assemblies in solution. In order to analyse the MW of the human protein in solution, I performed several experiments of analytic gel filtration in different conditions testing all the produced constructs. Using commercial MW standards for gel filtration chromatography, I initially obtained a calibration curve for the column adopted

for all the buffers from which it is possible to estimate the MW of the proteins using the relation between the elution volume ( $V_e$ ) and the LogMW. In the table below is reported the apparent MW calculated from the analytic SEC injecting 2 mg/ml of protein in a buffer with 5 mM  $\text{CaCl}_2$ . The hGCAP1 *wt*, D100G, E155G and E155A mutants are characterized by a MW compatible with a dimeric (dimeric/trimeric for D100G) assembly in solution.

In order to check whether the dimeric assembly of the *wt* protein was due to the exposure of the myristoyl moiety from its N-terminal hydrophobic cleft, I produced a not-myristoylated hGCAP1 adopting the same expression protocol without the co-transformation with pBB131-NMT1. This construct revealed to be dimeric like the *wt* protein, showing that the dimer is not dependent on a possible myristoyl switch. Also the variant *wt* $\Delta$ 12 (which I produced with a C-terminal truncation (5.2) inspired from the visible crystal structure of chicken GCAP1) shows a MW compatible with a dimer, indicating that the last 12 C-terminal amino acids are not involved in the dimerization of the protein.

hGCAP1	Elution volume (ml)	LogMW	MW (kDa)
<i>wt</i>	10.9	1.69	44
Not myr <i>wt</i>	11	1.67	47
<i>wt</i> $\Delta$ 12	11.2	1.64	44
D100G (EF3)	10.9	1.75	57
E155G (EF4)	11.3	1.62	42
E155A (EF4)	11.2	1.64	44

**Table 3.1:** apparent MW estimated by analytic SEC based on the relation between the elution volume and the LogMW obtained from a calibration curve with MW standards using a buffer with 5mM  $\text{CaCl}_2$ . The localization of the mutation for each hGCAP1 variant is reported in brackets.

The injected protein concentration of the *wt* hGCAP1 was decreased with serial dilutions up to 0.05 mg/ml and the samples were tested using the same protocol of analytic SEC to exclude that the dimer observed in solution is a purification artifact. Surprisingly, the SEC profiles showed a shift of the elution peak towards higher  $V_e$  corresponding to lower apparent MW species when GCAP1 concentration was decreased (fig. 3.5).

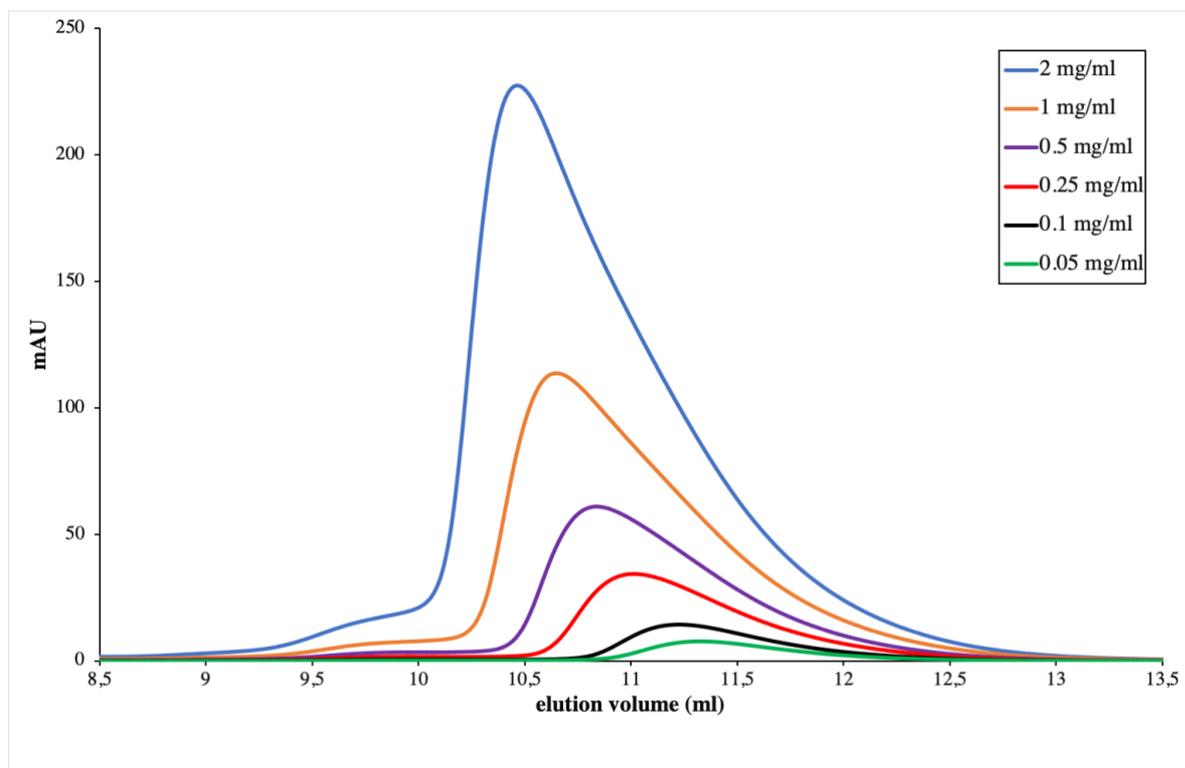


**Figure 3.5:** hGCAP1 *wt* analytic SEC elution profiles in  $\text{Ca}^{2+}$ -buffer at different protein concentrations. The elution peak shifts towards higher  $V_e$  (lower Mw) decreasing the protein concentrations.  $V_e$  (ml) is reported on the  $x$  axis, absorbance at 280 nm (mAU) is reported on the  $y$  axis.

The elution profile of each sample is not symmetric and appears to be enlarged on the right, suggesting the presence of a non-homogeneous sample consisting of both dimers and monomers which are not separated in gel filtration. This behavior prompted the assumption that hGCAP1 forms a very dynamic monomer-dimer equilibrium in solution.

To test this hypothesis, I performed the same analytic SEC experiments coupled with multi angle light scattering (MALS). From the SEC-MALS analysis (fig. 3.6) hGCAP1 was characterized by a monomer-dimer equilibrium at each of the tested protein concentrations, suggesting a concentration-dependent mechanism.

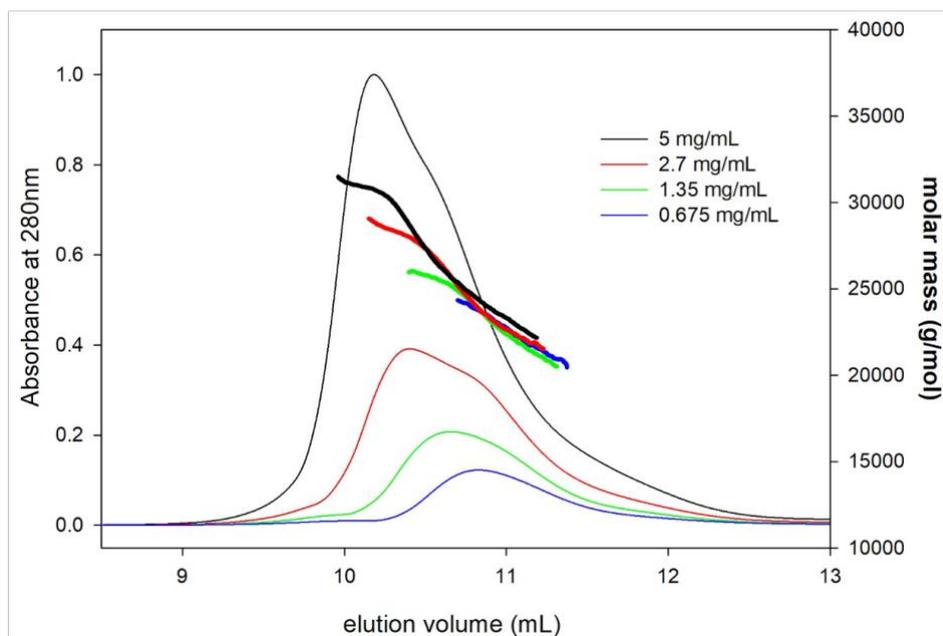


**Fig. 3.6** SEC-MALS analysis of the  $\text{Ca}^{2+}$ -bound hGCAP1 at different injected protein concentrations. The molar mass reported on the right y axis indicates the presence of a monomer-dimer equilibrium at each concentration tested.

Since all the samples tested in analytic SEC show a small peak at lower  $V_e$  (around 9.5 ml) which can not be separated from the elution peak of hGCAP1, a cross-linking experiment was performed in order to check for the presence of higher order quaternary assemblies other than dimers in  $\text{Ca}^{2+}$ -buffer. The corresponding SDS-PAGE (fig. 3.7) confirms that the only quaternary structure adopted by hGCAP1 cross-linked by BS3 in solution is the dimeric assembly.

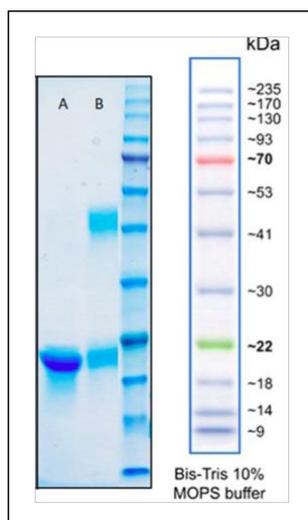


**Figure 3.7:** SDS-PAGE reporting hGCAP1 BS3-mediated dimerization. (A) negative control incubated without BS3; (B) a 46 kDa band corresponding to the GCAP1 dimer, together with the 23 kDa band of the monomer.

After proving that the monomer-dimer equilibrium depends on protein concentration, I start analysing the effects of calcium and magnesium on the dimerization of hGCAP1.

Serial dilutions of the protein were prepared in presence of 5 mM MgCl<sub>2</sub> and 2 mM EGTA to chelate all Ca<sup>2+</sup> in solution and the analytic SEC were repeated in presence of Mg<sup>2+</sup>/EGTA. The monomer-dimer equilibrium of the Mg<sup>2+</sup>-bound hGCAP1 is still characterized by a concentration-dependent trend, but it is shifted towards the monomeric form compared to the Ca<sup>2+</sup>-bound hGCAP1 (fig. 3.8). This scenario indicates that hGCAP1 dimerization is regulated both by protein concentration and by the nature of divalent ions bound to GCAP1.

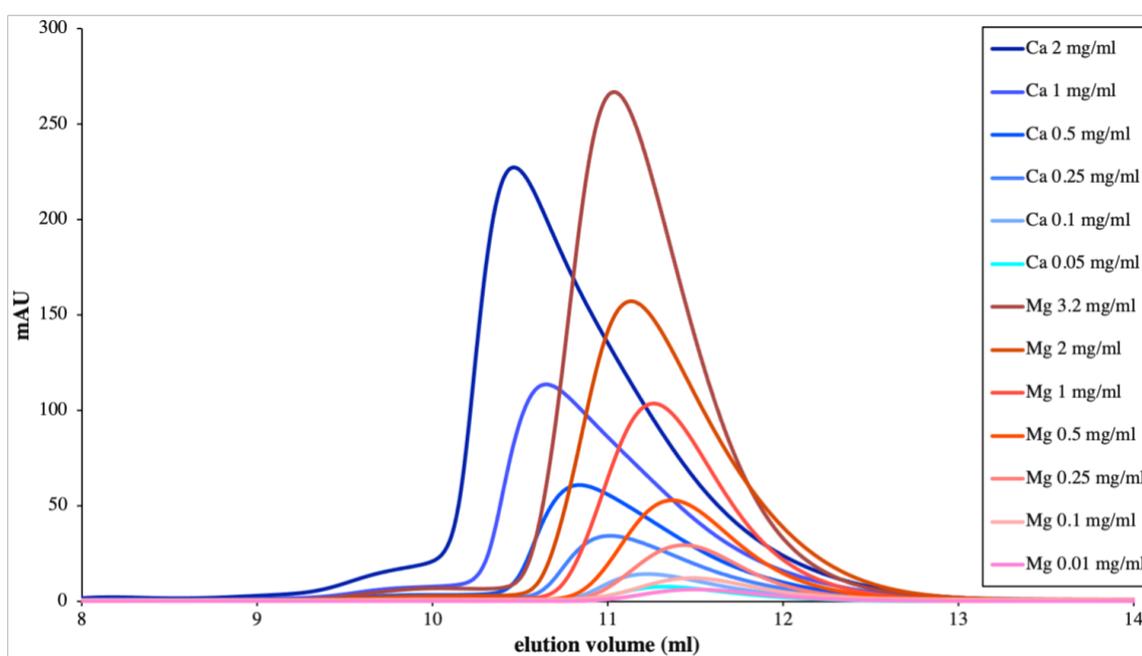


**Figure 3.8:** analytic SEC profiles comparing both the Ca<sup>2+</sup>-bound (blue gradation) and Mg<sup>2+</sup>-bound (red gradation) hGCAP1 at different concentrations reported on the right. Elution volume (ml) is reported on the x axis; absorbance at 280 nm (mAU) is reported on the y axis.

We exploited the relation between the  $V_e$  of the protein and the logarithm of its  $M_w$  which in turn depends on the monomer-dimer equilibrium that is related to protein concentration ( $c$ ) calculated from the absorbance at the elution peak (paper 1). Based on these relations, we expressed the  $V_e$  vs.  $c$  curve with an equation depending on 3 free parameters: A, B (representing the linear relation between  $V_e$  and  $\log(M_w)$ ) and the monomer-dimer dissociation constant  $K_d$  (fig.3.9).

$$V_e = A \cdot \log \left( 22.9 \cdot \left( 1 - \frac{k}{4c} \cdot \left( -1 + \left( 1 + \frac{8c}{k} \right)^{\frac{1}{2}} \right) \right) + 22.9 \right) + B$$

**Figure 3.9:** equation used to calculate the dimerization constant from analytic SEC showing the relation between  $V_e$ ,  $c$  and dissociation constant  $k$ .

Using this procedure, it was possible to determine the  $K_d$  for both  $\text{Ca}^{2+}$  and  $\text{Mg}^{2+}$ - bound hGCAP1, assessing different propensities to dimerization. By fitting the variation of  $V_e$  vs. hGCAP1 concentrations using this equation, a  $K_d = (8.8 \pm 0.7) \mu\text{M}$  was estimated for the  $\text{Ca}^{2+}$ -bound protein, which turned out to be five times lower than the one estimated for the  $\text{Mg}^{2+}$ -bound GCAP1:  $K_d = (45 \pm 15) \mu\text{M}$ .

This result clearly shows that the hGCAP1 is more prone to form dimers in solution when bound to  $\text{Ca}^{2+}$  rather than to  $\text{Mg}^{2+}$ .

The detailed results related to the monomer-dimer equilibrium analysed with SEC in presence of  $\text{Ca}^{2+}$  or  $\text{Mg}^{2+}$  are reported in **paper 1**.

### 3.4 From monomer to dimer: the MST approach

Proven that the monomer-dimer equilibrium is dependent on protein concentration and after assessing that persists at each tested concentration in analytic SEC, we assumed that hGCAP1 should be mostly monomeric at concentrations lower than the resolution limits of the column adopted for gel filtration.

MicroScale thermophoresis (MST) detects changes in the hydration shell of molecules and is used to detect interactions under close-to-native conditions. This technique is based on the measure of the concentrations of ligand-free and ligand-bound forms of a protein recording the fluorescence emission intensity of sample mixtures. For this reason, MST requires that the target protein is intrinsically fluorescent or labelled with an appropriate dye. Thanks to an infrared laser a microscale temperature gradient is produced within glass capillaries filled with the solution of choice and molecules are free to move along the temperature gradient. Upon the interaction with a ligand, the hydration shell of the target protein is influenced by possible changes in the primary, secondary, tertiary and/or quaternary structure: this affects the thermophoretic movement and thus the recorded fluorescence signal. This property can be used

to determine binding affinities with high accuracy and sensitivity. In our case, we decided to exploit this technique to study the protein-protein interaction by which the labelled hGCAP1 dimerizes with unlabeled GCAP1 monomers.

I used the *wt* protein at 20 nM concentration in order to increase the probability of labelling only the monomeric form with the NT-647-NHS fluorescent dye. A first *binding-check* trial is usually performed to test if any difference in the fluorescent signal is detected during thermophoresis. For this purpose, four capillaries were tested with the labelled hGCAP1 alone and four with the addition of 2  $\mu$ M of unlabeled protein. As reported in fig. 3.10, during MST the fluorescence curves are distributed in two distinct populations, meaning that the change in labelled protein fluorescence depends on the formation of the dimeric assembly. Thus, this technique showed to be suitable to study the dimerization process of GCAP1 starting from the monomer.

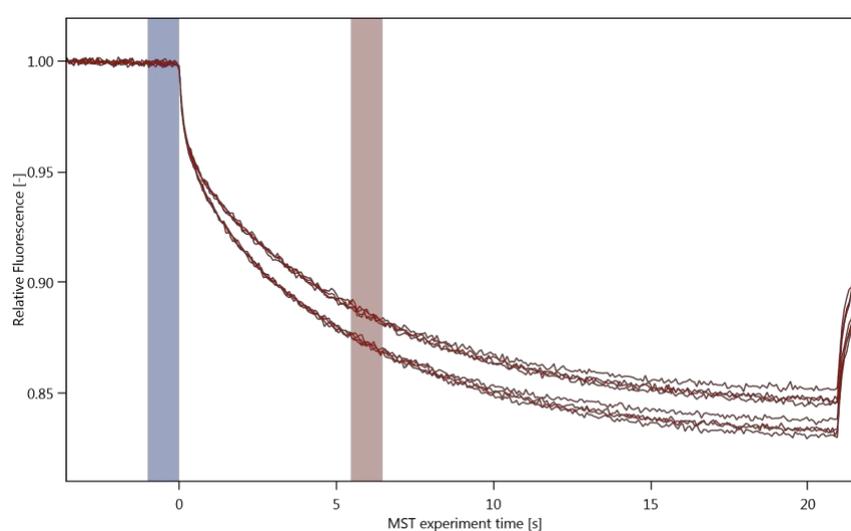


**Figure 3.10.** Binding check control in MST showing the fluorescence variation as a function of the time. The blue bar represents the onset of the gradient temperature; the red bar (at 6 sec) represents the time-frame selected to analyse the fluorescence signal.

Different MST experiments were therefore performed to calculate the monomer-dimer dissociation constants for hGCAP1 in different conditions (fig. 3.11). In particular, 16 serial dilutions of the unlabeled hGCAP1 were added to a fixed concentration of labelled protein (20 nM) in a buffer with 5 mM  $\text{CaCl}_2$ . By the interpolation of the MST data (fig. 3.11) we calculated a monomer-dimer dissociation constant for the  $\text{Ca}^{2+}$ -bound hGCAP1,  $K_d = (9.4 \pm 1.3) \mu\text{M}$  which is consistent with the value calculated from the analysis of SEC experiments.

The same experiment repeated using a buffer with 5 mM  $\text{MgCl}_2$  and 2.5 mM EGTA allowed to calculate the  $K_d$  for the  $\text{Mg}^{2+}$ -bound hGCAP1 still in agreement with the one obtained from

SEC analysis:  $K_d = (77.2 \pm 8.9) \mu\text{M}$ . This result is very similar to the  $K_d$  measured using a buffer with a combination of 5 mM EGTA / 5mM EDTA ( $K_d = 75.6 \pm 1.5 \mu\text{M}$ ) pointing out that the apo and  $\text{Mg}^{2+}$ -bound proteins behave in a similar way.

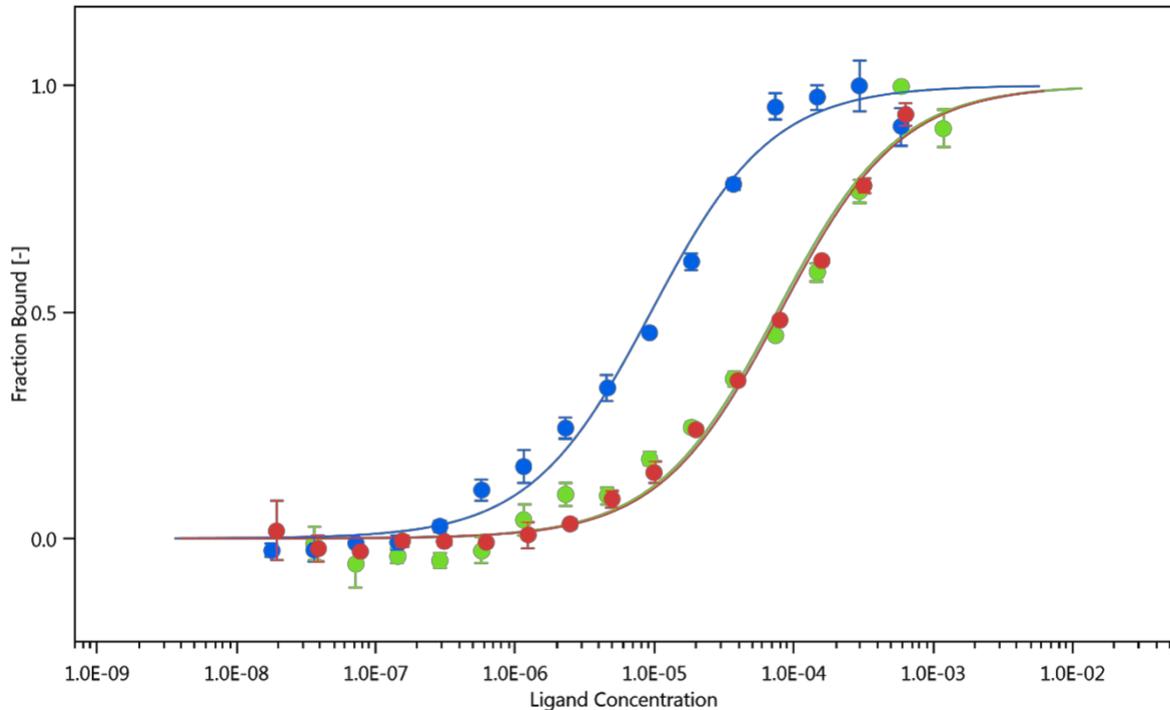


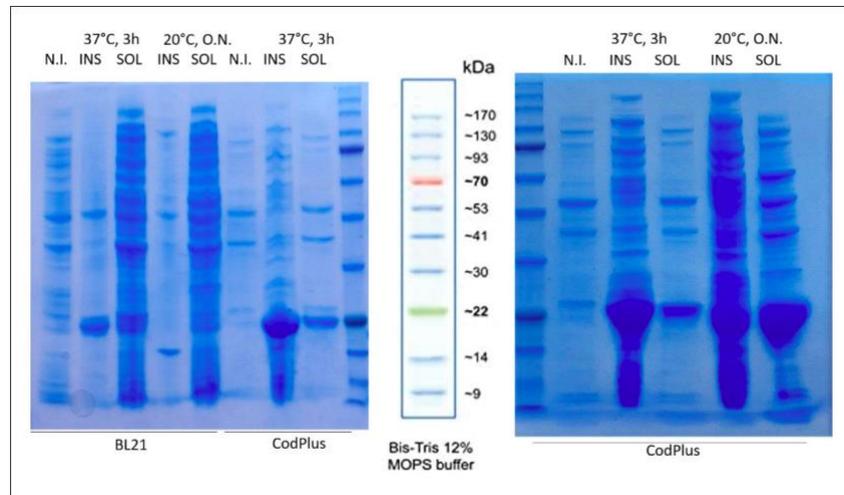
**Figure 3.11** Dimerization of hGCAP1 *wt* followed by MST. The monomer-dimer transition is measured in triplicate in each of three different conditions. Changes in labelled protein fluorescence as a function of unlabeled hGCAP1 concentration in presence of  $\text{Ca}^{2+}$  (blue line),  $\text{Mg}^{2+}$  (red line) or EGTA/EDTA (green line) together with the curve fitting the three experiments (law of mass action) in blue, red and green respectively.

### 3.5 Chicken GCAP1: an evolutionary conserved monomer-dimer equilibrium

The chicken GCAP1 (cGCAP1) was initially produced in order to try to overcome the difficulties encountered in the crystallization of the human protein since the only crystallographic structure available so far is the  $\text{Ca}^{2+}$ -bound chicken protein (pdb id: 2r2i). Because of the high sequence identity between the two proteins (80.5%), I tried to produce the cGCAP1 with the initial purpose to characterize the structural determinants of the human pathogenic mutations D100G, E155G and E155A.

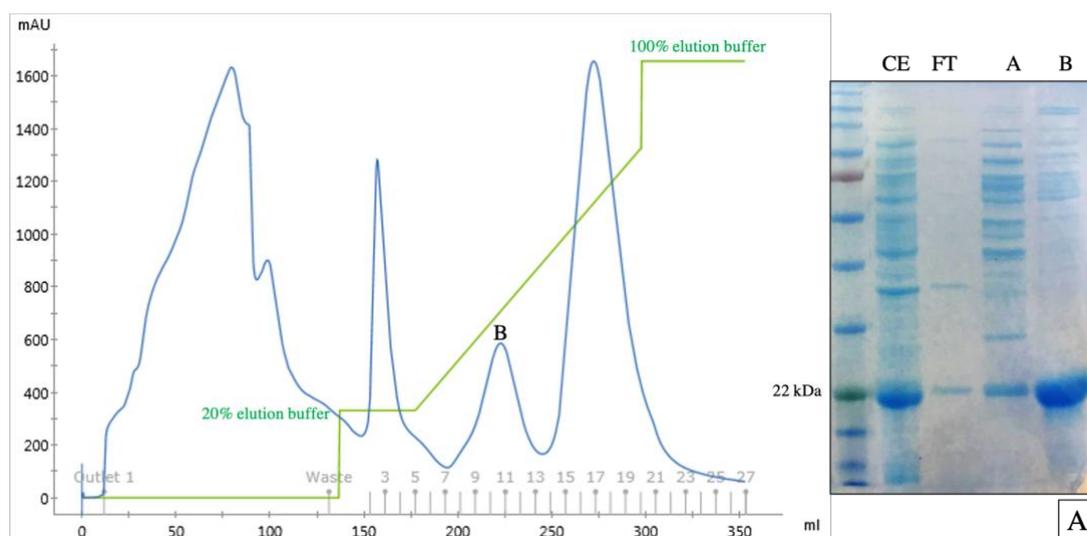
Using the same plasmid reported in literature [12] containing the coding sequence for the crystallized cGCAP1, I adopted the same expression and purification protocols used to produce

hGCAP1. Preliminary expression tests (fig. 3.12) showed once again that using the *E. coli* strain BL21 *CodonPlusRP* iis was possible to obtain the recombinant protein in the soluble form, allowing its purification from the clarified soluble extract.



**Figure 3.12:** cGCAP1 expression tests: SDS-PAGE showing BL21 *CodonPlusRP* *E. coli* cells as the only strain able to produce the protein in the soluble fraction.

Fractions from the IEC peak eluted at 50% of the buffer B (peak B, fig. 3.13 panel A) were checked in SDS-PAGE to assess the purity of the cGCAP1, pooled, concentrated and passed through gel filtration. As reported in fig. 3.13, all the fractions corresponding to the main elution peak of the SEC chromatogram displayed a high degree of purity of the chicken protein (fig. 3.13, panel B).



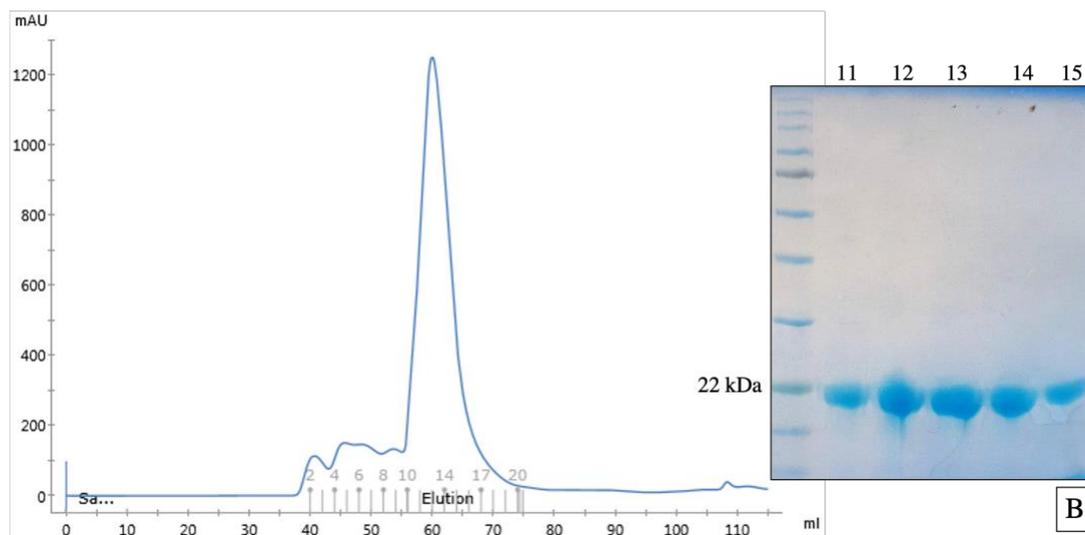


**Figure 3.13.** Purification of the cGCAP1 *wt.* Panel A: cGCAP1 IEC elution profile. Green line reports the elution buffer gradient. The main peak (B) corresponds to the overexpressed recombinant protein as shown in the associated SDS-PAGE. Panel B: cGCAP1 SEC elution profile. All the fractions corresponding to the main peak (from 11 to 15) are composed of the isolated cGCAP1 as shown in the associated SDS-PAGE.

Since the crystal structure of the chicken protein shows GCAP1 as a monomer, I investigated at first the apparent molecular weight of the fresh purified protein with analytic SEC using the same calibration curve adopted for the characterization of the hGCAP1. The first sample analysed was the  $\text{Ca}^{2+}$ -bound protein injected at 2 mg/ml concentration which was characterised by an elution peak at 11.35 ml. Based on the column calibration curve, the  $V_e$  corresponds to a molecule with a MW of 42 kDa compatible once again with a dimeric assembly.

This unexpected result on the cGCAP1 suggested a possible similarity about the monomer-dimer equilibrium in solution observed for the hGCAP1 which was not reported in literature [12]. To test this hypothesis, I repeated the analytic SEC with serial protein dilutions also on the  $\text{Ca}^{2+}$ -bound and  $\text{Mg}^{2+}$ -bound cGCAP1. As shown in fig. 3.14, the elution peak of the protein shifted toward higher  $V_e$  by decreasing the concentration of the injected protein. This trend characterises both the  $\text{Ca}^{2+}$ -bound and  $\text{Mg}^{2+}$ -bound forms, suggesting that a monomer-dimer equilibrium persists also for the chicken protein with a concentration-dependent mechanism.

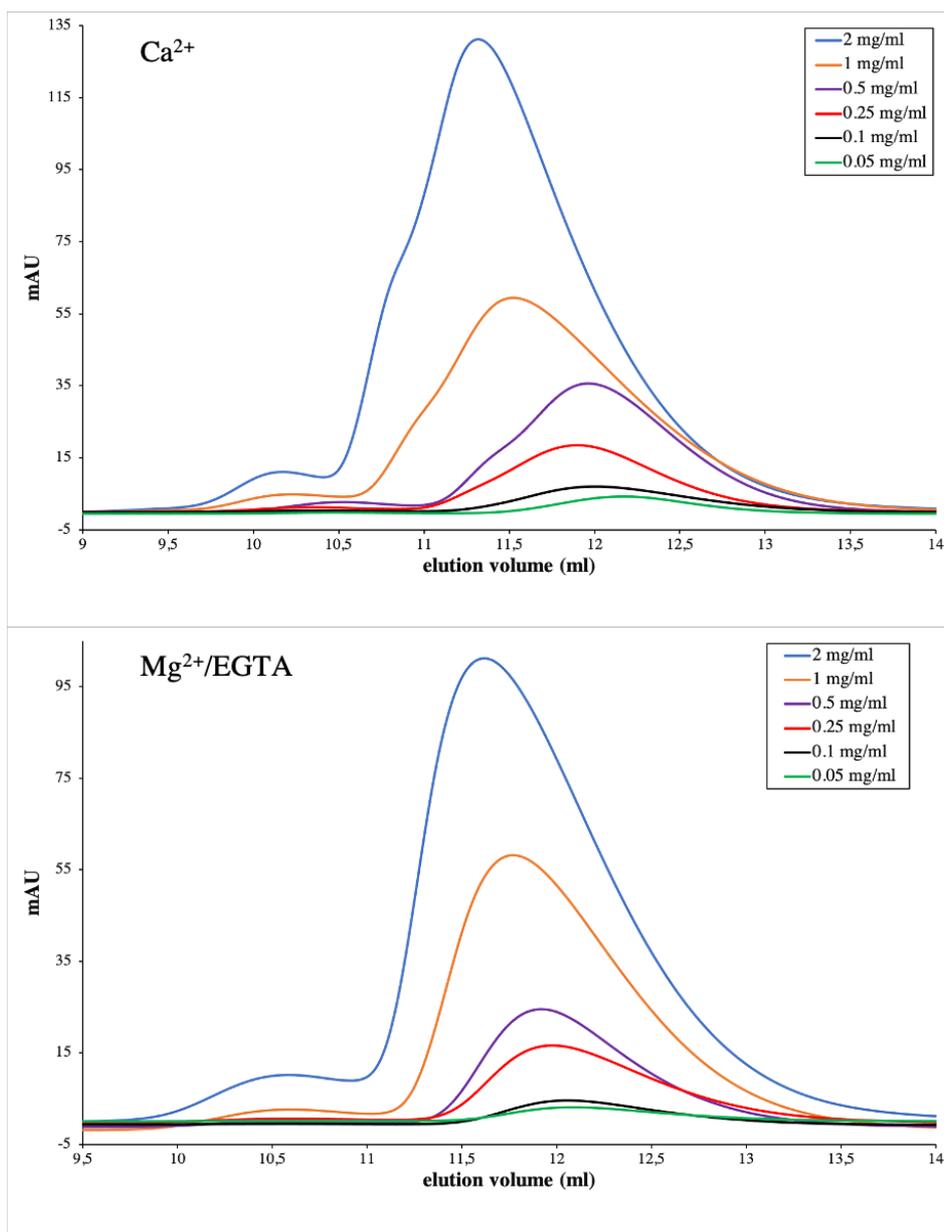


**Figure 3.14:** cGCAP1 analytic SEC chromatograms in  $\text{Ca}^{2+}$  buffer (upper panel) or  $\text{Mg}^{2+}/\text{EGTA}$  buffer (lower panel) at different protein concentrations (legend on the right). Elution volume (ml) is reported on the  $x$  axis; absorbance at 280 nm (mAU) is reported on the  $y$  axis.

Moreover, the elution profiles of the  $\text{Ca}^{2+}$ -bound form present a shoulder on the left of the main peak, meaning that probably higher order oligomeric assemblies coexist in solution with dimers and monomers of cGCAP1. All the species in solution can not be resolved with SEC probably due to the high dynamicity of the quaternary equilibria.

Nevertheless, by a qualitative comparison of the normalized elution curves, cGCAP1 shows a different monomer-dimer equilibrium depending on the nature of the ion bound (fig. 3.15). In particular, the  $\text{Ca}^{2+}$ -bound protein seems to be more prone to dimerize with respect to the  $\text{Mg}^{2+}$ -

bound form as already shown for the human GCAP1, suggesting that the monomer-dimer equilibrium is a conserved feature of GCAP1 in the two species.

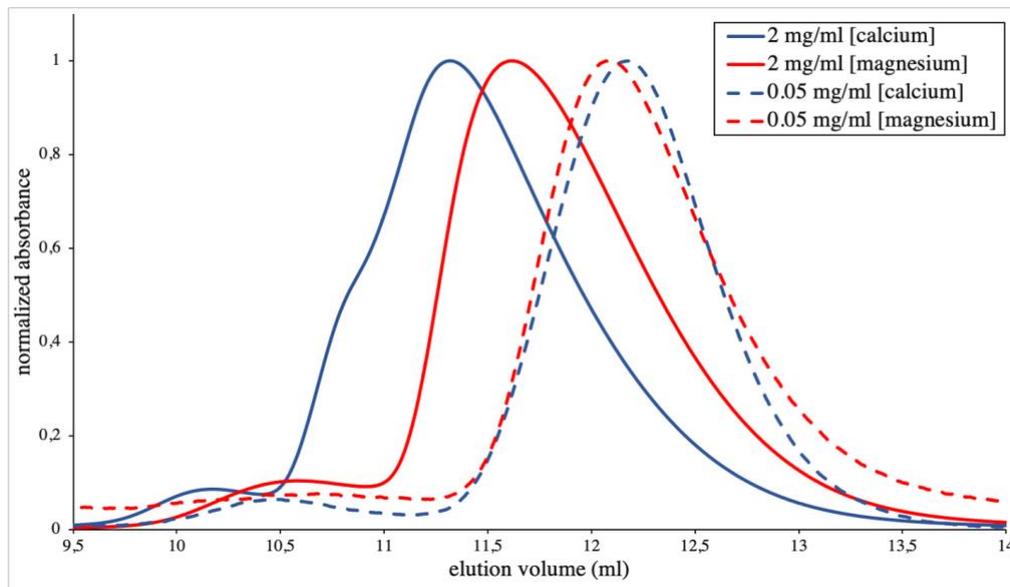


**Figure 3.15:** Analytic SEC chromatograms comparing different concentrations of cGCAP1 both in  $\text{Ca}^{2+}$  and  $\text{Mg}^{2+}$  buffers, respectively represented in blue and red lines. The higher  $\Delta V_e$  observed for the  $\text{Ca}^{2+}$ -bound form suggests a lower  $K_d$  as observed for hGCAP1. Elution volume (ml) is reported on the x axis, normalized absorbance at 280 nm (mAU) is reported on the y axis.

### 3.6 GCAP1 dimerization is affected by ionic strength

Since all the crystallization trials performed with the cGCAP1 resulted in small quasi-crystals or not diffracting crystals (3.7 paragraph), I decided to modify the purification protocols adopted for the cGCAP1 with the addition of a hydrophobic interaction chromatography (HIC) as reported in [12]. Accordingly, the purified chicken protein was loaded on a HiPrep PhenylFF 16/10 column with a buffer composed of 20 mM TrisHCl pH 7.5, 300 mM NaCl, 5 mM  $\beta$ -mercaptoethanol. Most of the protein bound the resin as can be noted from the low  $A_{280}$  of the unbound fraction (FT, fig. 3.16). The wash with the same buffer reported in [12] - with 4 mM EGTA - did not allow to elute the protein from the resin, even after 150 ml. In order to recover the protein from the column, I adopted the typical approach used for HIC which consists in the decreasing of salt concentration by using the same elution buffer without NaCl and EGTA. As can be seen in the chromatogram, cGCAP1 slowly eluted from the resin although most of the

bound fraction was recovered only washing the resin with water. Since the GCAP1 immobilized into the resin has been washed with several volumes of EGTA and NaCl was removed, I consider the protein purified with this treatment as the apo-GCAP1.

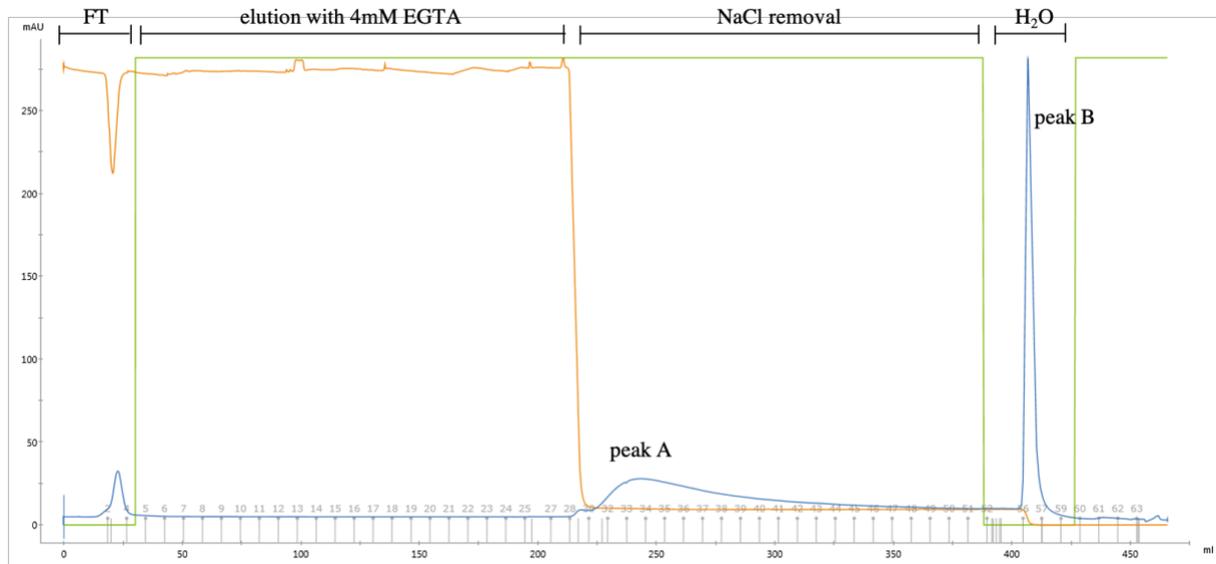


**Figure 3.16:** HIC chromatogram of the cGCAP1. The green line corresponds to protein elution. The orange curve reports the conductance related to the salt concentration measured after the column. The chromatographic steps are indicated on top: FT (flow through) represents the unbound fraction; elution with 4 m EGTA; NaCl removal was performed with the same elution buffer without EGTA and NaCl; H<sub>2</sub>O was used to wash the resin. Elution volume (ml) is reported on the x axis, absorbance at 280 nm (mAU) is reported on the y axis.

After checking by SDS-PAGE that all the elution peaks obtained in HIC were composed of pure cGCAP1, I investigated the oligomeric state of the protein with analytic SEC. The peak B recovered from HIC (in water) eluted with the void volume of the SEC column, meaning that the sample is composed of aggregates or oligomers too large for the used resin. The peak A, eluted with a  $V_e$  of 9.8 ml, corresponds to an apparent MW of 85 kDa. Interestingly, by the addition of 20 mM trisHCl, 5 mM  $\beta$ -mercaptoethanol to the sample of peak B, the elution volume changed to the one already observed for peak A (fig. 3.17).

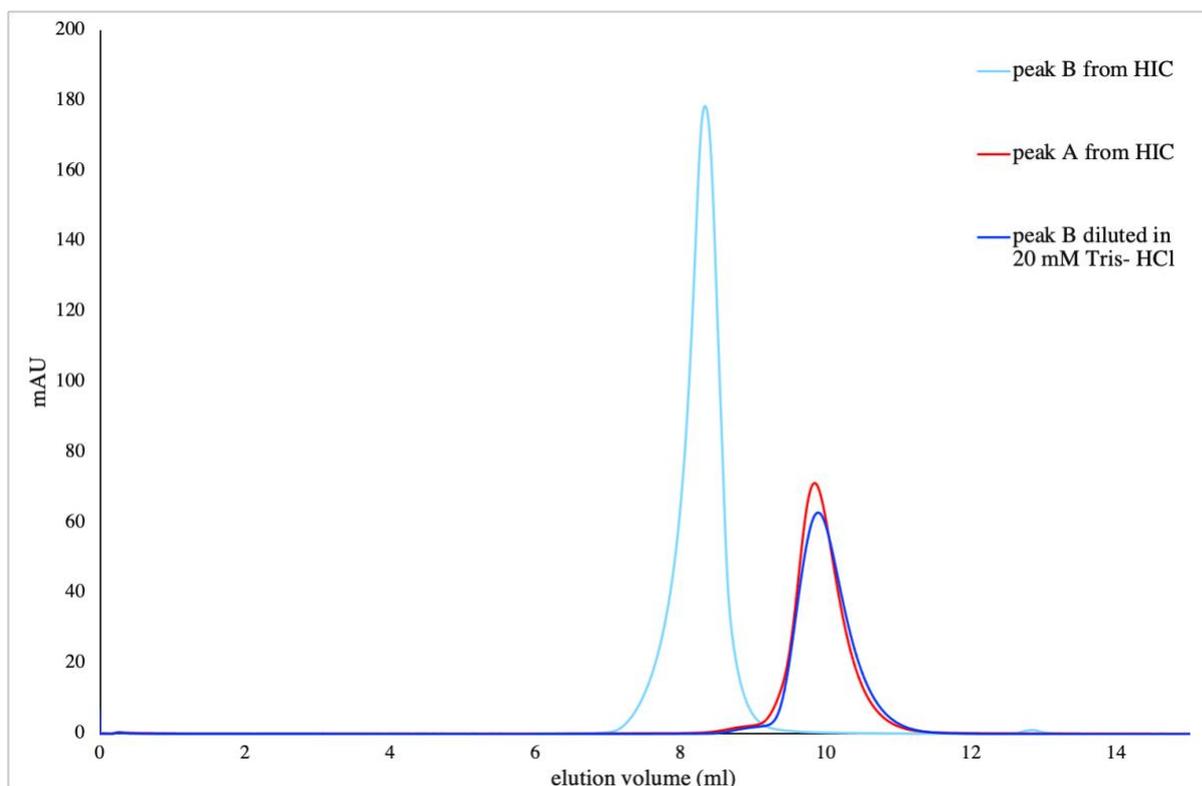


**Figure 3.17:** analytic SEC of the cGCAP1 elution peaks obtained in HIC. The elution volume is reported on the  $x$  axis; the absorbance at 280 nm (mAU) is reported on the  $y$  axis. By diluting with 20 mM Tris-HCl the cGCAP1 eluted in water (peak B) during HIC, its SEC elution peak corresponds to the peak A obtained in HIC.

cGCAP1 has been investigated to assess if the monomer-dimer equilibrium persists also at low ionic strength (using a buffer without NaCl, composed of 20 mM Tris/HCl pH 8.0 and 5 mM DTT).

Accordingly, four serial protein dilutions of GCAP1 were tested in analytic SEC experiments adopting the same protocol used in the previous SEC analyses.

Unexpectedly, at low ionic strength all the tested concentrations were characterized by the same elution volume (fig. 3.18, panel A), indicating that the monomer-dimer equilibrium is shifted toward one of the two forms. The same result characterized also hGCAP1 (purified in EGTA buffer and desalted in order to obtain the apo-hGCAP1) which was tested at two protein dilutions (fig. 3.18, panel B).

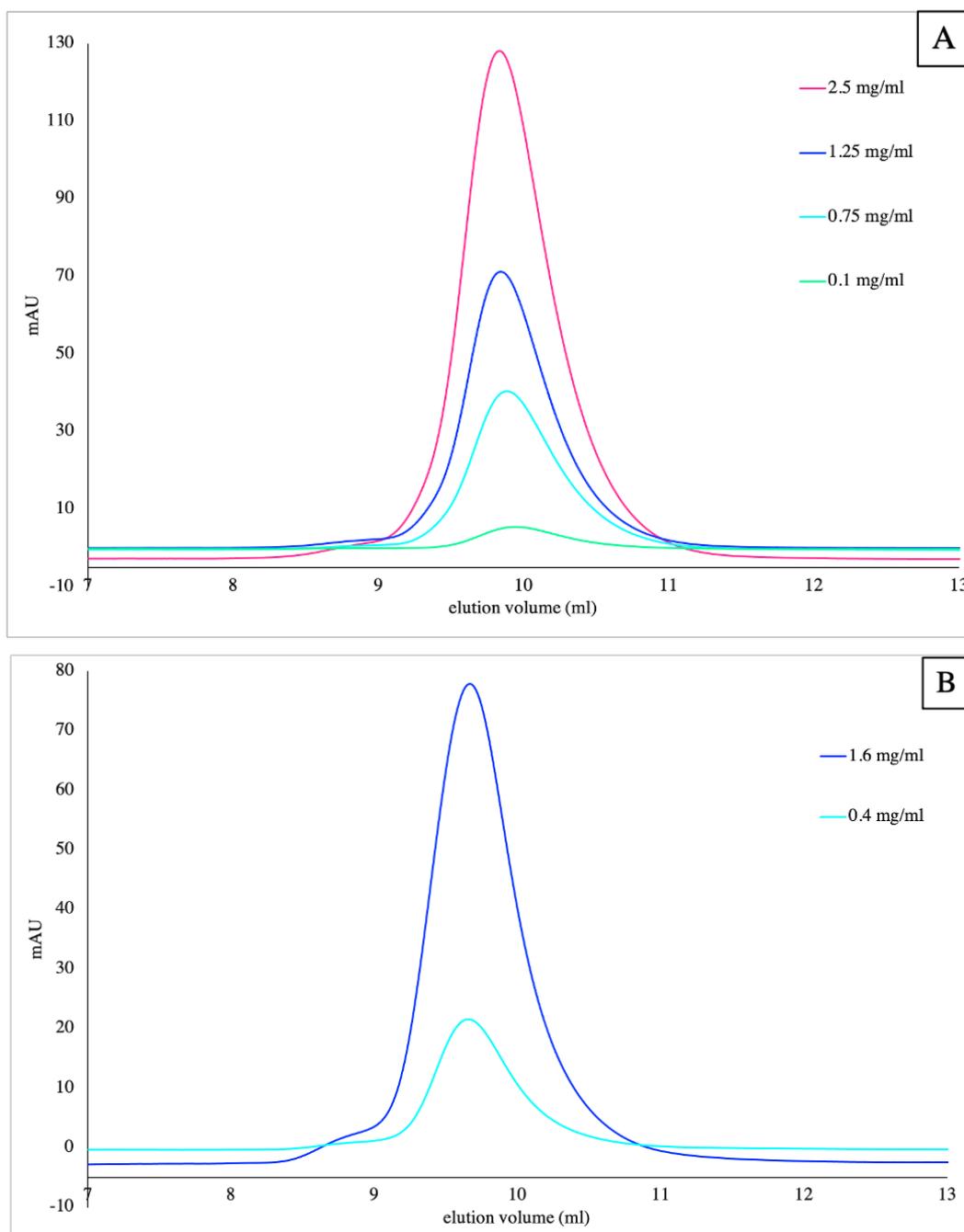


**Figure 3.18.** Analytic SEC chromatograms comparing different concentrations of cGCAP1 in a buffer at low ionic strength. Elution volume (ml) is reported on the x axis; absorbance at 280 nm (mAU) is reported on the y axis.

Nevertheless, a more detailed characterization of this low ionic strength state was required. Hence, SEC was coupled to MALS with the aim to determine with more accuracy the MW of the apo-cGCAP1.

From the analysis of the molar mass along the elution peak (fig. 3.19, panel A), I discovered that the estimated MW of the apo cGCAP1 and apo hGCAP1 were respectively 21.8 kDa and 22.8 kDa, concluding that the apo GCAP1 adopts a pure monomeric form at low ionic strength.

This implies that the monomer-dimer equilibrium is completely shifted toward the monomer when salt is removed from the buffer.

Therefore, I took advantage of the monomeric GCAP1 observed with SEC-MALS to understand the role of  $\text{Ca}^{2+}$  in the dimerization process of both the chicken and human GCAP1. Using the same experimental conditions of low ionic strength, I added 1 mM  $\text{CaCl}_2$  in the SEC buffer and analysed the MW of the protein with MALS. As shown in fig. 3.19 (panel B), the cGCAP1 monomer-dimer equilibrium is promptly recovered upon the addition of  $\text{Ca}^{2+}$  in the buffer without NaCl, as proved by the increased molar mass (25 kDa), indicating that the divalent ion plays a crucial role in the dimerization process. This effect is even more striking for the human protein MW (29 kDa) and reported in detail in **paper 1**.

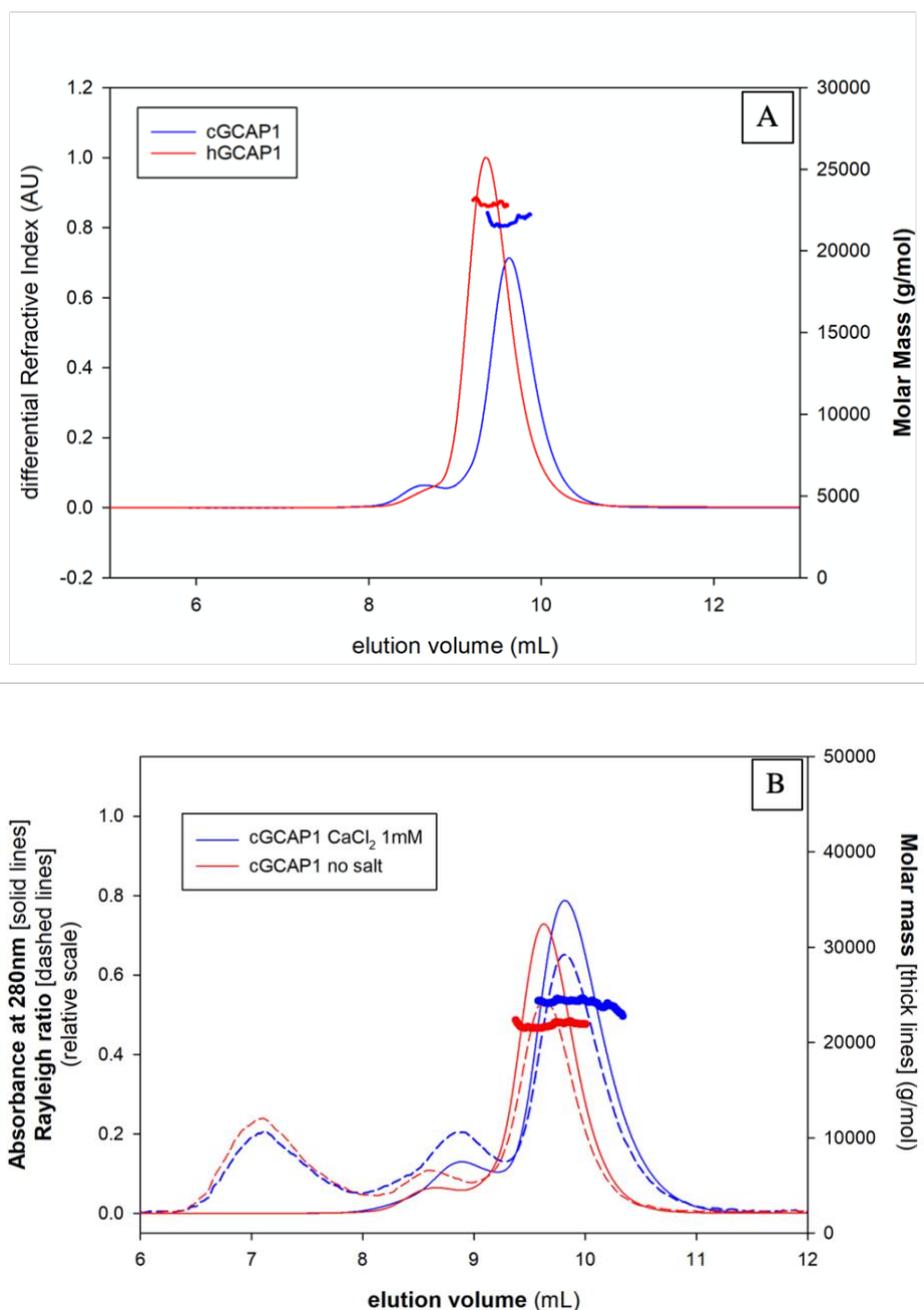


**Figure 3.19.** SEC-MALS analysis of the apo hGCAP1 and apo cGCAP1: at low ionic strength the measured MW of both human (red curve) and chicken (blue curve) protein corresponds to the GCAP1 monomer (panel A). Panel B: SEC-MALS cGCAP1 chromatography showing the recovery of the monomer-dimer equilibrium upon calcium binding. The elution peak at low ionic strength (red chromatogram) shifts towards higher molar mass species when calcium is added (blue chromatogram). Elution volume (ml) is reported on the x axis, absorbance at 280 nm (mAU) on the left and molar mass (g/mol) on the right.

By the observation of the elution profiles of both the hGCAP1 and cGCAP1 with and without  $\text{Ca}^{2+}$ , we discovered an inverted distribution of the elution peaks. Indeed, the monomeric GCAP1 elutes before the  $\text{Ca}^{2+}$ -bound form which is a monomer-dimer equilibrium. This behavior is in agreement with the analysis of the hydrodynamic radius of GCAP1 in the two different conditions (fig. 3.20). Both the apo protein and the  $\text{Ca}^{2+}$ -bound form are characterised

by a similar hydrodynamic radius in the salt-free buffer. Such evidence suggests that the GCAP1 monomer, at low-ionic strength, displays an open non-compact structure, potentially partially unfolded.

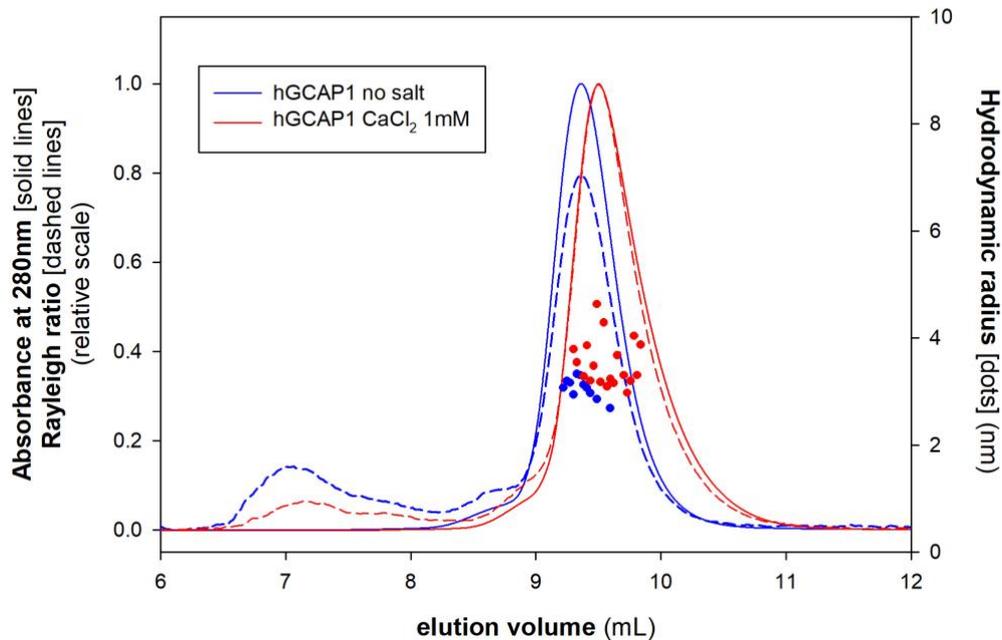


**Figure 3.20** SEC-MALS analysis of the hydrodynamic radius of hGCAP1 without NaCl. Monomer-dimer equilibrium recovery upon  $\text{Ca}^{2+}$  addition is confirmed by the change in hGCAP1 elution volume. The monomer displays a hydrodynamic radius (blue dots) comparable with the one of the monomer-dimer equilibrium (red dots). Elution volume is reported on the  $x$  axis, absorbance at 280 nm (mAU) on the left and hydrodynamic radius (nm) on the right.

## 3.7 Crystallization trials of the human and chicken GCAP1: an engineered construct

### 3.7.1 Full length GCAP1

Several crystallization trials of the hGCAP1 *wt* and the mutants D100G, E155G and E155A were carried out along the three years of my PhD work in order to solve the crystal structure of the human protein and get structural insights of the pathological variants.

I used different crystallization methods (*i.e.* vapor diffusion sitting/hanging drop, microbatch) coupled with different temperatures and protein/precipitant ratios using commercial screening

solutions and manual optimization of the most promising crystalline precipitates for more than 3,000 different crystallization conditions tested.

The only positive result obtained with the full-length *wt* hGCAP1 was an apparent *quasi* crystalline precipitate grown in conditions similar to those reported for the cGCAP1 [12]. Such a sample was analysed with Second Harmonic generation (SHG - Multiphoton microscopy) signal as reported in 5.7 by scanning the crystalline precipitate with a 200 fs laser exciting at 1064 nm. A signal at 532 nm emission wavelength was recorded (fig. 3.21), proving that this precipitate is actually formed by micro-crystals of protein since only a sample composed of chiral crystals can produce a second harmonic wave characterized by half the wavelength of the incident light. A possible future approach on this kind of crystalline precipitate could be micro electron diffraction experiments aimed at collecting diffraction data of the hGCAP1.

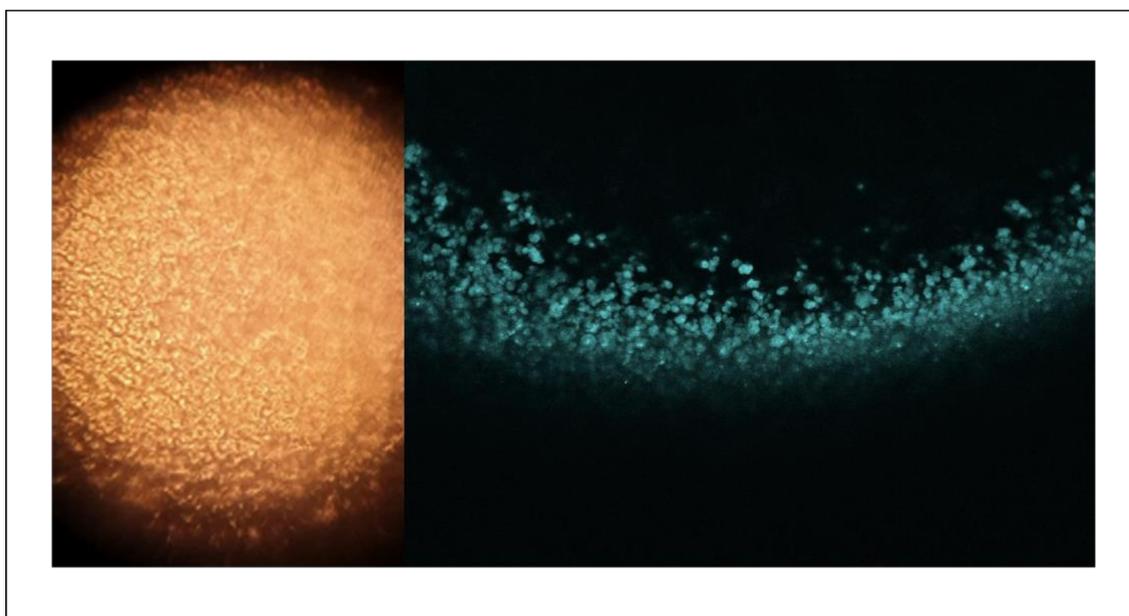


**Figure 3.21.** Second Harmonic Generation (SHG) - Precipitate observed at 25X magnification (left). Second harmonic wave emission (right) demonstrates the crystalline nature of the precipitate; excitation: 1064 nm; emission: 532 nm.

As mentioned before, I exploited the sequence homology between human and chicken GCAP1 in order to replicate the crystals of the chicken protein and obtain structural information on the human pathological variants using the cGACAP1 scaffold.

I tested several commercial crystallization screenings together with screening based on the published crystallographic conditions (ammonium sulphate optimizations) of the cGCAP1. Despite all these trials, the only positive hint was represented by small irregular *quasi-crystals* obtained at 2.2 M ammonium sulphate, 0.1 M Tris/HCl pH 8.0 with a combination of 70% protein and 30% precipitant. This was the only sample positive for *Izit Crystal Dye HR4-710*

coloring, indicating that the dye can penetrate in the solvent channels of the protein crystals (fig. 3.22).

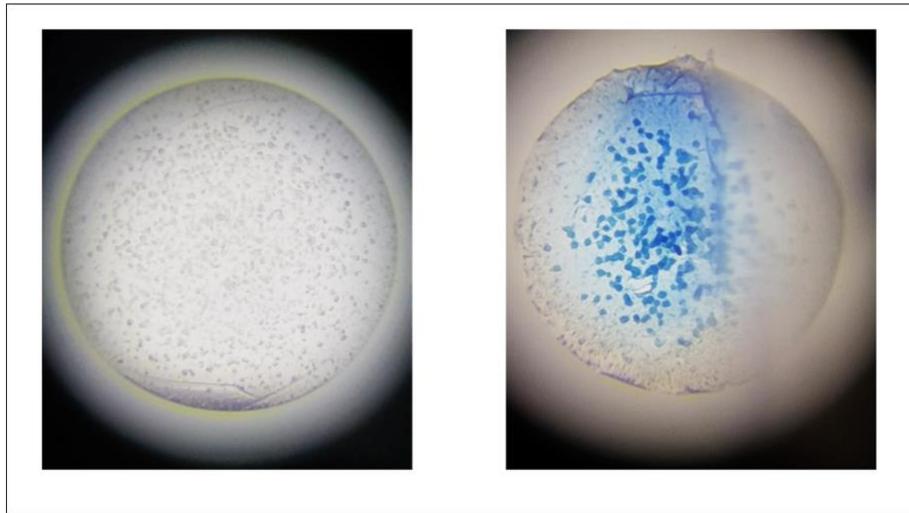


**Figure 3.22** cGCAP1 wt *quai*-crystals positive for *Izit Crystal Dye HR4-710* at 10X magnification formed in 2.2 M ammonium sulphate, 0.1M Tris HCl pH 8.0.

### 3.7.2 Limited proteolysis: a stable fragment of hGCAP1

Trypsin mediated limited proteolysis experiments were initially performed to investigate any possible conformational difference between  $\text{Ca}^{2+}$ -bound and  $\text{Mg}^{2+}$ -bound hGCAP1 that could be detected by different proteolytic patterns.

Interestingly, after incubating overnight the proteolysis reaction at 37°C a fragment of about 15/16 kDa resistant to proteolytic cleavage was detectable for both the  $\text{Ca}^{2+}$  and  $\text{Mg}^{2+}$  -bound isoforms (fig. 3.23).

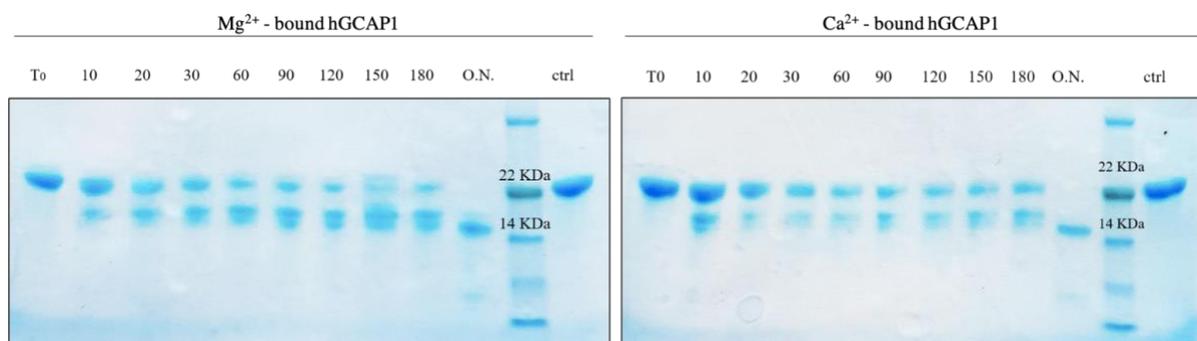


**Figure 3.23** Limited proteolysis reactions of the  $\text{Mg}^{2+}$ -bound and  $\text{Ca}^{2+}$ -bound hGCAP1 analysed in SDS-PAGE displaying a conserved proteolytic pattern from 10 to 180 minutes of incubation and after overnight digestion.

Analytic SEC was used to investigate the behavior in solution of the stable fragment (at about 15 kDa) obtained by trypsin-mediated overnight digestion at two protein concentrations (1 mg/ml and 0.2 mg/ml). From the analysis of the SEC elution profiles reported below (fig. 3.24) the  $V_e$  of this fragment does not change with protein concentration, not showing any apparent monomer-dimer equilibrium.

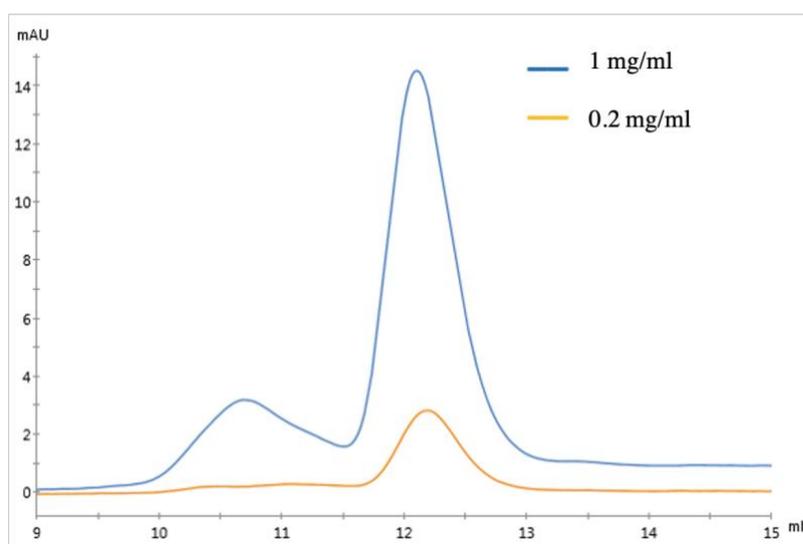


**Figure 3.24** Analytic SEC of hGCAP1 proteolysed fragments at different protein concentrations. Elution volume (ml) is reported on the x axis; absorbance at 280 nm (mAU) is reported on the y axis.

Assuming that this fragment may have originated from the loss of flexible regions that prevent the crystallization of GCAP1, I scaled up the proteolytic reaction and tried to purify with SEC the aforementioned fragment for crystallographic purposes.

By comparing the elution peaks A and B obtained with SEC (fig. 3.25) it appears evident that further proteolysis occurred maybe because the scaled up reaction did not work properly. A great amount of protein was detected in the insoluble fraction. However, few crystallization trials were performed using the fragment purified from the peak B. Two commercial crystal screens (HT<sup>TM</sup> Hampton Research and JCSG – *plus*<sup>TM</sup>, Molecular Dimensions) were used in combination with an optimization of the crystallization condition reported in literature for the cGCAP1 structure. Although no diffracting crystals were obtained, further information about this fragment could be obtained by mass spectrometry analysis in order to understand which is the stable core of the protein resistant to trypsin proteolysis.

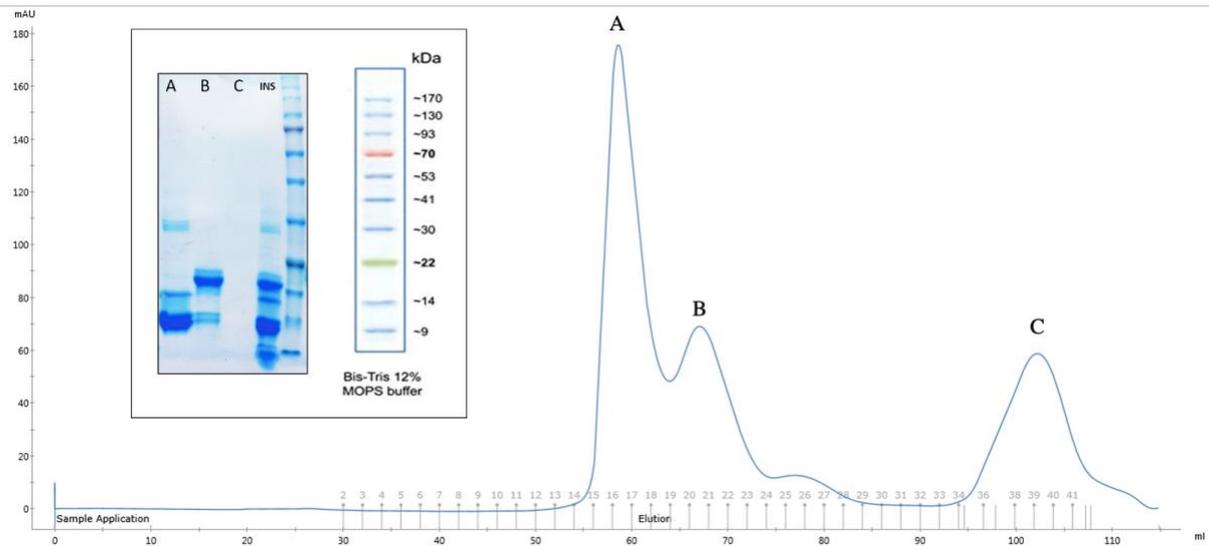


**Figure 3.25** SEC chromatogram of hGCAP1 proteolysed by trypsin with the corresponding fractions analysed by SDS-PAGE. Elution volume (ml) is reported on *x* axis; absorbance at 280 nm (mAU) is reported on the *y* axis.

### 3.7.3 GCAP1 wt $\Delta$ 12 Q58C/A118C: stabilization of GCAP1 with a disulfide bridge

From a sequence-based prediction of hGCAP1 disordered residues using PrDos software, the N-terminal and C-terminal portions of hGCAP1 were predicted as the most disordered regions. Moreover, by the observation that the C-terminal portion is not modeled in the chicken crystal structure and since the N-terminal portion should be stabilized by the myristoyl group, a variant of hGCAP1 lacking the final twelve C-terminal residues (wt $\Delta$ 12) was produced in order to obtain a new construct characterized by a higher structural stability likely suitable for crystallization.

A STOP codon was inserted in place of E190 residue by site-directed mutagenesis (E190STOP). The mutation was confirmed by DNA sequencing and the recombinant short construct was successfully expressed and purified with the same protocols adopted for the full-length protein. Despite all the crystallization trials performed, no diffracting crystals were obtained.

Hence an additional double mutation was introduced in the wt $\Delta$ 12 construct again with the aim to produce a further reduction of the protein flexibility at the interface between EF-2 and EF-3 domains.

Q58 from EF-2 and A118 from EF-3 were identified as two conserved residues close enough to promote the formation of a disulfide bridge (fig. 3.26). Thus, the two residues were

mutagenized in Q58C and A118C in order to obtain the double cysteine substitution shown on the crystal structure of the cGCAP1 reported below as model.

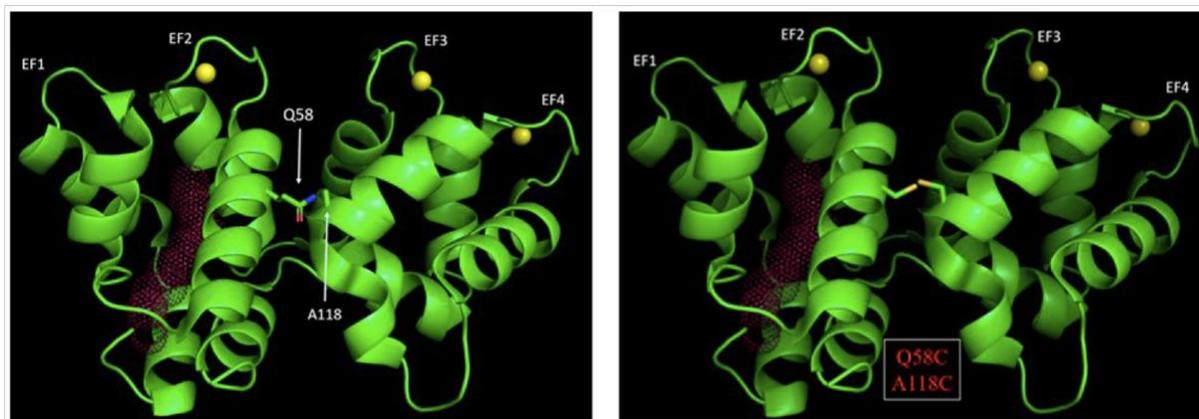


**Figure 3.26** *In silico* model of Q58C/A118C double mutant. Residues Q58 and A118 (left cartoon) were mutated in cysteine using PyMOL on the cGCAP1 template.

From preliminary expression trials in *E.coli* I found that the highest soluble fraction of the cell extract containing the wt $\Delta$ 12 Q58C/A118C was expressed in SHuffle cells (an *E.coli* strain with enhanced capacity to correctly fold proteins with multiple disulfide bonds in the cytoplasm) grown overnight at 20°C.

Although the purification yield was lower respect to wt GCAP1, I modified the expression protocol to increase the overall amount of the recombinant protein. The purification protocol used for the full-length GCAP1 was successfully applied to the wt $\Delta$ 12 Q58C/A118C variant with a final buffer composed of 20 mM Tris/HCl pH 8.0, 100 mM NaCl, 1 mM DTT, 5 mM CaCl<sub>2</sub>.

The protein was concentrated to 10 mg/ml and some commercial crystallization screen solutions were tested in vapor diffusion crystallization experiments. From the very first crystallization trials I found a condition (fig. 3.27) in which nice crystals grew in relatively short times (20% w/v polyethylene glycol 10,000, 0.1 M HEPES pH 7.5). A few crystals were tested for X-ray diffraction, but they turned out to be too small to fish and embedded in the film-like surface of the crystallization drop. An optimization of the purification protocol and crystallization conditions is currently going on in order to decrease the number of crystallization nuclei and to try to increase the crystals size.

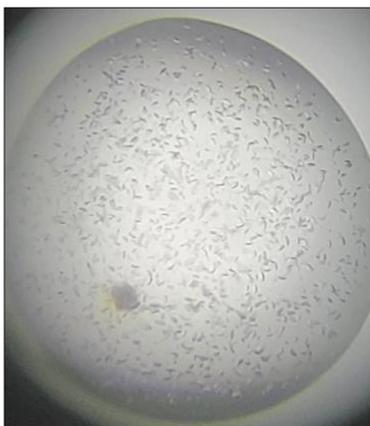


**Figure 3.27:** crystals obtained in vapor diffusion (sitting drop) with 20% w/v polyethylene glycol 10,000, 0.1 M HEPES pH 7.5, as precipitant solution.

The activity of this construct has been investigated at Oldenburg University with the supervision of Prof. Karl Koch in order to understand if the probable reduction of protein dynamicity and the absence of the C-terminal tail induced any change in the regulatory activity of the guanylate cyclase. As reported in fig. 3.28, the recombinant double mutant is able to regulate the retGC1 activity as well as the *wt* full-length GCAP1 with the same  $\text{Ca}^{2+}$ -sensitivity. This preliminary result reveals that by removing the 12 C-terminal residues the regulatory activity of GCAP1 is preserved thus the C-terminal tail appears to be not involved in the regulation of the retGC1. Moreover, once confirmed the formation of the disulfide bond, this experiment represents the proof of concept that the *wt* $\Delta$ 12 Q58C/A118C protein is a reliable hGCAP1 model with biological relevance.

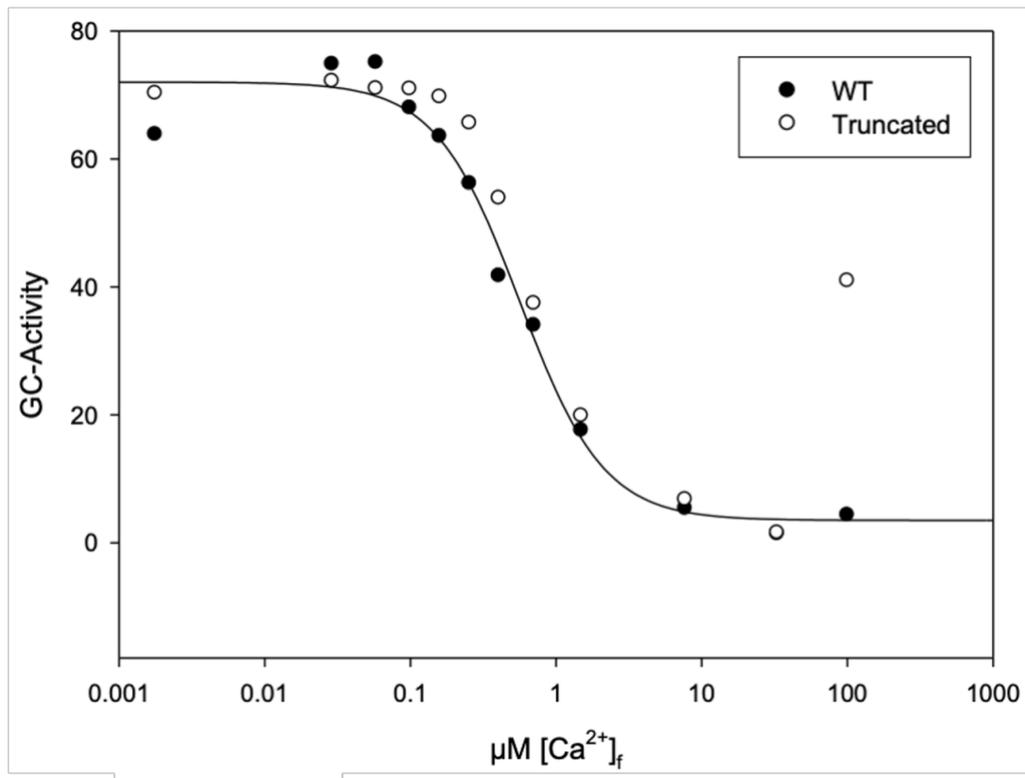


**Figure 3.28** Comparison of the wt GCAP1 and wt $\Delta$ 12 Q58C/A118C (truncated) regulatory activity on the guanylate cyclase (y axis) at different  $\text{Ca}^{2+}$  concentrations (x axis).

### 3.8 Small Angle X-ray Scattering (SAXS): a low-resolution model of the hGCAP1 dimeric assembly

Despite the large number of crystallization trials and all the different constructs produced, a crystal structure of the hGCAP1 protein is still missing. Therefore, during my PhD experience, I performed several SAXS measurements at European Synchrotron Radiation Facility (*ESFR* - Grenoble) and Diamond Light Source (*DLS* - Oxford) in order to better characterize the monomer-dimer equilibrium and to produce low resolution models of the dimeric assembly.

All the experimental conditions and the detailed results concerning the modeling of the hGCAP1 dimer are reported in **paper 1**.

Briefly, SAXS allowed us to confirm that the monomer-dimer equilibrium depends both on protein concentration and the nature of the divalent ion bound to GCAP1.

Coupling SAXS with HPLC we showed that at low concentration the human apo protein (5 mM EGTA) is monomeric. The monomer-dimer equilibrium was observed by increasing the protein concentration and using a buffer with 5 mM CaCl<sub>2</sub> and 5 mM MgSO<sub>4</sub>. In particular, the data collected at high protein concentration (~76 μM) showed a prevalent dimeric assembly and were used to select between different possible dimeric models of the hGCAP1, built using the program zdock [47] and exploiting the distance constraints of the dimeric bovine homologue recently reported by Lim et al. in [33].

SAXS data of the D100G, E155G and E155A pathological mutants were collected in batch mode at different protein concentrations in presence of saturating concentration of Mg<sup>2+</sup> and Ca<sup>2+</sup>.

By the analysis of the molecular weight, we discovered that also the three variants are characterized by different equilibria between oligomeric species in solution dependent on protein concentration. Interestingly, we found that only the E155G variant shows a monomer-dimer equilibrium, while the D100G and the E155A variants showed molecular weights compatible with a dimer/trimer and with a trimer/tetramer assembly, respectively. We were able to produce a low-resolution model of the E155G variant which suggests a partial independence of the four EF-hand motifs probably due to the higher flexibility of the Gly with respect to the Glu. Together these data point out a more complicated scenario at the base of the cone dystrophy in which the pathological mutations could perturb not only the tertiary structure of GCAP1 but also its quaternary assembly.

The SAXS analysis of the D100G, E155G and E155A mutants are published as part of the detailed characterization of the GCAP1 pathological variants in **paper 2**.

### **3.9 Retinal Guanylate Cyclase 1: efforts to produce the retGC1/GCAP1 complex**

Assuming that in photoreceptors GCAP1 is located close to the retGC1, I tried to express and purify a retGC1/GCAP1 complex with the aim of obtaining high-resolution data on the mechanism of interaction between the two proteins. RetGC1 is a protein of about 1100 amino acids located in the membrane of rod outer segment with an intracellular catalytic domain of 560 amino acids. The interaction with the regulatory GCAP1 should occur via the retGC1 juxtamembrane domain (JMD) involving two close protein segments: amino acids 492-503

and 554-573 [48]. Therefore, I tried first to express and purify the isolated intracellular portions of the retGC1 predicted to interact with GCAP1. All the DNA constructs used for the expression of retGC1 were kindly provided by Prof. Karl-Wilhelm Koch (Oldenburg University).

The first vector I worked with contained the juxtamembrane domain (JMD) and the kinase homologous domain (KHD) of the retGC1 and was previously known to produce an insoluble recombinant protein. Therefore, I co-transformed *E. coli* cells with the two plasmids coding for retGC1 and GCAP1 in order to try to exploit the second protein as a driver of the correct folding of the first protein upon the formation of the complex. Although the co-transformation worked properly for all the *E. coli* strains tested (*BL21*, *CodonPlus*, *SHuffle*, *Tuner*) the expression induced with IPTG led to the production of the retGC1 construct alone and the presence of GCAP1 was not detectable. Unfortunately, retGC1 construct turned out to be insoluble and despite the attempts to refold it from inclusion bodies I was not able to produce a soluble form.

The second construct I tested was composed of a N-terminal His-tagged maltose binding protein (MBP) as driver of solubility, a small linker region with a TEV protease restriction site and the retGC1 JMD-KHD domains. Even though I successfully produced and purified the MBP-JMD-KHD in a soluble form, the JMD-KHD gave rise to insoluble aggregates whenever the MBP was cleaved by TEV protease, preventing once again from obtaining a soluble retGC1/GCAP1 complex.

Thus, I decided to produce the whole soluble cytoplasmic domain of the retGC1 (from H485 to S1103) composed of the JMD, KHD, dimerization domain (DD) and catalytic domain (CD). This construct was cloned into a pIEX/Bac3 plasmid, designed for the expression of recombinant proteins in insect cells using the baculovirus expression vector system (BEVs). The availability of this construct was particularly useful during my PhD as it allowed me to improve my expertise in the production of recombinant proteins using eukaryotic cells. First, since no fusion tag was associated with retGC1 coding sequence in the provided pIEX/Bac3 plasmid, I inserted an N-term 6xHis-tag and a thrombin recognition site (confirmed by DNA sequencing).

In order to produce the recombinant bacmid, *Sf9* insect cells were co-transfected with the recombinant pLEX/Bac3 plasmid and the commercial BacMagic viral DNA. An even monolayer (fig. 3.29) of  $1 \times 10^6$  cells/ml was treated according to the protocol reported in 5.9.

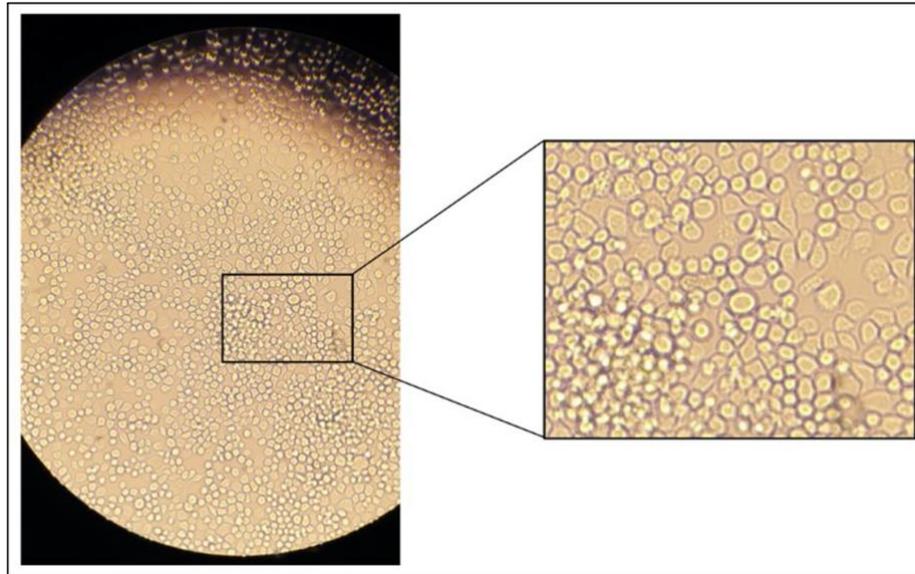


**Figure 3.29** Co-transfection of *Sf9* cells at 10X magnification (phase-contrast microscope). Transfected cells appear irregular and enlarged with respect to non-transfected cells.

*Sf9* cells were incubated at 28°C for five days post-transfection. The viral progeny P0 was collected from the growth medium harvesting the cells at 1000 x g for ten minutes. Because of its low viral titer, P0 was used to infect a fresh preparation of *Sf9* cells in order to be amplified. Different P0 dilutions (1:100, 1:500, 1:5000) were inoculated into 50 ml of *Sf9* cells and incubated with shaking. Cellular growth was monitored day by day until a remarkable growth stop was registered (after 4-5 days) indicating a proper infection rate.

As reported in figure 3.30, 1:100 and 1:500 P0 dilutions stopped their growth respectively at three and four days post infection. Thus, cells infected with these P0 dilutions were centrifuged at 1000 x g for ten minutes and the supernatants containing progeny 1 (P1) recombinant baculovirus were stored at 4°C.

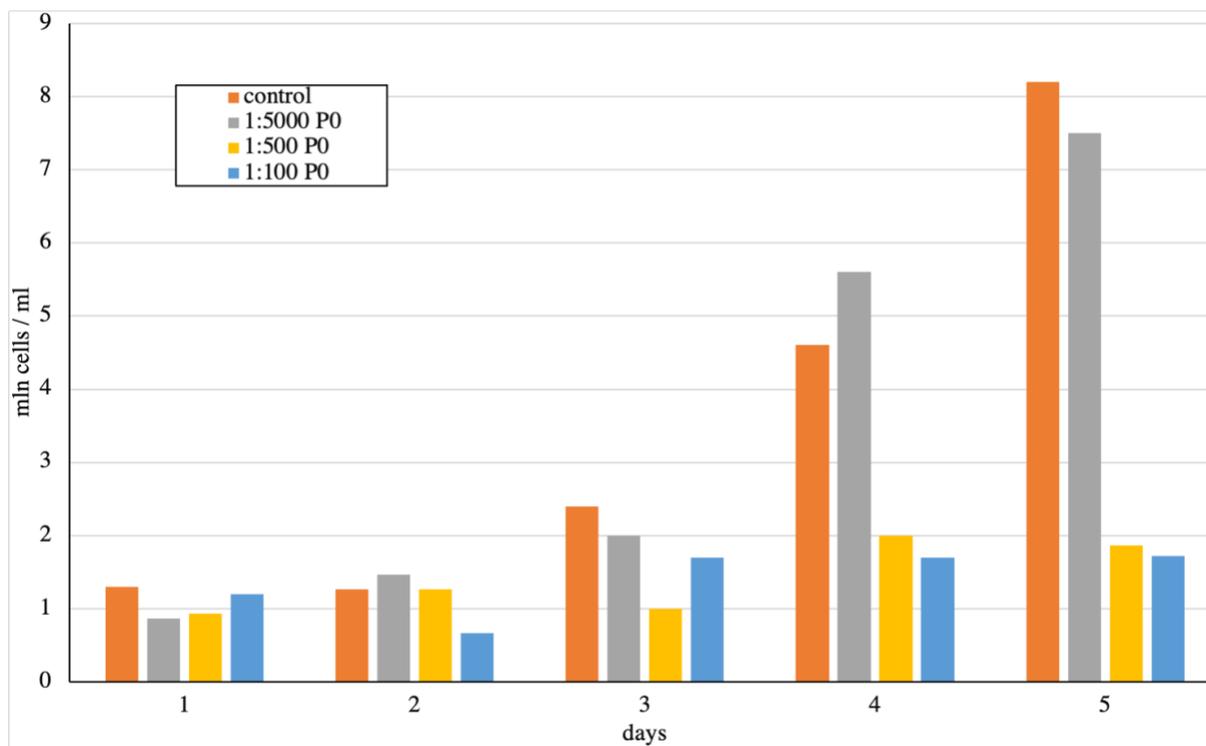


**Figure 3.30:** P1 recombinant baculovirus amplification from P0. Sf9 cells growth monitoring at three different P0 dilutions. Days post infection are reported on the x axis; number of cells (mln/ml) are reported on y axis.

Expression trials of the soluble cytoplasmic domain of retGC1 were performed infecting  $1 \times 10^6$  cells/ml of a new fresh Sf9 preparation with different P1 dilutions in order to find out the experimental condition with a multiplicity of infection (m.o.i.) closest to 1.

Cells were monitored for 96 hours (fig. 3.31) and 2 ml for each condition of the cell growth were centrifuged at  $1000 \times g$ , resuspended in loading buffer (Tris-HCl pH 7.5, 500 mM NaCl, 5 mM imidazole) and sonicated for 30 seconds in order to perform in small scale an affinity chromatography (Ni-NTA) in batch mode.

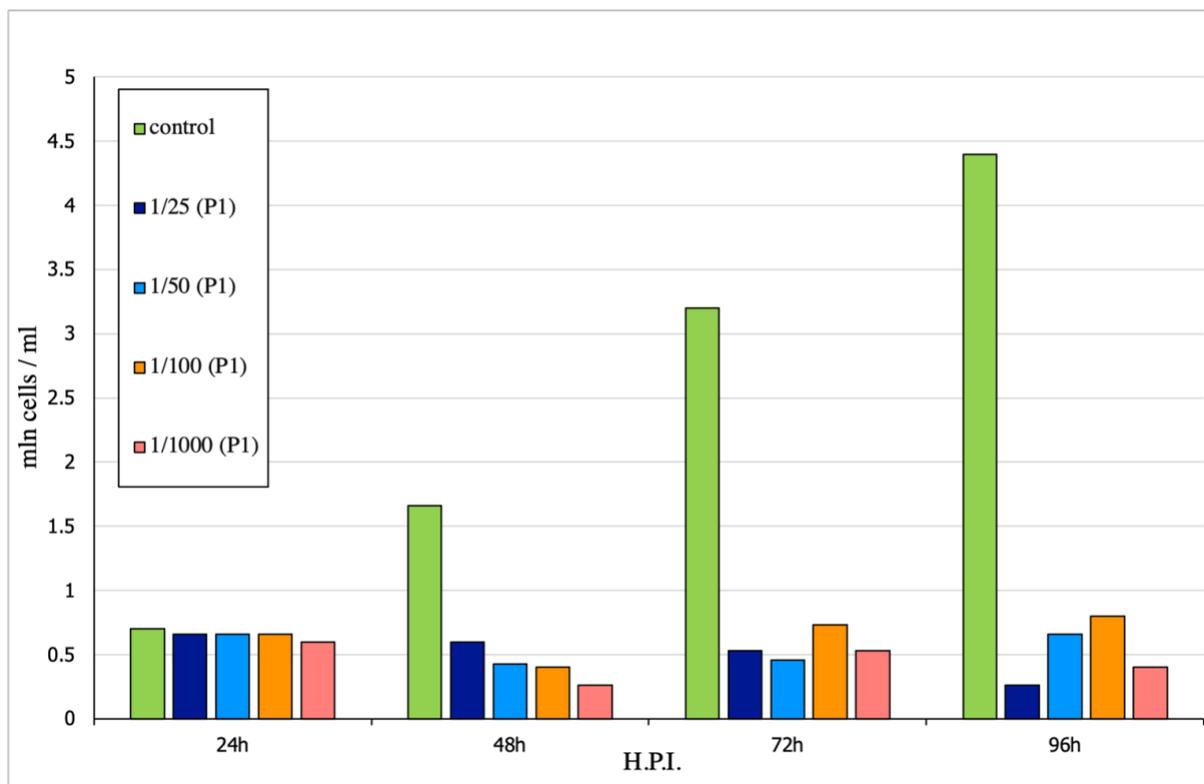


**Figure 3.31:** Sf9 cells growth monitoring at four different P1 dilutions. Time (hours post infection) is reported on the x axis, number of cells (mln/ml) is reported on the y axis.

Samples were centrifuged at 14,000 rpm in an Eppendorf bench centrifuge for 20 minutes in order to separate the soluble and insoluble fractions and incubated for one hour with 60  $\mu$ l of slurry  $\text{Ni}^{2+}$ - resin previously equilibrated with the loading buffer. Elution was performed using 60  $\mu$ l of elution buffer (50 mM Tris-HCl pH 7.5, 500 mM NaCl, 1 M imidazole). 30  $\mu$ l of the eluted samples were analysed by SDS-PAGE to check the presence of a band at  $\sim$ 70 kDa, corresponding to the cytoplasmic domain of the retGC1.

The SDS-PAGE reported below (fig. 3.32) is an example of the results obtained by analysing the expression at 72 hours post infection (H.P.I.). None of the different expression conditions tested presented the expected band, probably indicating that the expression level of retGC1 is too low in *Sf9* cells to be detectable with SDS-PAGE. A western blot using an antibody anti-retGC1 should clarify if the recombinant protein is actually produced. Thanks to a recent collaboration with San Raffaele's laboratory (Milan) we will repeat the expression tests using *Hi5* insect cells which are known to improve the expression levels of recombinant proteins with BEVs.

Another possible interpretation of these preliminary results could be an inefficient homologous recombination of the pIEX/Bac3 plasmid and the viral DNA during co-transfection in *Sf9* cells which resulted in the production of too low amount of recombinant P0. This in turn could have

caused the excision of the retGC1 DNA from the viral genome, resulting in an amplified P1 composed only by non-recombinant baculovirus. This issue could be overcome by repeating the co-transfection trying different pIEX/Bac3: viral DNA ratios.

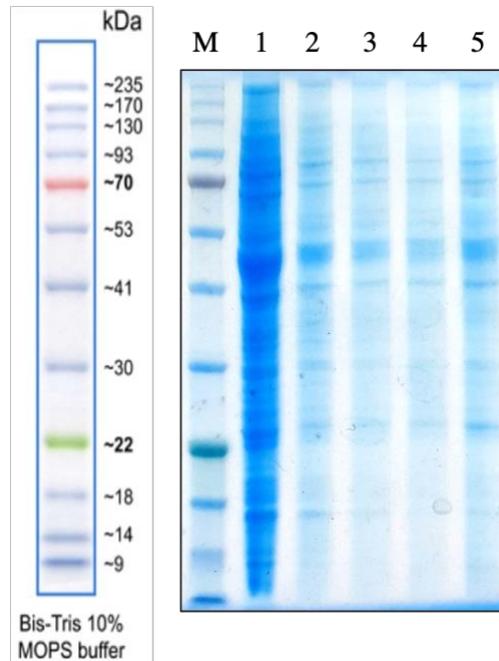


**Figure 3.32** SDS-PAGE corresponding to the retGC1 expression trials in *Sf9* insect cells at 72 H.P.I. M: protein ladder, 1: control, 2: 1/25 P1 dilution; 3: 1/50 P1 dilution; 4: 1/100 P1 dilution; 5: 1/1000 P1 dilution.

### 3.10 Identification of EF1-targeted compounds: a preliminary screening

The modulation of the retGC1 activity occurs through EF-1 and EF-2 motifs of GCAP1. Such a region of the protein was considered a good target for an *in silico* docking aimed at the identification of small molecules able to modulate the aberrant regulatory activity of the pathogenic GCAP1 variants.

The rationale for such approach is related to different potential effects of the selected ligands: these molecules could

- i.* alter the binding mode of the pathogenic GCAP1 mutants to the cyclase, restoring their regulatory activity;
- ii.* promote the preferential binding of the *wt* protein in people carrying just one copy of the defective gene (autosomal dominant disease);

iii. promote a compensatory effect of GCAP2 in people carrying two copies of the defective gene.

The *in silico* docking was performed using the *wt* cGCAP1 crystal structure (pdb-id: 2r2i) as reference model, considering the mutational analysis of Peshenko et al. [41]. A grid of 22x22x22 Å<sup>3</sup> was centered on Phe41 of the EF-1 motif and 30,000 different compounds from the “hit2lead” library ([www.hit2lead.com](http://www.hit2lead.com)) were analysed with the program *autodock-vina* [49] for a fast preliminary screening. A more detailed molecular docking was performed using AutoDock4 with the best 100 compounds ranked from the first docking.

Ten compounds with the best predicted free energy of binding were purchased and tested using MST to investigate the binding with the *wt* hGCAP1. Most of them revealed to be highly insoluble while only three showed a K<sub>d</sub> in the millimolar range. These three compounds were used as templates to search for analogues with a higher solubility aimed at improving the binding affinity to GCAP1. I carried out the MST measurements testing both a hGCAP1 labelled on cysteine (NT-647-MALEIMIDE fluorophore) and a hGCAP1 labelled on lysine (NT-657-NHS fluorophore). I observed only a few positive MST results with the Lys-labelled hGCAP1, indicating that the covalently bound fluorophore probably interfered with the binding of the compounds. All the reported K<sub>d</sub> are therefore related to MST analyses performed using the Cys-labelled hGCAP1.

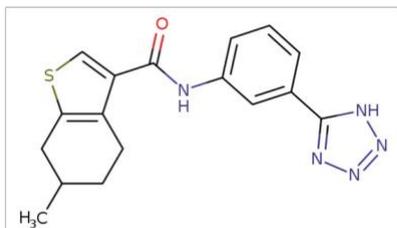
I identified four molecules (fig. 3.33) able to bind to the hGCAP1 with a K<sub>d</sub> in the micromolar range:

- **compound 3:** 6-methyl-N-[3-(1H-1,2,3,4-tetrazol-5-yl)phenyl]-4,5,6,7-tetrahydro-1-benzothiophene-3- carboxamide
- **compound 7:**  
N-{[2-(benzyloxy)pyridin-3-yl]methyl}furan-3-carboxamide
- **compound 10:** N-[3-(1H-1,2,3,4-tetrazol-5-yl)phenyl]-4,5,6,7-tetrahydro-1-benzothiophene-2-carboxamide
- **compound 12:** 3,5-diacetamido-N-(3-methyl-2,3-dihydro-1,3-benzothiazol-2-ylidene)benzamide

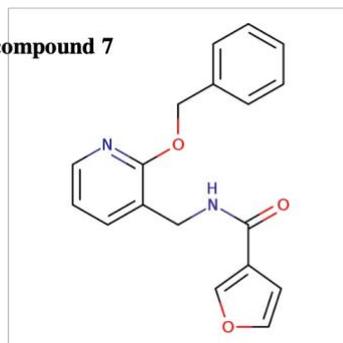
The binding affinity of these compounds for hGCAP1 could be further ameliorated by looking for other soluble analogues or by modifying them with different substituent groups. Before proceeding to improve their binding affinity, some preliminary enzymatic assays on the retGC1

regulation in presence of these compounds should be done in order to assess a possible biological activity of the selected molecules in complex with GCAP1.

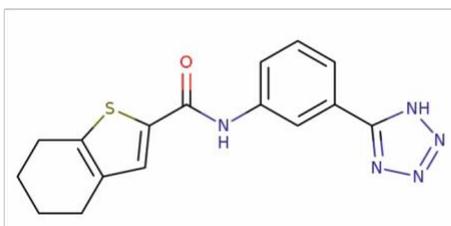
**compound 3**



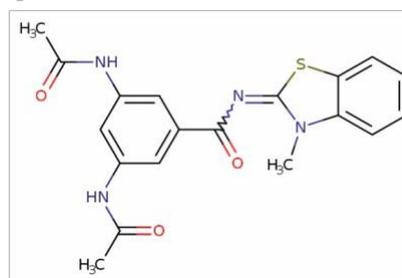
**compound 7**



**compound 10**



**compound 12**



<b>compound</b>	<b>Kd</b>
3	500 $\mu$ M
7	850 $\mu$ M
10	800 $\mu$ M
12	65 $\mu$ M

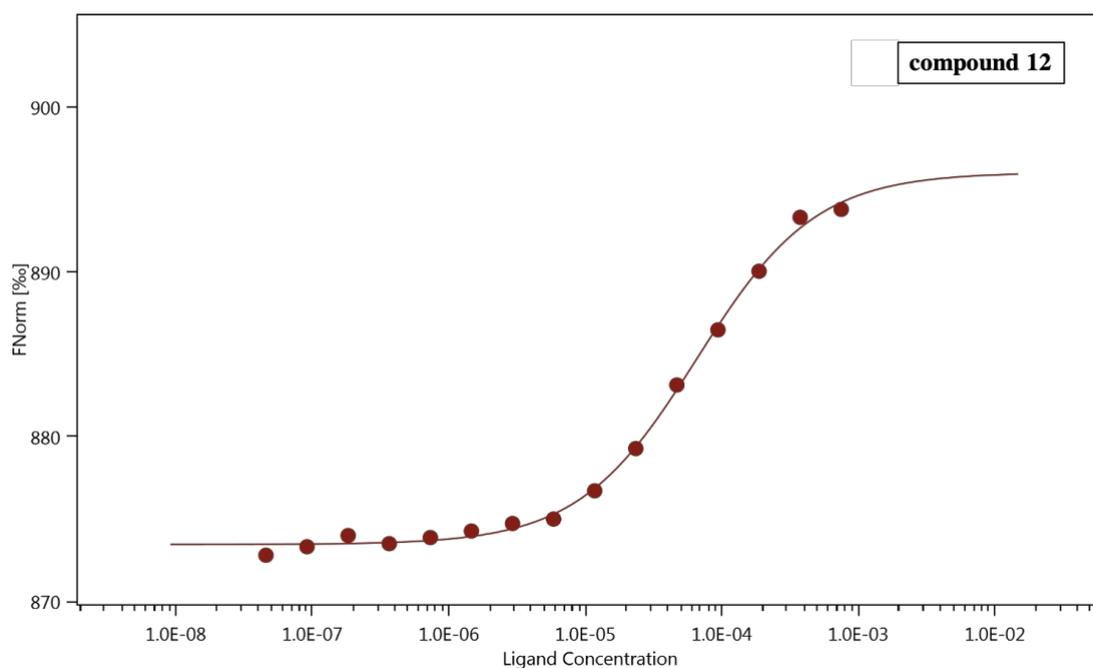


**Figure 3.33:** Structure of the four compounds with the best affinity for the hGCAP1 measured in MST experiments with their respective calculated  $K_d$  reported in the table. The binding curve of the hGCAP1 with compound 12 is reported below.

Finally, during the last period of my PhD work, I started to investigate the binding affinity of these compounds for the pathological mutants. 40 nM of D100G labelled on cysteine were added to serial dilution of compound 3 and MST measurements were performed in triplicate. As reported in figure 3.34, the binding affinity of the mutant and the *wt* protein for compound 3 are very similar, confirmed by a calculated  $K_d = (850 \pm 56) \mu\text{M}$  for D100G and  $K_d = (900 \pm 90) \mu\text{M}$  for the *wt*. This indicates that although this compound is able to recognise and bind to GCAP1, it is not selective for the mutant. Further binding affinity analyses of the compounds identified so far will be extended to the other available mutants in order to find out molecules with a higher selectivity for the COD related GCAP1 variants. Once these molecules are identified, their biological activity on GCAP1 will be investigated with enzymatic assays testing any possible effect on the regulation of the retGC1. Moreover, I will validate if the EF1 motif is the actual binding site of these molecules performing site-directed mutagenesis on residues predicted to be involved in the binding as shown in the *in silico* docking analysis.

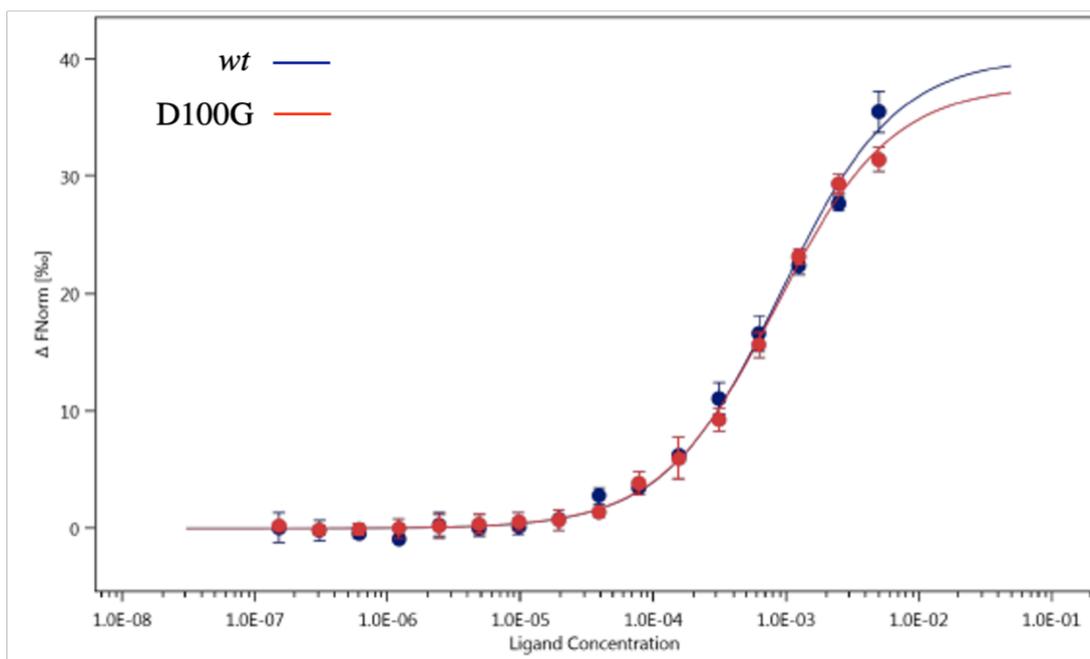


**Figure 3.34:** binding affinity of the hGCAP1 wt (blue curve) and D100G (red curve) for compound 3. MST measurements were performed in triplicate and ligand concentration (M) was fitted with the fluorescence variation ( $\Delta F_{\text{Norm}}^{0/100}$ ).

## 4. Conclusions and future perspectives

GCAP1 is a neuronal calcium sensor expressed in photoreceptors responsible for the modulation of the retGC1 activity during the phototransduction. Mutations in GCAP1 alter the affinity of the protein for  $\text{Ca}^{2+}$ . This condition leads to non-physiological  $\text{Ca}^{2+}$  concentrations required for the retGC1 inhibition, eventually causing the degeneration of photoreceptors and retinal dystrophies. To date, 22 pathological mutations responsible for COD/CORD have been associated with GCAP1 but a detailed mechanism of the interaction with retGC1 and the molecular determinants of the pathogenic GCAP1 variants are still incomplete.

During my PhD I used a multidisciplinary approach of biophysical and biochemical techniques in order to shed light on the human protein and to study the pathogenic effects of three mutations D100G, E155A and E155G.

I successfully produced and purified the *wt* hGCAP1 in a soluble form as recombinant protein in *E. coli* and observed with analytic SEC that the MW of the purified  $\text{Ca}^{2+}$ -bound hGCAP1 in solution is compatible with a dimeric assembly. By coupling MALS with SEC, I described for the first time that a monomer-dimer equilibrium characterizes GCAP1 in solution. Exhaustive experiments of analytic SEC and MST allowed to describe in detail this equilibrium which is different according to the divalent ion bound to the protein. After SEC experiments, exploiting the relation between the  $V_e$  of the protein and the logarithm of its MW (which depends on the monomer-dimer equilibrium that is related to protein concentration) we arrived to an equation depending on 3 free parameters in order to determine the monomer-dimer dissociation constant  $K_d$ . The  $K_d$  calculated for the  $\text{Mg}^{2+}$ -bound hGCAP1 is five times higher than the one calculated for the  $\text{Ca}^{2+}$ -bound form, showing that during phototransduction this equilibrium is shifted towards the dimer as the cytoplasmic concentration of  $\text{Ca}^{2+}$  increases after the light stimulus has occurred.

The analysis of monomer-dimer equilibrium represented an opportunity for me to master the Microscale Thermophoresis (MST) technique developed to study protein-protein and protein-ligand interactions. By decreasing the protein concentration, we were able to label the monomeric GCAP1 and we extended the use of this technique to study the interaction of the protein with itself during the homodimerization process. MST measurements confirmed the  $K_d$  calculated from analytic SEC experiments and assessed to the  $\text{Ca}^{2+}$ -bound GCAP1 a higher

propensity to form dimers with respect to the  $Mg^{2+}$ -bound state or for the apo protein (in the presence of EGTA/EDTA).

I discovered that by removing NaCl from the buffer it is possible to stabilize GCAP1 in the monomeric form. This condition allowed me to further study the effect of  $Ca^{2+}$  in the dimerization process. The divalent ion indeed plays a pivotal role in the process since at low salt concentration the addition of a small amount of  $Ca^{2+}$  (1 mM) is sufficient to push the monomeric state toward the monomer-dimer equilibrium, as observed in SEC-MALS experiments.

This effect could be due to the low isoelectric point of GCAP1 (4.4) which makes the protein negatively charged at physiological pH. Thus, at low salt concentration, electrostatic repulsion may be responsible for shifting the equilibrium towards the monomeric state, while the binding of three  $Ca^{2+}$  ions should partially shield the electrostatic repulsion and trigger protein dimerization.

To date, the only crystal structure available is that of the  $Ca^{2+}$ -bound chicken homologue, while the crystal structure of the hGCAP1 remains elusive. Despite all my efforts I did not obtain any diffracting crystals of the human protein. To overcome this issue, I exploited the high sequence identity between the chicken and human proteins with the aim to analyse the pathogenic mutations that affect the hGCAP1 on the cGCAP1 scaffold. Surprisingly, also the chicken protein, despite being monomeric in the crystal structure, displays a monomer-dimer equilibrium similar to what observed for hGCAP1. This common feature indicates that the monomer-dimer equilibrium is a property common to different GCAP1 orthologs, and therefore likely involved in the regulation mechanism of the cyclase.

Decreasing the dynamicity of the GCAP1 by removing the 12 C-terminal residues and inserting a disulfide bridge between the N-terminal and C-terminal portions proved to be a good strategy to obtain nice protein crystals. The crystallization conditions for the new construct will be optimized in order to increase the crystal size with hope to solve the crystal structure of the hGCAP1 and of the pathogenic mutants.

Using a combination of computational techniques and SAXS analysis, we exploited the constraints of the bovine GCAP1 dimeric model recently reported by Lim et al. [33], producing three different models of the hGCAP1 dimer. All our assemblies were in agreement with the experimental data obtained with SAXS and confirmed that the dimerization interface of the hGCAP1 is stabilized by hydrophobic interactions of the same residues identified in the bovine homologue (His19, Tyr22, Phe73 and Val77). These hydrophobic contacts have been proven

to be essential for both the dimerization of GCAP1 and the activation of retGC1 which needs itself to dimerize in order to be active. A possible explanation of the conserved monomer-dimer equilibrium of GCAP1 could be a required dimerization in order to bind to the cyclase in a 2:2 complex, whose allosteric regulation of catalytic activity may involve quaternary structural changes in the protein-protein complex [32].

The three variants D100G, E155A and E155G were produced and thoroughly characterized in collaboration with Prof. Dell'Orco's laboratory (University of Verona), confirming that  $\text{Ca}^{2+}$ -coordination is a fundamental feature required to the optimal switch of GCAP1 from retGC1-activator to inhibitor state, since individual amino acid substitutions can lead to a significantly altered functionality. Moreover, from the SAXS analysis of these pathogenic variants we assessed a common propensity to form oligomeric assemblies at increasing protein concentrations. While the MW of the E155G mutant is compatible with a monomer/dimer assembly, the D100G and E155A substitutions seem to produce dimer/tetramer and trimer/tetramer assemblies, respectively. This suggests that the local perturbation of the EF-hand motifs by pathogenic point mutations could ultimately lead to an altered organization of the GCAP1 quaternary structure which in turn could contribute to the pathological phenotype. It might be worth characterizing all those GCAP1 variants which carry a pathogenic mutation in a region unrelated to (or far from) the calcium-binding residues of the EF-motifs, such as P50L, L84F, G86R, E89K etc. Many of these pathogenic variants have already been partially characterized considering the effect of the mutation on the affinity for calcium; my future plan is to characterize these mutants evaluating their quaternary assembly in order to assess any possible correlation between the altered oligomeric state of GCAP1 and its altered regulatory activity on the retGC1.

Actually, no cure for retinal dystrophies is available. The main purpose of the Telethon project which allowed me to carry on my research is the design of therapeutic molecules able to restore the activity of the pathogenic GCAP1 variants. In order to get insights into the structural details of the activation/inhibition states of retGC1, the availability of a GCAP1/retGC1 complex is a crucial step. Since all attempts to express the single portions of the cyclase predicted to interact with GCAP1 resulted in insoluble proteins, I finally opted for producing the whole soluble cytoplasmic domain of retGC1. This allowed me to approach for the first time a new expression system (Baculovirus expression vector system) and to enhance my scientific and technical background, mastering how to properly handle insect cells in order to produce a recombinant baculovirus. Thanks to the collaboration with San Raffele's

laboratory (Milan) I will hopefully optimize the expression conditions of the retGC1 cytoplasmic domain and produce a retGC1/GCAP1 complex that will be investigated with a combined approach of X-ray crystallography and cryoEM.

Finally, from a preliminary *in silico* molecular docking targeted on the N-terminal EF-1 motif of the cGCAP1 crystal structure I selected a few molecules predicted to be able to bind to GCAP1. MST has been used to investigate the binding affinity for hGCAP1 and I identified four molecules with a  $K_d$  in the millimolar range. Particularly promising is the compound 12 and we are searching for homologous with higher affinity.

However, while searching for analogues to ameliorate the binding affinity of these compounds, it will be essential to test any possible modulatory effect on the activity of GCAP1 *wt* and pathological mutants with enzymatic assays in presence of the retGC1. At the same time, the validation of the real binding site of these compounds will be crucial in order to understand the molecular determinants of their potential effect on GCAP1.

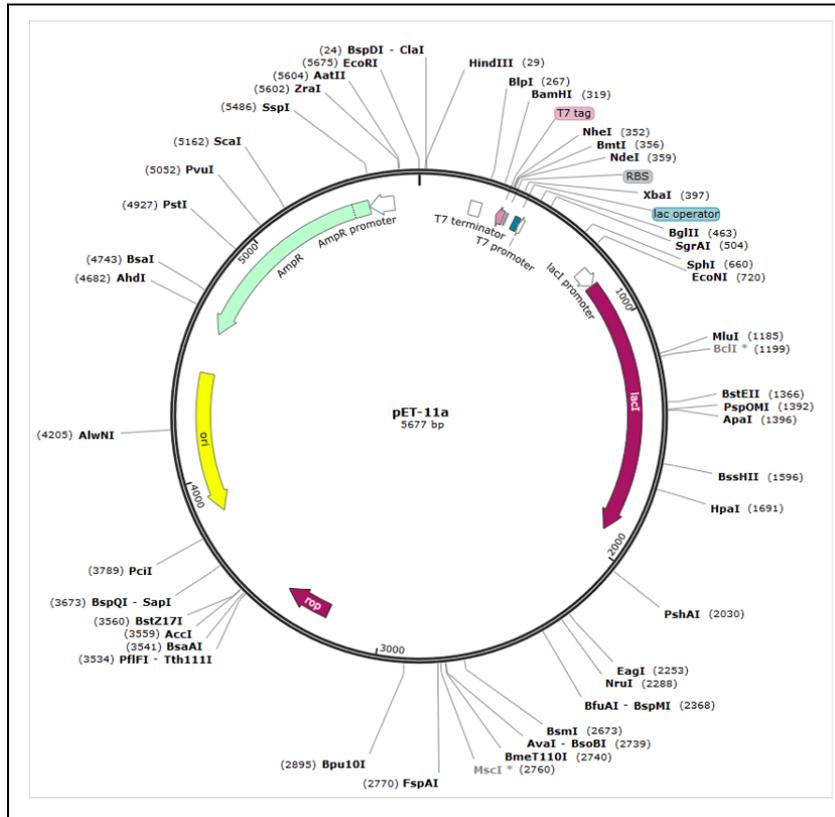
# 5. Materials and Methods

## 5.1 Plasmids for expression of myristoylated GCAP1 in *E.coli*:

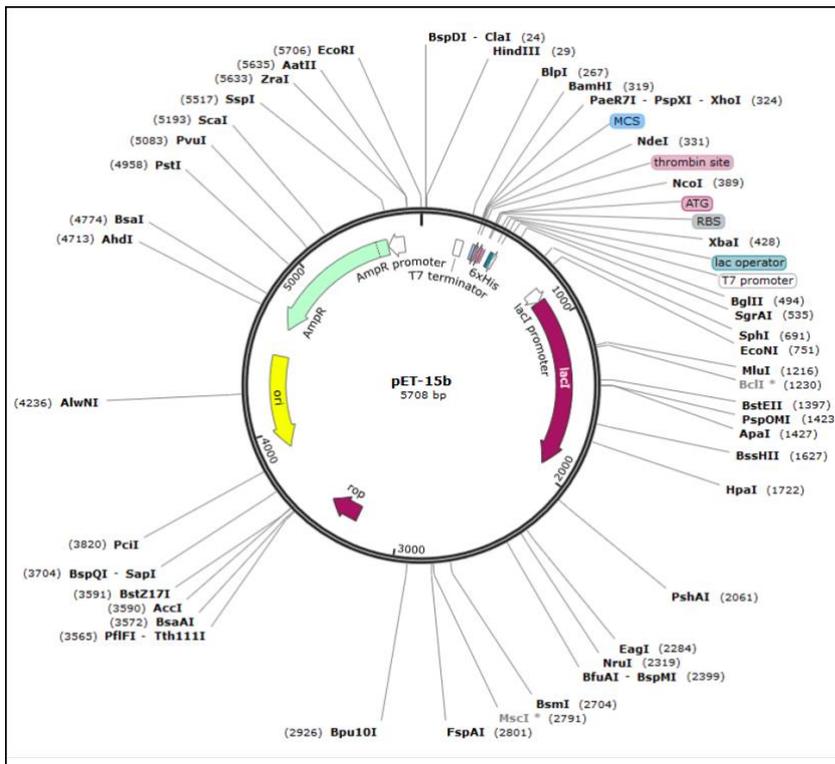
The plasmids used for the expression of the myristoylated human and chicken GCAP1 are here reported:

- human GCAP1 (hGCAP1) wt pET-11a, in which the sequence coding for GCAP1 was cloned between *NdeI* and *NheI*;
- chicken GCAP1 (cGCAP1) wt pET-15b, in which the sequence coding for the chicken isoform of GCAP1 was cloned between *Xho I* and *Nco I* restriction sites;
- N-myristoyltransferase (NMT)-1 pBB131, in which the sequence coding for the NMT1 from yeast was cloned between *NcoI* and *HindIII* [50].

GCAP1 recombinant plasmids were kindly provided by Prof. Daniele Dell'Orco (Università degli Studi di Verona), while NMT-1 pBB131 plasmid was kindly provided by Prof. Karl-Wilhelm Koch (Oldenburg University, DE).



A



B

Figure 5.1 Plasmids circular maps. pET-11a (A) and pET-15b (B) carry Ampicillin resistance gene.

## 5.2 Site directed mutagenesis (SDM)

The Q5 Site-Directed Mutagenesis Kit (New England BioLabs®) was used to introduce point mutations in the gene coding for hGCAP1 in order to produce:

- a shorter construct lacking the last twelve residues at the C-terminal predicted to be disordered (*wt*Δ12);
- two additional mutations introduced into the GCAP1 variant *wt*Δ12 coding gene carrying the Q58C and A118C substitutions. These mutations were introduced with the aim of promoting the formation of a disulfide bridge in order to reduce protein flexibility and facilitate its crystallization.

Customized primers for PCR were designed using NEBaseChanger tool (provided by New England BioLabs) and purchased by Eurofins Genomics

*wt*Δ12 primers:

*wt*Δ12\_F: 3'- tgaacaagatTAAGAaggtgcggatgaag-5'

*wt*Δ12\_R: 3'- ccattctgcaggcgacgg-5'

Q58C primers:

Q58C\_F: 3'-gtacgtggaatGCatgttcgaaacgttcgattcaacaaggac-5'

Q58C\_R: 3'-tgggacgcgctcggactc-5' 21

A118C primers:

A118C\_F: 3'-cattatccaaTGCattcgcgctatcaatccgtgtag-5'

A118C\_R: 3'-gtcagcagttcgtcgcga-5'

Primers for SDM are designed in such a way that the desired mutation is inserted at the center of the forward primer, including at least 10 complementary nucleotides on the 3' side of the mutation. The reverse primer is designed so that the 5' ends of the two primers anneal back-to-back.

### SDM reaction

- 12.5 µl Q5 Hot Start High-Fidelity 2X Master Mix;
- 1.25 µl Forward Primer 10 µM;
- 1.25 µl Reverse Primer 10 µM;
- Template DNA (1-25 ng/µl);

- Nuclease-free water 9  $\mu$ l.

The annealing temperature was calculated by NEBaseChanger (66°C for *wt* $\Delta$ 12, 69°C for Q58C and 64°C for A118C) and the PCR reaction was set according to the following protocol:

- Initial Denaturation at 98°C for 30 seconds;
- 25 Cycles: 98°C for 10 seconds, 50-72°C for 10-30 seconds, 72°C for 20-30 seconds/kb;
- Final Extension at 72°C for 2 minutes;

PCR product was then incubated for five minutes with KLD Enzyme Mix (NEB), containing kinase, ligase and Dpn1 enzymes. While the first two enzymes phosphorylate and ligate PCR products circularizing them, Dpn1 degrades the methylated DNA template.

KLD Enzyme Mix composition:

- 1  $\mu$ l PCR Product;
- 5  $\mu$ l 2X KLD Reaction Buffer;
- 1  $\mu$ l 10X KLD Enzyme Mix;
- 3  $\mu$ l Nuclease-free Water.

5  $\mu$ l of KLD mix were then used to transform TOP10 *E. coli* competent cells and the double substitution was checked by plasmid sequencing (Eurofins Genomics).

### Heat shock transformation

Recombinant plasmids were used to transform *E. coli* competent cells BL21-CodonPlus RP (containing Chloramphenicol resistance), BL21, SHuffle, TOP10 using the heat shock protocol reported below:

- One aliquot containing about 50  $\mu$ l of *E. coli* cells was thawed for about 30 minutes on ice;
- 2  $\mu$ l of plasmid (about 100-200 ng) were added to the competent cells and the transformation reaction was incubated on ice for at least 30 minutes, thereafter kept at 42°C for 30 seconds;
- after two minutes of incubation on ice, 500  $\mu$ l LB medium were added to the transformation reaction;
- transformed cells were incubated for one hour at 37°C with shaking at 250 rpm.

About 400 µl of transformed cells were plated on LB Agar Petri dishes containing proper antibiotics needed by specific plasmids/cells as dominant selective markers and incubated at 37°C overnight.

A single colony was used to prepare a starting growth in a volume of sterilized LB medium with the addition of the selection antibiotics (100 µg/ml of Ampicillin, 30 µg/ml of Kanamycin, 34 µg/ml of Chloramphenicol) and incubated at 37°C overnight.

Cells were collected by centrifugation for 10 minutes at 4400 rpm (5702 R Centrifuge, Eppendorf). Plasmid extraction was performed using the Monarch Plasmid Miniprep Kit (New England Biolabs) following the manufacturer's guide. Plasmid concentration was then measured at Nanodrop One/OneC (Thermofisher), based on absorbance at 260/280 nm.

### **5.3 GCAP1 expression and purification**

Typically, 50 ml of the initial growth were used to inoculate 2.5 l total growth medium (LB plus proper antibiotics combination) and incubated at 37°C with shaking at 220 rpm.

Once the cellular growth reached 0.4 OD<sub>600</sub>, 50 µg/ml myristic acid (Sigma-Aldrich) was added into the medium. GCAP1 expression was induced by the addition of 1 mM IPTG at 0.5-0.6 OD<sub>600</sub>.

After induction, cultures were incubated for 3 hours at 37°C, then centrifuged 15 minutes at 6000 rpm with a JLA 8100 rotor at 4°C (Avant J-20 Centrifuge, Beckman). Pellet was washed in Tris/HCl pH 7.5 buffer, and stored at -20°C.

#### **5.3.1 Cell lysis**

For the *E. coli* SHuffle mediated protein expression, the induction was carried on overnight at 20°C.

2 g of cells were resuspended in 80 ml of loading buffer (50 mM Tris/HCl pH 8, 50 mM NaCl, 2 mM EDTA, 5 mM DTT). A protease inhibitor cocktail (cOmplete, EDTA free, Roche), 20 mM MgSO<sub>4</sub> and lysozyme 0.25 mg/ml was added to the suspension. 10 µg/ml Deoxyribonuclease from bovine pancreas was added in order to eliminate nucleic acids.

*E. coli* cells were lysed by high pressure in a Basic Z Bench top (Constant Systems Limited, U.K.) at 25 KPSI. The crude extract was centrifuged for 30 minutes at 18,000 rpm and 4°C (Thermo Scientific Sorvall RC6 Plus Centrifuge, SS34 rotor). Collected supernatant was then

filtered through a 0.45  $\mu\text{m}$  diameter pored membrane (Millipore Express Pes Membrane, Millex-GP).

### **5.3.2 Ion Exchange Chromatography**

The clarified soluble extract was loaded in a HiPrep™ XL 16/10 (GE Healthcare Lifesciences) using a loading buffer composed of 50 mM Tris/HCl pH 8.0, 50 mM NaCl, 2 mM EDTA, 5 mM DTT. The elution was performed with a linear NaCl gradient (from 0.2 to 1 M in 60 minutes) in a 50 mM Tris/HCl pH 8.0, 2 mM EDTA, 5 mM DTT elution buffer with a 2 ml/min flow rate. Fractions containing GCAP1 were analyzed by SDS-PAGE, pooled and concentrated for the next purification step.

### **5.3.3 Size Exclusion Chromatography**

GCAP1 was loaded into a HiLoad™ 16/600 Superdex™75 pg (GE Healthcare Life Sciences) column, equilibrated with 20 mM Tris/HCl pH 8.0, 100 mM NaCl, 5 mM DTT, 1 mM  $\text{CaCl}_2$  and cOmplete protease inhibitor. SEC was performed using a 0.8 ml/min flow rate. Alternatively, the preparative SEC was performed in 2 mM EDTA and 2 mM EGTA in order to study protein behavior without calcium.

All the purification steps were performed using an ÄKTA pure 25L (GE Healthcare) at 10°C and checked with SDS-PAGE.

### **5.3.4 Analytic Size Exclusion Chromatography**

Analytic SEC was used to investigate the apparent MW of the fresh purified protein. MW standards for gel filtration chromatography were used to obtain a calibration curve of the column used for all the analytic SEC measurements in  $\text{Ca}^{2+}$ -buffer (fig. 5.2).

In order to study the monomer-dimer equilibrium of GCAP1, protein buffer was exchanged into 20 mM Tris/HCl pH 8.0, 100 mM NaCl, 1 mM DTT, with the addition of 5 mM  $\text{CaCl}_2$  or 5 mM  $\text{MgCl}_2$  / 2 mM EGTA (to study the  $\text{Mg}^{2+}$ -bound protein) using a PD-10 Desalting Column (GE Healthcare).

Different protein dilutions were prepared from 87  $\mu\text{M}$  to 2  $\mu\text{M}$  and 500  $\mu\text{l}$  samples were loaded into a Superdex™75 Increase 10/300 GL column (GE Healthcare Life Science) with a 0.8 ml/min flow rate.

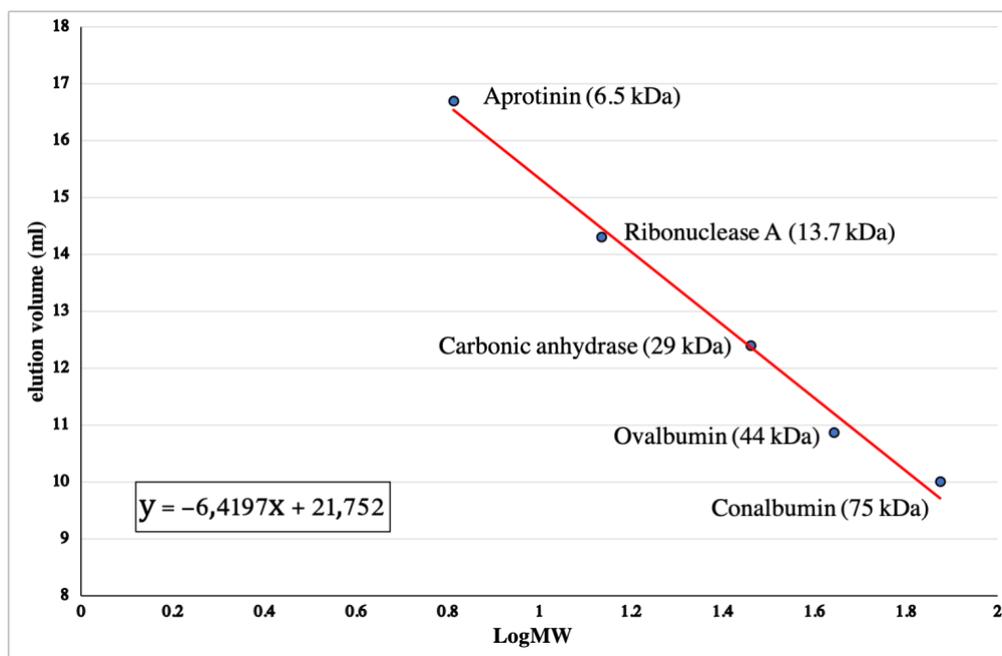


**Figure 5.2** Calibration curve of the Superdex<sup>TM</sup>75 Increase 10/300 GL column in Ca<sup>2+</sup>-buffer obtained by the combination of the elution volume (*y* axis) of MW standards with the logarithm of their MW (*x* axis).

## 5.4 SEC-MALS

MALS was coupled with SEC experiments (SEC-MALS) in order to separate different species of the GCAP1 monomer-dimer equilibrium, determining their MW and R<sub>g</sub> (radius of gyration) from light scattering data acquired.

The main advantage of this technique with respect to reference standards used in SEC column calibration is that MW can be determined independently from the elution volume (*V<sub>e</sub>*): this is of particular importance for non-globular proteins which don't interact with SEC columns in a way described by the calibration curve.

The molar mass of human and chicken GCAP1 monomer-dimer equilibrium were characterized with a Dawn® Heleos® Multi Angle Light Scattering (Wyatt, Santa Barbara, CA, USA) mounted on an analytical SEC-HPLC system. 200 µl of sample were separated by analytical SEC connected on-line with the Dawn® Heleos® Multi Angle Light Scattering, an Optilab® T-rEX Refractive Index Detector (Wyatt) and a Waters 2487 Dual k Absorbance Detector. Molar mass at different elution volumes were calculated by means of Astra software (v. 5.3.4.18, Wyatt) using 0.185 as dn/dc value.

## 5.5 Trypsin mediated limited proteolysis

Independent limited proteolysis experiments were carried out on GCAP1 in  $\text{Ca}^{2+}/\text{Mg}^{2+}$  or  $\text{Mg}^{2+}/\text{EGTA}$  buffers with trypsin to assess the presence of protein fragments resistant to the proteolytic cleavage.

Limited proteolysis experiments were performed with a 1/100 trypsin/GCAP1 molar ratio. The reaction was set with 0.4  $\mu\text{M}$  of trypsin and 40  $\mu\text{M}$  of GCAP1 in a 200  $\mu\text{l}$  volume using a 20 mM Tris/HCl pH 8.0, 100 mM NaCl, 1 mM DTT and 500  $\mu\text{M}$   $\text{CaCl}_2/\text{MgCl}_2$  or  $\text{MgCl}_2/\text{EGTA}$  buffer.

The reaction volume was increased up to 1 ml in order to produce stable fragments to be analyzed with chromatographic techniques.

The proteolysis reaction was incubated at 37°C and 9  $\mu\text{l}$  samples were collected at time zero ( $T_0$ ) and at regular times until 3 hours of incubation (10, 20, 30, 60, 90, 120, 150, 180 minutes and overnight). 3  $\mu\text{l}$  of Sample Buffer 4X were added and samples were boiled 5 minutes at 95°C before SDS PAGE.

Negative control consisted of 40  $\mu\text{M}$  GCAP1 incubated overnight without trypsin at 37°C.

## 5.6 Chemical cross-linking

Protein-protein interactions were stabilized by Bis Sulfo succinimidyl suberate (BS3), a water-soluble crosslinking agent acting by inducing nucleophilic attack of the amino group of lysine and subsequent covalent bonding via the crosslinker.

The crosslinking assay was performed with 25  $\mu\text{M}$  GCAP1 and 1 mM BS3 in a 200  $\mu\text{l}$  volume using a 20 mM HEPES pH 7.4, 100 mM NaCl, 1 mM  $\text{CaCl}_2$  buffer.

The reaction was incubated at room temperature and stopped after 2 hours with 2 mM Tris/HCl pH 7.5. 30  $\mu\text{l}$  aliquots were collected, added to 10  $\mu\text{l}$  of Sample Buffer 4x and boiled 5 minutes at 95°C before SDS PAGE.

Negative control consisted of 25  $\mu\text{M}$  GCAP1 incubated 2 hours without BS3.

## 5.7 Second Harmonic Generation (SHG)

Two-photon excitation is a multiphoton microscopy technique that provides three-dimensional optical sectioning of a sample above and below the plane of focus.

The SHG is a phenomenon that occurs with chiral crystals (represented by proteins in this specific case). If the biological sample is chiral, it will be able to produce a second harmonic wave characterized by half the wavelength of the excitation wave as represented (fig. 5.3).

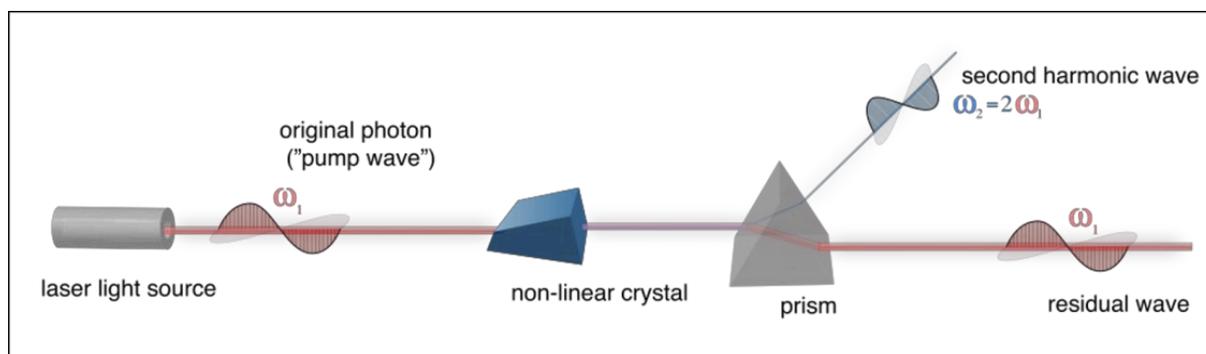


**Figure 5.3** Second Harmonic Generation schematic process.

1 mM of purified hGCAP1 was diluted 1:1 with the precipitant solution in a 0.5  $\mu$ l drop in a vapor diffusion hanging drop set up. After the precipitate was formed, the coverslip with the drop was placed and sealed on a new glass slide.

A two-photon microscope equipped with a 200-fs laser (Chameleon Discovery - Coherent) and a 25X water-immersion lens was used to investigate whether the hGCAP1 precipitate was crystalline.

In order to verify any SHG signal from the sample, different wavelengths available from the tunable laser were tested and finally the experiment was set up using a 1064 nm excitation wavelength and setting the detector at 532 nm.

## 5.8 Crystallization trials

### Vapor diffusion

Crystallization trials were performed at 20°C using a crystallization robot Oryx-8 (Douglas Instruments). Protein solution (20 mg/ml) was joint to reservoir solution in a 0.4  $\mu$ l drop varying protein concentration (30%, 50%, 70%) and 100  $\mu$ l of crystallization solution were added into the well.

Many different commercial precipitant solutions (crystal screen solutions) were tried to search for crystallization conditions:

- HTTM, Hampton Research
- JCSG – plus™, Molecular Dimensions
- JBS, Jena Bioscience
- Morpheus
- Stura /macrosol
- PACT
- PegIon
- SaltRX
- Ammonium sulfate optimization screening: from 0.5 to 2.2 M of ammonium sulfate; from pH 6 to pH 9 ( $\Delta\text{pH} = 0.2$ ) and 0.1 M NaCl
- PEG 20,000 optimization screening: from 20% to 28% M PEG; from pH 6 to pH 9 ( $\Delta\text{pH} = 0.2$ ) and from 0.1 to 0.5 M  $\text{KNO}_3$ .

Vapor diffusion crystallization experiments were performed using the sitting-drop technique, while I extended the optimization of the most promising conditions to hanging-drop.

### Microbatch

For most of the crystal screens tested I coupled vapor-diffusion to microbatch in order to explore a more extended region of the “phase diagram”. Typically, drops of 0.4  $\mu\text{l}$  composed of 65% protein and 35% precipitant were placed in a 96-well plate and covered with 75% silicon oil and 25% paraffin oil.

Crystallization trials were often performed in duplicate in order to test different crystallization temperatures (20°C and/or 4°C).

## **5.9 Recombinant baculovirus production for the expression of the cytoplasmic domain of retinal guanylate cyclase**

In order to study the interaction between GCAP1 and its target protein retGC1, the baculovirus expression vector system (BEVS) was adopted to express the cytoplasmic domain of the human retinal guanylate cyclase (retGC) (from H485 to S1103).

Because of retGCs high MW and the presence of disulfide bridges, an eukaryotic cell expression system was adopted by infecting *Spodoptera frugiperda* (*Sf9*) cells with modified baculovirus expression vectors.

BEVS exploits the baculovirus mediated infection for large scale protein production in eukaryotic insect cells. *Autographa californica* multi-nucleopolyhedrovirus (AcMNPV) is a virus that upon genetic engineering facilitates foreign genes insertion; *Sf9* cells were employed to produce the recombinant baculovirus. The sequence coding for the cytoplasmic domain of retGC1 was cloned into a pIEx/Bac-3 plasmid, kindly provided by Prof. Karl Koch. Since no tag was associated with the cloned sequence, an insertion of 6xHis-tag was performed with the same Q5 Site-Directed Mutagenesis Kit used for the SDM experiments.

N-term His tag and thrombin tag was taken from pET-28a plasmid and inserted into pIEx/Bac-3 plasmid.

Designed primers:

Q5SDM\_F: 3'-AGCAGCGGCCTGGTGCCGCGCGGCAGCcattatgtgaggcaccgg-5'

Q5SDM\_R: 3'-GTGATGATGATTGATGATGATGGCTGCTGCCcatatgattgtaaataaaatgtaatttacag-5'

The pIEX/Bac plasmids are a group of vectors intended to be used in association with the commercial viral BacMagic DNA in order to obtain the *bacmide* required for the production of a functional baculovirus. For the expression of retGC1 the BacMagic™-2 DNA Kit was purchased by Novagen. The BacMagic DNA viral genome carries a deletion of the essential open reading frame (ORF) 1629, preventing non-recombinant baculovirus from replicating in insect cells. BacMagic DNA also contains deletions of non-essential genes, such as *chiA* (coding for the secretory protein chitinase) and *v-cath* (coding for a cathepsin-like cysteine protease), resulting in significantly improved quality and expression yield for most of the target proteins.

The *bacmide* is produced within insect cells thanks to the co-transfection with the pIEX/Bac vector and the BacMagic viral DNA: upon homologous recombination the ORF 1629 is restored and the target sequence replaces bacterial artificial chromosome (BAC), producing the recombinant functional *bacmide* (fig. 5.4).

The use of pIEx Bac-3, as a result of the combination of immediate/early (*hr5* enhancer and *iel* promoter) and late/very late (*p10*) promoters, enables the continuous expression of the target protein.

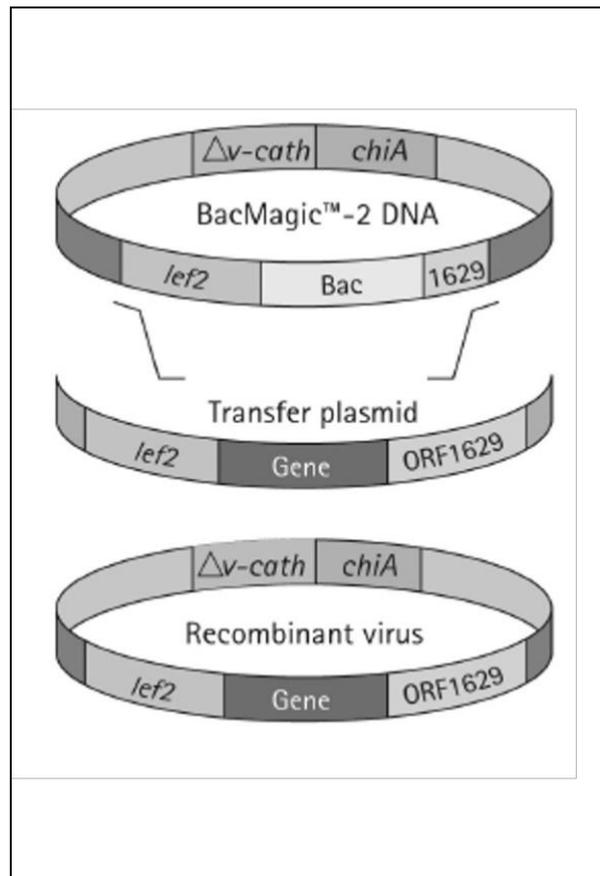


**Figure 5.4** *Bacmide* production with ORF 1629 restoration

$1 \times 10^8$  *Sf9* cells were thawed according to BacMagic™-2 DNA Kit protocol and resuspended in Sf-900™ II SFM (Gibco™) serum-free insect cell culture medium under laminar flow hood. Cell cultures were diluted to  $0.5 \times 10^6$ /ml (50 ml volume) and incubated at 28°C and 150 rpm in 250 ml disposable polycarbonate Erlenmeyer flask.

The production of the recombinant baculovirus occurred by co-transfection of *Sf9* cells with the pLEX/Bac-3 carrying the retGC1 sequence and the BacMagic-2 viral DNA in a 35-mm plate using the Insect GeneJuice® Transfection Reagent, optimized for maximal transfection efficiency of *Sf9* cells.

According to the manufacturer protocol, one hour before co-transfection, 35-mm plate dishes were seeded with  $1 \times 10^6$  cells/ml in 2 ml of cell medium, forming an even cell monolayer and incubated for one hour at 28°C

The co-transfection reaction was prepared as following:

- 1 ml BacVector Insect Cell Medium
- 5 µl Insect GeneJuice
- 5 µl BacMagic DNA (100 ng total)
- 5 µl transfer vector DNA (500 ng total)

Negative control consisted in a corresponding amount of cell medium in place of the viral BacMagic DNA.

The transfection mix was incubated for 30 minutes at room temperature, allowing liposome complexes formation.

After incubation, the growth medium was gently removed by the cell monolayer and 1 ml of transfection mix was added dropwise to the center of each dish; transfection reaction was incubated at 28°C for at least 5 hours.

After this incubation period, 1 ml of insect cell medium was added and the incubation was carried on for 5 days.

After 5 days, virus-infected cells appeared grainy with enlarged nuclei and didn't form a confluent monolayer. Cellular medium containing recombinant baculovirus was harvested by centrifugation at 1000 x g for 10 minutes.

Amplification of the first (P0) generation of recombinant baculovirus in *Sf9* cells grown in suspension culture was necessary to increase the viral title.

Different P0 virus dilutions (1:100, 1:500, 1:5000) were inoculated into 50 ml *Sf9* cells flasks and incubated with shaking. Cellular growth was monitored day by day until a remarkable stop was registered (4-5 days) suggesting a proper infection rate.

At this point the virus contained into cell medium culture was harvested by centrifugation at 1000 x g for 10 minutes.

Surnatant containing the recombinant baculovirus was aseptically removed and stored as P1 virus stock in dark at 4°C.

# References

- [1] M. Brini, T. Calì, D. Ottolini, and E. Carafoli, “Neuronal calcium signaling: Function and dysfunction,” *Cellular and Molecular Life Sciences*. 2014.
- [2] G. J. Augustine, F. Santamaria, and K. Tanaka, “Local calcium signaling in neurons,” *Neuron*. 2003.
- [3] Y. Bourne, J. Dannenberg, V. Pollmann, P. Marchot, and O. Pongs, “Immunocytochemical Localization and Crystal Structure of Human Frequentin (Neuronal Calcium Sensor 1),” *J. Biol. Chem.*, 2001.
- [4] J. B. Ames, K. B. Hendricks, T. Strahl, I. G. Huttner, N. Hamasaki, and J. Thorner, “Structure and calcium-binding properties of Frq1, a novel calcium sensor in the yeast *Saccharomyces cerevisiae*,” *Biochemistry*, 2000.
- [5] J. B. Ames, A. M. Dizhoor, M. Ikura, K. Palczewski, and L. Stryer, “Three-dimensional structure of guanylyl cyclase activating protein-2, a calcium-sensitive modulator of photoreceptor guanylyl cyclases,” *J. Biol. Chem.*, 1999.
- [6] S. Vijay-Kumar and V. D. Kumar, “Crystal structure of recombinant bovine neurocalcin,” *Nat. Struct. Biol.*, 1999.
- [7] R. H. Scannevin *et al.*, “Two N-Terminal Domains of Kv4 K<sup>+</sup> Channels Regulate Binding to and Modulation by KChIP1,” *Neuron*, 2004.
- [8] J. B. Ames, R. Ishima, T. Tanaka, J. I. Gordon, L. Stryer, and M. Ikura, “Molecular mechanics of calcium-myristoyl switches,” *Nature*, 1997.
- [9] X. Robert and P. Gouet, “Deciphering key features in protein structures with the new ENDscript server,” *Nucleic Acids Res.*, 2014.
- [10] A. M. Dizhoor, C. K. Chen, E. Olshevskaya, V. V. Sinelnikova, P. Phillipov, and J. B. Hurley, “Role of the acylated amino terminus of recoverin in Ca<sup>2+</sup>- dependent membrane interaction,” *Science (80-. )*, 1993.
- [11] S. Lim, I. Peshenko, A. Dizhoor, and J. B. Ames, “Effects of Ca<sup>2+</sup>, Mg<sup>2+</sup>, and myristoylation on guanylyl cyclase activating protein 1 structure and stability,” *Biochemistry*, 2009.
- [12] R. Stephen, G. Bereta, M. Golczak, K. Palczewski, and M. C. Sousa, “Stabilizing Function for Myristoyl Group Revealed by the Crystal Structure of a Neuronal Calcium Sensor, Guanylate Cyclase-Activating Protein 1,” *Structure*, 2007.
- [13] S. Lim, I. V. Peshenko, A. M. Dizhoor, and J. B. Ames, “Structural insights for activation of retinal guanylate cyclase by GCAP1,” *PLoS One*, 2013.
- [14] M. Ikura, “Calcium binding and conformational response in EF-hand proteins,” *Trends in Biochemical Sciences*. 1996.
- [15] J. L. Gifford, M. P. Walsh, and H. J. Vogel, “Structures and metal-ion-binding properties of the Ca<sup>2+</sup>-binding helix-loop-helix EF-hand motifs.,” *Biochem. J.*, vol. 405, no. 2, pp. 199–221, Jul. 2007.
- [16] S. Bhattacharya, C. G. Bunick, and W. J. Chazin, “Target selectivity in EF-hand calcium binding proteins,” *Biochim. Biophys. Acta - Mol. Cell Res.*, vol. 1742, no. 1–3, pp. 69–79, 2004.
- [17] A. P. Yamniuk, L. T. Nguyen, T. T. Hoang, and H. J. Vogel, “Metal Ion Binding Properties and Conformational States of Calcium- and Integrin-Binding Protein,” *Biochemistry*, 2004.
- [18] E. A. Permyakov and R. H. Kretsinger, *Calcium Binding Proteins*. 2010.
- [19] R. W. Rodieck, “The First Steps in Seeing,” 1998.
- [20] S. Lim, A. M. Dizhoor, and J. B. Ames, “Structural diversity of neuronal calcium sensor

- proteins and insights for activation of retinal guanylyl cyclase by GCAP1,” *Frontiers in Molecular Neuroscience*. 2014.
- [21] E. N. Pugh and T. D. Lamb, “Chapter 5 Phototransduction in vertebrate rods and cones: Molecular mechanisms of amplification, recovery and light adaptation,” *Handb. Biol. Phys.*, 2000.
- [22] J. Chen and A. P. Sampath, “Chapter 14 - Structure and Function of Rod and Cone Photoreceptors,” S. J. Ryan, S. R. Sadda, D. R. Hinton, A. P. Schachar, S. R. Sadda, C. P. Wilkinson, P. Wiedemann, and A. P. B. T.-R. (Fifth E. Schachar, Eds. London: W.B. Saunders, 2013, pp. 342–359.
- [23] R. K. Sharma and T. Duda, “Ca<sup>2+</sup>-sensors and ROS-GC: Interlocked sensory transduction elements: A review,” *Frontiers in Molecular Neuroscience*. 2012.
- [24] A. M. Dizhoor, E. V Olshevskaya, and I. V Peshenko, “Mg<sup>2+</sup>/Ca<sup>2+</sup> cation binding cycle of guanylyl cyclase activating proteins (GCAPs): role in regulation of photoreceptor guanylyl cyclase,” *Mol. Cell. Biochem.*, vol. 334, no. 1–2, pp. 117–124, Jan. 2010.
- [25] S. L. Semple-Rowland, P. Larkin, J. D. Bronson, K. Nykamp, W. J. Streit, and W. Baehr, “Characterization of the chicken GCAP gene array and analyses of GCAP1, GCAP2, and GC1 gene expression in normal and rd chicken pineal,” *Mol. Vis.*, 1999.
- [26] A. Mendez *et al.*, “Role of guanylate cyclase-activating proteins (GCAPs) in setting the flash sensitivity of rod photoreceptors,” *Proc. Natl. Acad. Sci. U. S. A.*, 2001.
- [27] J. B. Ames and S. Lim, “Molecular structure and target recognition of neuronal calcium sensor proteins,” *Biochimica et Biophysica Acta - General Subjects*. 2012.
- [28] I. V. Peshenko, E. V. Olshevskaya, S. Lim, J. B. Ames, and A. M. Dizhoor, “Calcium-myristoyl tug is a new mechanism for intramolecular tuning of calcium sensitivity and target enzyme interaction for guanylyl cyclase-activating protein 1: Dynamic connection between n-fatty acyl group and EF-hand controls calcium sensitivity,” *J. Biol. Chem.*, 2012.
- [29] F. Vinberg, I. V. Peshenko, J. Chen, A. M. Dizhoor, and V. J. Kefalov, “Guanylate cyclase-activating protein 2 contributes to phototransduction and light adaptation in mouse cone photoreceptors,” *J. Biol. Chem.*, 2018.
- [30] K. W. Koch and D. Dell’Orco, “A calcium-relay mechanism in vertebrate phototransduction,” *ACS Chemical Neuroscience*. 2013.
- [31] E. V. Olshevskaya, A. N. Ermilov, and A. M. Dizhoor, “Dimerization of guanylyl cyclase-activating protein and a mechanism of photoreceptor guanylyl cyclase activation,” *J. Biol. Chem.*, 1999.
- [32] J. B. Ames, “Dimerization of neuronal calcium sensor proteins,” *Frontiers in Molecular Neuroscience*. 2018.
- [33] J. Y. Hwang and K. W. Koch, “Calcium- and myristoyl-dependent properties of guanylate cyclase-activating protein-1 and protein-2,” *Biochemistry*, 2002.
- [34] M. Michaelides, D. M. Hunt, and A. T. Moore, “The cone dysfunction syndromes,” *British Journal of Ophthalmology*. 2004.
- [35] J. S. Gill, M. Georgiou, A. Kalitzeos, A. T. Moore, and M. Michaelides, “Progressive cone and cone-rod dystrophies: Clinical features, molecular genetics and prospects for therapy,” *Br. J. Ophthalmol.*, 2019.
- [36] D. Chakraborty, S. M. Conley, S. J. Fliesler, and M. I. Naash, “The function of oligomerization-incompetent RDS in rods,” *Adv. Exp. Med. Biol.*, vol. 664, pp. 39–46, 2010.
- [37] M. Power, S. Das, K. Schütze, V. Marigo, P. Ekström, and F. Paquet-Durand, “Cellular mechanisms of hereditary photoreceptor degeneration – Focus on cGMP,” *Progress in Retinal and Eye Research*. 2020.
- [38] S. E. Wilkie *et al.*, “Identification and functional consequences of a new mutation

- (E155G) in the gene for GCAP1 that causes autosomal dominant cone dystrophy,” *Am. J. Hum. Genet.*, 2001.
- [39] V. Marino, A. Scholten, K. W. Koch, and D. Dell’Orco, “Two retinal dystrophy-associated missense mutations in GUCA1A with distinct molecular properties result in a similar aberrant regulation of the retinal guanylate cyclase,” *Hum. Mol. Genet.*, 2015.
- [40] F. Vocke *et al.*, “Dysfunction of cGMP signalling in photoreceptors by a macular dystrophy-related mutation in the calcium sensor GCAP1,” *Hum. Mol. Genet.*, 2017.
- [41] I. V. Peshenko, E. V. Olshevskaya, S. Lim, J. B. Ames, and A. M. Dizhoor, “Identification of target binding site in photoreceptor guanylyl cyclase-activating protein 1 (GCAP1),” *J. Biol. Chem.*, 2014.
- [42] D. Dell’Orco, P. Behnen, S. Linse, and K.-W. Koch, “Calcium binding, structural stability and guanylate cyclase activation in GCAP1 variants associated with human cone dystrophy,” *Cell. Mol. Life Sci.*, vol. 67, no. 6, pp. 973–984, Mar. 2010.
- [43] G. Manes *et al.*, “Cone dystrophy or macular dystrophy associated with novel autosomal dominant GUCA1A mutations,” *Mol. Vis.*, 2017.
- [44] I. V. Peshenko *et al.*, “A G86R mutation in the calcium-sensor protein GCAP1 alters regulation of retinal guanylyl cyclase and causes dominant cone-rod degeneration,” *J. Biol. Chem.*, 2019.
- [45] K. Mizobuchi *et al.*, “Characterization of GUCA1A-associated dominant cone/cone-rod dystrophy: low prevalence among Japanese patients with inherited retinal dystrophies,” *Sci. Rep.*, vol. 9, no. 1, p. 16851, Nov. 2019.
- [46] V. Marino *et al.*, “A novel p.(Glu111Val) missense mutation in GUCA1A associated with cone-rod dystrophy leads to impaired calcium sensing and perturbed second messenger homeostasis in photoreceptors,” *Hum. Mol. Genet.*, 2018.
- [47] B. G. Pierce, K. Wiehe, H. Hwang, B. H. Kim, T. Vreven, and Z. Weng, “ZDOCK server: Interactive docking prediction of protein-protein complexes and symmetric multimers,” *Bioinformatics*, 2014.
- [48] C. Lange, T. Duda, M. Beyermann, R. K. Sharma, and K. W. Koch, “Regions in vertebrate photoreceptor guanylyl cyclase ROS-GC1 involved in Ca(2+)-dependent regulation by guanylyl cyclase-activating protein GCAP-1,” *FEBS Lett.*, vol. 460, no. 1, pp. 27–31, Oct. 1999.
- [49] O. Trott and A. J. Olson, “AutoDock Vina: Improving the speed and accuracy of docking with a new scoring function, efficient optimization, and multithreading,” *J. Comput. Chem.*, 2009.
- [50] R. J. Duronio *et al.*, “Protein N-myristoylation in Escherichia coli: reconstitution of a eukaryotic protein modification in bacteria,” *Proc. Natl. Acad. Sci.*, vol. 87, no. 4, pp. 1506–1510, 1990.

# Introduction to paper 1

## **Modulation of Guanylate cyclase activating protein 1 (GCAP1) dimeric assembly by $\text{Ca}^{2+}$ or $\text{Mg}^{2+}$ : hints to understand protein activity**

In this work we describe the monomer-dimer equilibrium which characterizes the recombinant wild type hGCAP1. We analyse its propensity to form dimers in solution in different conditions, i.e. in complex with  $\text{Ca}^{2+}$  or  $\text{Mg}^{2+}$  and at different protein and salt concentrations. A combined approach of Small Angle X-ray Scattering, protein-protein docking and molecular dynamics has been used to produce three different dimeric models of the human protein which provide novel insights into the knowledge of its structure.

I developed and optimized the expression and purification protocols for the production of the recombinant hGCAP1 and cGCAP1 in a soluble form. I personally performed all the analytic SEC and MicroScale Thermophoresis experiments reported in the article and in my PhD thesis with the help of Carlo Bidoia who I supervised during his master thesis work. I performed all the dynamic light scattering and the Trp fluorescence measurements and discovered the effects of salt concentration in the dimerization process by combining SEC and MALS under the supervision of Dr. Alberto Barbiroli.

I was responsible for the preparation of all samples used for SAXS measurements and I participated to all the data collections performed at the European Synchrotron Radiation Facility and to the analysis of the data collected.

# Introduction to paper 2

## **Missense mutations affecting Ca<sup>2+</sup>-coordination in GCAP1 lead to cone-rod dystrophies by altering protein structural and functional properties**

The subject of this work is the investigation of the structural and functional effects of three missense mutations in GCAP1 associated with cone-rod dystrophy.

D100G, E155A and E155G mutations affect residues directly involved in Ca<sup>2+</sup>-coordination. These pathogenic variants were thoroughly characterized with biochemical and biophysical techniques that pointed out a decreased affinity for Ca<sup>2+</sup> resulting in a constitutively activation of the retinal guanylate cyclase. Moreover, Small Angle X-ray Scattering was used to assess the oligomerization state of the GCAP1 variants and we report that point mutations of crucial residues in EF3 (D100) and EF4 (E155) are responsible for a severe perturbation of the quaternary structure of GCAP1.

All the three pathogenic variants were produced in parallel by Prof. Dell'Orco group (Verona) and by me at the Institute of Biophysics (Milano). I performed preliminary analytic SEC experiments which assessed an oligomeric state of the purified proteins. All the reported biophysical and biochemical characterization was performed by Prof. Dell'Orco group.

I personally performed the data collection at Diamond Light Source (Oxford) where serial dilutions of the human protein were analysed in SAXS experiments comparing the D100G, E155G and E155A pathological variants. These data were used to point out the monomer-dimer equilibrium which characterize also the mutants but with unequal tendency to form higher order quaternary assemblies. In particular, the tendency to form oligomers at high protein concentration is more pronounced for E155A and to a minor extent for D100G and E155G.

Article

# Modulation of Guanylate Cyclase Activating Protein 1 (GCAP1) Dimeric Assembly by $\text{Ca}^{2+}$ or $\text{Mg}^{2+}$ : Hints to Understand Protein Activity

Francesco Boni<sup>1,2</sup>, Valerio Marino<sup>3</sup>, Carlo Bidoia<sup>1,2</sup>, Eloise Mastrangelo<sup>1,2</sup>, Alberto Barbiroli<sup>4</sup>, Daniele Dell'Orco<sup>3,\*</sup> and Mario Milani<sup>1,2,\*</sup>

<sup>1</sup> CNR-IBF, Istituto di Biofisica, Via Celoria 26, I-20133 Milan, Italy; francesco.boni@unimi.it (F.B.);

carlo.bidoia@studenti.unimi.it (C.B.); eloise.mastrangelo@unimi.it (E.M.)

<sup>2</sup> Dipartimento di Bioscienze, Università di Milano, Via Celoria 26, I-20133 Milan, Italy

<sup>3</sup> Dipartimento di Neuroscienze, Biomedicina e Movimento, Sezione di Chimica Biologica, Università di Verona, I-37134 Verona, Italy; valerio.marino@univr.it

<sup>4</sup> Dipartimento di Scienze per gli Alimenti, la Nutrizione e l'Ambiente, Università degli Studi di Milano, Via Celoria 2, I-20133 Milan, Italy; alberto.barbiroli@unimi.it

\* Correspondence: daniele.dellorco@univr.it (D.D.); mario.milani@unimi.it (M.M.);

Tel.: +39-045-802-7637 (D.D.); +39-02-5031-4890 (M.M.)

Received: 17 September 2020; Accepted: 1 October 2020; Published: 5 October 2020



**Abstract:** The guanylyl cyclase-activating protein 1, GCAP1, activates or inhibits retinal guanylyl cyclase (retGC) depending on cellular  $\text{Ca}^{2+}$  concentrations. Several point mutations of GCAP1 have been associated with impaired calcium sensitivity that eventually triggers progressive retinal degeneration. In this work, we demonstrate that the recombinant human protein presents a highly dynamic monomer-dimer equilibrium, whose dissociation constant is influenced by salt concentration and, more importantly, by protein binding to  $\text{Ca}^{2+}$  or  $\text{Mg}^{2+}$ . Based on small-angle X-ray scattering data, protein-protein docking, and molecular dynamics simulations we propose two novel three-dimensional models of  $\text{Ca}^{2+}$ -bound GCAP1 dimer. The different propensity of human GCAP1 to dimerize suggests structural differences induced by cation binding potentially involved in the regulation of retGC activity.

**Keywords:** quaternary assembly; calcium-binding proteins; EF-hand; protein-protein interaction; small-angle X-ray scattering; molecular dynamics simulations; protein modeling; protein dynamics; size exclusion chromatography; multi-angle light scattering

## 1. Introduction

In photoreceptor cells, light photons are transformed into electric signals by the coordinate interplay of a complex network of proteins, regulated by different chemical messengers [1].

Guanylyl cyclase-activating protein 1 (GCAP1) belongs to the calmodulin superfamily and hosts 4 EF-hand motifs (EF1–EF4). At low  $\text{Ca}^{2+}$  concentration (<100 nM) GCAP1 EF2 can bind at least one  $\text{Mg}^{2+}$  ion [2] activating retinal guanylyl cyclase 1 (retGC1) [3,4]. Active retGC1, in turn, replenishes the second messenger cGMP, switching off the light-activated cascade and restoring the photoreceptors' dark state. High cGMP concentration increases the influx of  $\text{Ca}^{2+}$  through the cyclic nucleotide-gated (CNG) channels determining GCAP1  $\text{Ca}^{2+}$ -bound state (EF2-4 bind 3  $\text{Ca}^{2+}$  ions) that inhibits retGC1 activity. During evolution, GCAP1 N-terminal EF-hand (EF1) lost the capability to bind calcium and became involved in the binding of retGC1 and modulation of its activity [5–7].

So far, 22 pathological point mutations of GCAP1 have been identified, which are associated with an autosomal dominant cone or cone-rod dystrophy [8]. Such mutations usually induce a lower affinity

for  $\text{Ca}^{2+}$  determining the deregulation of retGC1 at physiological calcium levels, with progressive degeneration of the cone photoreceptors [9,10]. Nevertheless, exceptions exist for substitutions at the N-terminal domain (L84F and L176) that do not perturb the affinity for  $\text{Ca}^{2+}$  in the respective GCAP1 variants [11,12]. Recent work suggests also the involvement of GCAP1 in retinitis pigmentosa, a severe form of progressive rod-cone dystrophy [13].

It is known that purified GCAP1 displays both monomeric and dimeric species [14]. Recently the dimeric assembly raised particular interest for its possible involvement in retGC1 regulation [15,16]. The dimeric assembly proposed by Lim et al. [15] involves contacts between residues comprised in EF1 and EF2 motifs, i.e., in the portion of the protein that is thought to interact with retGC1, specifically His19, Tyr22, Phe73, and Val77. Mutations of these residues abolished the dimeric assembly as proven by analytical gel filtration [15].

In this work, we performed several experiments on recombinant human (h) GCAP1, to thoroughly analyze the dimeric assembly. Microscale thermophoresis, size exclusion chromatography (SEC) and small-angle X-ray scattering (SAXS) data confirmed the presence of a monomer-dimer equilibrium in solution influenced by  $\text{Ca}^{2+}$  or  $\text{Mg}^{2+}$  binding and by ionic strength.

Using the ZDOCK program [17] for rigid-body protein–protein docking, we produced a large number of possible dimeric assemblies, ranked using the empirical docking score, and filtered according to the fulfillment of distance constraints imposed by previous EPR double electron-electron resonance (DEER) experiments [15]. The best 3 dimers were selected for further characterization and optimization by molecular dynamics (MD) simulations and analyzed with SEC-SAXS data collected at the highest protein concentration. The optimized dimeric structures were used to predict the change in the free energy of binding ( $\Delta\Delta G^\circ$ ) upon mutations, which are known to induce GCAP1 monomerization [15]. The two resulting three-dimensional models of dimeric GCAP1 in its  $\text{Ca}^{2+}$ -bound form presented in this work, recapitulate all current experimental lines of evidence from us and other authors and might have implications on the regulatory activity of GCAP1.

## 2. Materials and Methods

### 2.1. Human GCAP1 Expression and Purification

To produce the N-terminal myristoylated hGCAP1, the recombinant plasmid pET11a carrying the cDNA sequence was co-transformed in the *E. coli* strain BL21-CodonPlus RP (Agilent Technologies, Santa Clara, CA, USA) together with a pBB131 plasmid carrying the coding sequence for yeast N-myristoyltransferase (NMT). The hGCAP1 construct has the E6S mutation needed for the post-translational myristoylation.

Cell cultures were grown at 37 °C in 2 L of LB medium containing 100 µg/mL ampicillin (Amp), 30 µg/mL kanamycin (Kan), and 34 µg/mL chloramphenicol (Cm). The myristic acid (220 µM) was added when the culture reached the OD<sub>600</sub> = 0.4. Fifteen min later, the expression of hGCAP1 and NMT was induced by the addition of 1 mM IPTG. Cells were harvested after 3 h at 37 °C and frozen at −20 °C.

Typically, 3 g of *E. coli* cells were resuspended in lysis buffer (50 mM Tris-HCl pH 8.0, 50 mM NaCl, 10 µg/mL Deoxyribonuclease I, 20 mM MgSO<sub>4</sub>, 5 mM DTT, and protease inhibitors (cOmplete, Roche, Basel, Switzerland) and lysed by high-pressure cell disruptor (Basic Z Bench Top; Constant Systems Limited, Daventry, Northants, UK) at 25 KPSI. The crude extract was centrifuged at 38,700× RCF for 30 min and filtered through a 0.45 µm filter. The clarified soluble extract was loaded in a HiPrepTMQ XL 16/10 (GE Healthcare Life Sciences, Boston, MA, USA) in loading buffer (50 mM Tris-HCl pH 8.0, 50 mM NaCl, 2 mM EDTA, 5 mM DTT) and eluted with a linear gradient of NaCl (from 0.2 to 1 M).

Fractions corresponding to hGCAP1 were pooled, concentrated, and passed through a HiLoadTM 16/600 SuperdexTM75 pg (GE Healthcare Life Sciences) equilibrated with 20 mM Tris/HCl pH 8.0, 100 mM NaCl, 5 mM DTT, 1 mM CaCl<sub>2</sub>, and one cOmplete protease inhibitor tablet. All the purification steps were performed using an ÄKTA pure 25L (GE Healthcare) at 4 °C and analyzed with SDS-PAGE.

To obtain the apo form of hGCAP1, the protein was further purified using a hydrophobic interaction chromatography, decreasing the NaCl concentration from 300 mM to 0 mM. EGTA was added at 4 mM concentration both in the loading and the elution buffer.

## 2.2. Circular Dichroism

Far-UV Circular Dichroism (CD) spectra of hGCAP1 with and without  $\text{Ca}^{2+}$  were recorded in a Jasco J-810 spectropolarimeter (JASCO Europe, Cremella, Italy) equipped with a Jasco temperature controller module PFD-425S. All measurements were performed in a 0.1 cm path length quartz cuvette at 0.2 mg/mL protein concentration in 20 mM Tris-HCl, pH 7.5, 100 mM NaCl, 2 mM DTT, added with 2 mM  $\text{Ca}^{2+}$  or 2 mM EGTA. Far-UV spectra were recorded from 190 to 260 nm, at 20 and 95 °C (temperature was increased in ramp mode at 1 °C/min).

## 2.3. Analytical Size Exclusion Chromatography

To study the monomer-dimer equilibrium of the  $\text{Ca}^{2+}$ -bound hGCAP1 the protein buffer was exchanged into 20 mM Tris-HCl pH 8.0, 100 mM NaCl, 1 mM DTT, 5 mM  $\text{CaCl}_2$  using a PD-10 Desalting Column (GE Healthcare). Calcium was substituted with 5 mM  $\text{MgCl}_2$  and 2.5 mM EGTA to study the  $\text{Mg}^{2+}$ -bound protein.

Different protein dilutions were prepared (87  $\mu\text{M}$ , 43  $\mu\text{M}$ , 21  $\mu\text{M}$ , 10  $\mu\text{M}$ , 4  $\mu\text{M}$ , 2  $\mu\text{M}$ ) and injected (200  $\mu\text{L}$ ) in a Superdex<sup>TM</sup>75 Increase 10/300 GL column (GE Healthcare Life Science) with 0.8 mL/min flow rate.

Assuming a linear dependency of  $V_e$  from the logarithm of the  $M_w$  ( $V_e = A \times \log(M_w) + B$ ) and assuming that in the presence of a monomer-dimer equilibrium the apparent  $M_w$  is related to the percentage of each species through the equation  $M_w = (\% \text{dim} \times 22.9 + 22.9)$  we get the relation  $V_e = A \times \log((\% \text{dim} \times 22.9 + 22.9)) + B$ . Describing the monomer-dimer equilibrium through the dissociation constant  $K_d$  we arrive at the 3 parameters ( $A$ ,  $B$ , and  $K_d$ ) equation to fit the  $V_e$  vs. concentration (c) curve:

$$V_e = A \cdot \log(22.9 \cdot (1 - K_d/4c \cdot (-1 + (1 + 8c/K_d)^{0.5})) + 22.9) + B$$

## 2.4. Microscale Thermophoresis (MST)

The human GCAP1 was labeled with the red fluorescent dye NT-647-NHS with the Monolith NTTM Protein Labeling kit according to the manufacturer protocol (Nanotemper Technologies, München, Germany). The NT-647-NHS carries a reactive NHS-ester group that reacts with primary amines (lysine residues) to form a covalent bond, achieving about 1:1 ratio of labeled protein to dye. The dye solution was prepared at 30  $\mu\text{M}$  in the supplied labeling buffer. GCAP1 (10  $\mu\text{M}$ ) was diluted in a 1:2 ratio with the labeling solution and incubated at room temperature for 30 min. Sixteen serial dilutions of unlabeled protein were prepared from 46.6  $\mu\text{M}$  to 11.4 nM in 20 mM Tris-HCl, 100 mM NaCl, pH 7.5, 1 mM DTT, 5 mM  $\text{CaCl}_2$  supplied with 0.05% Tween20. Labeled hGCAP1 (10 nM) was added in each of the sixteen dilutions and the reactions were loaded in sixteen capillaries. After confirming that the fluorescence of each capillary was constant, the MST traces were recorded at 24 °C with 40% laser excitation power and 40% MST power.

The same experiments were repeated using a 20 mM Tris-HCl, 150 mM KCl, 5 mM  $\text{MgCl}_2$ , 2.5 mM EGTA, pH 7.5, 1 mM DTT buffer supplied with 0.05% Tween20 to study the magnesium-bound hGCAP1.

All the MST experiments were carried out with a Monolith NT.115 (Nano Temper Technologies).  $K_d$  values were calculated as the average of the triplicate experiments analyzed with MO.Affinity Analysis 3 software.

## 2.5. Dynamic Light Scattering

hGCAP1 were concentrated to 175  $\mu\text{M}$  in 20 mM Tris-HCl pH 8, 5 mM 2-mercaptoethanol, and filtered through a 0.22  $\mu\text{m}$  filter (Merck Millipore Ltd. Burlington, MA, USA). Eighty microliters of protein solution were used to measure hydrodynamic radius by DLS. Measurements were performed

using a DynaPro instrument (Protein Solutions, Charlottesville, VA, USA) in a thermostatic cuvette at 10 °C.

## 2.6. SEC-MALS

Size-Exclusion Chromatography (SEC) combined with Multi-Angle Light Scattering (MALS) detection was performed in an HPLC system composed by a Waters 515 HPLC Pump, a Waters 2487 Dual  $\lambda$  Absorbance detector (Waters, Sesto San Giovanni, Italy), a Wyatt Dawn Heleos MALS and a Wyatt Optila T-rEX differential refractive index detector (Wyatt Technology, Santa Barbara, CA, USA).

200  $\mu$ L of 2 mg/mL GCAP1 samples were run on a Superdex 75 Increase 10/300 GL column (GE Healthcare, Milan, Italy), by using 20 mM Tris-HCl, pH 8, 5 mM 2-mercaptoethanol, with/without 1 mM CaCl<sub>2</sub>, as mobile phase, at a flow rate of 0.8 mL/min. Molar masses were calculated by means of the Astra V software vs. 5.3.4.20 (Wyatt), using a dn/dc value of 0.185.

## 2.7. Trp Fluorescence

The Trp fluorescence of the hGCAP1 was measured diluting the protein concentration at 3  $\mu$ M in the followed three different buffers: calcium buffer (20 mM Tris-HCl, 150 mM KCl, pH 8, 5 mM DTT, 1 mM CaCl<sub>2</sub>), magnesium buffer (20 mM Tris-HCl, 150 mM KCl, pH 8, 5 mM DTT, 1 mM MgCl<sub>2</sub>, 1 mM EGTA), EGTA buffer (20 mM Tris-HCl, 150 mM KCl, pH 8, 5 mM DTT, 1 mM EGTA). All the measurements were performed in a Varian Cary Eclipse fluorescence spectrophotometer using a 280 nm excitation wavelength, 300–400 nm emission wavelength, setting the slit at 10 nm, and the temperature at 25 °C.

## 2.8. SAXS Data Collection

The SAXS data of hGCAP1 were collected with  $\lambda = 0.9919$  Å after elution from the analytic SEC (Superdex75 Increase 10/300 GL) at ESRF beamline BM29 with Pilatus 1M detector with 1 s exposure time.

The 2700 frames of hGCAP1 in EGTA (20 mM Tris-HCl pH 7.5, 150 mM NaCl, 5 mM EGTA, 5 mM DTT) were collected at 20 °C: the selected peak comprised 47 frames (1372–1419) that were scaled in groups of three and subtracted from the buffer (frames 15–194) considering each slightly different concentration (from UV absorbance) before subtraction.

The SEC-SAXS data of hGCAP1 in Mg<sup>2+</sup> (20 mM Tris-HCl pH 8.0, 5 mM MgSO<sub>4</sub>, 2.5 mM EGTA, 150 mM KCl, 5 mM DTT) and Ca<sup>2+</sup>/Mg<sup>2+</sup> (20 mM Tris-HCl pH 8.0, 5 mM CaCl<sub>2</sub>, 5 mM MgSO<sub>4</sub>, 150 mM KCl, 5 mM DTT) were collected at 4 °C. The selected peak of hGCAP1 in Ca<sup>2+</sup>/Mg<sup>2+</sup> at the higher protein concentration comprised 41 frames (1330–1371, buffer frames 172–525). The data analysis was performed using programs PRIMUS 3.0 [18] and ScÅtter 3 (<http://www.bioisis.net>).

## 2.9. Model of hGCAP1 Dimeric Assembly and Molecular Dynamics Simulations

Different possible dimeric conformations were generated using the equilibrated structure of Ca<sup>2+</sup>-loaded hGCAP1 reported in [19] as the monomeric unit. The structure was subjected to three independent rigid body docking simulations using ZDOCK 3.0.2 [20] with a sampling step of 6° (dense sampling) starting from different relative orientations, each resulting in 4000 complexes. All the 12,000 resulting dimers were then filtered according to the distance constraints identified by Lim et al. [15]. The standard deviation of such constraints was increased by 50% to include correctly the distances between C $\alpha$ s and the limits of rigid-body docking, resulting in the following constraints: 42.5 Å < d (E57–E57) < 57.5 Å; 42.5 Å < d (E133–E133) < 57.5 Å, and, 23.5 Å < d (E154–E154) < 32.5 Å. The 3 final dimers, resulting from the highest-scored filtered complex from each of the three docking runs, were then fused to a randomly generated C-terminal (17 amino acids).

The three dimers (d1, d2, and d3) were then subjected to 200 ns all-atom MD simulations using GROMACS v. 2016.1 [21] with CHARMM36m [22] as a force field, after manual addition of the parameters for the myristoylated Gly at the N-term [23]. The simulated systems consisted of a

dodecahedral box ( $\sim 11.5 \times 11.5 \times 8.2 \text{ nm}^3$ ) comprising 30673–33644 water molecules, 93–96  $\text{K}^+$  ions, 13–14  $\text{Mg}^{2+}$  ions, and 95–101  $\text{Cl}^-$  ions for a total of 98566–107500 atoms, depending on the specific dimer. The protocols for energy minimization, equilibration, and production were the same as in Marino et al. [4].

For each trajectory, 2000 frames were extracted at 100 ps intervals and the average  $\chi^2$  with respect to SAXS data over the last 100 ns of the trajectory was calculated using the program CRY SOL 2.8 [24] both considering and discarding the C-term. Indeed, the presence of the highly mobile C-term was found to greatly affect the agreement with SAXS data making it difficult for the selection of the correct dimer interface. To include in the analysis the mobility of each dimeric assembly along with the simulations we used the program EOM 2.1 [25] (with *saxns\_fit2eom* script; <http://xray.utmb.edu/SAXNS>) that builds a mixed model selecting different structures along the simulations to enhance the agreement with SAXS data.

From each trajectory, the frame displaying the lowest absolute  $\chi^2$  without C-ter (i.e., 162 for d1, 1878 for d2, and 1921 for d3) was selected as the representative model for each dimer, namely d1', d2', and d3', respectively.

In such dimers, the two chains were separated and subjected again to rigid-body docking using ZDOCK 2.3 [26]. For each complex, 4 docking simulations were performed (1 with the original relative orientation and 3 with randomly generated orientations) each with 4,000 solutions and rotational sampling  $6^\circ$ . The 16,000 solutions for each complex were clustered into a group of native-like poses having a C $\alpha$  RMSD  $< 1 \text{ \AA}$  with respect to the original complex. The average ZDOCK score (ZD-s) was then calculated for the native-like poses to estimate the binding free energy using the correlation explained in [27] ( $\Delta G^0 = 3.86 - 0.39 \times \text{ZD-s}$ ).

Finally, in silico mutagenesis of the variants known to interfere with the dimerization process, namely H19R, Y22D, F73E, and V77E [15], on both monomers of the best complexes (d1' and d2') were obtained using Maestro (Schrodinger) software. The rotamers for each residue were selected according to the most probable non-clashing rotamer ranked by the "mutate residue" function of Maestro. The four variants were docked using ZDOCK 2.3 [26], using the same protocol as previously described for the WT homodimers, and the relative change in binding free energy with respect to the WT ( $\Delta\Delta G^0$ ) was calculated. The persistence of electrostatic interactions over the 200 ns trajectories was calculated using PyInteraph 1.0 software [28], which calculates the percentage of the trajectory frames where the distance constraints between oppositely charged residues are fulfilled ( $3.5 \text{ \AA}$ ).

### 3. Results

#### 3.1. hGCAP1 Expression and Purification

The recombinant hGCAP1 was expressed in *E. coli* BL21-CodonPlus RP cells with N-terminal myristoylation (Myr). In such conditions, we expected an efficient cut of the N-ter Met ( $>97\%$ ) [29] followed by an effective N-terminal myristoylation ( $>95\%$ ). The protein was purified from the soluble fraction of the cell lysate by ion-exchange chromatography followed by size exclusion chromatography. The purification yield was typically 10 mg (protein)/g (cells).

#### 3.2. Thermal Denaturation of hGCAP1

Thermal denaturation of hGCAP1 with and without  $\text{Ca}^{2+}$  was detected using circular dichroism spectroscopy. The ellipticity at 220 nm of the  $\text{Ca}^{2+}$ /EGTA protein varied from  $-26/-27 \text{ mdeg}$  (at  $20^\circ\text{C}$ ) to  $-19/-22 \text{ mdeg}$  (at  $95^\circ\text{C}$ ) (Figure S1). In both cases, the persistence of the ellipticity signal at high temperature demonstrates a non-complete denaturation of the protein and the conservation of most of the alpha-helical structures. Such evidence suggests that the EF-hand motifs could remain well folded and functional even at extreme conditions [30].

### 3.3. Monomer-Dimer Equilibrium of hGCAP1 in the Presence of $\text{Ca}^{2+}$ or $\text{Mg}^{2+}$

We used analytical size exclusion chromatography (SEC) to study the monomer-dimer equilibrium of hGCAP1 (molecular weight,  $M_w = 22.9$  kDa). Comparing the elution volume ( $V_e$ ) of the  $\text{Ca}^{2+}$  bound hGCAP1 ( $V_e = 10.89$  mL) with that of 5 reference proteins (from Aprotinin,  $M_w = 6.5$  kDa to Conalbumin,  $M_w = 75$  kDa) it was possible to estimate its molecular weight at 49 kDa, compatible with a dimeric assembly. In these experimental conditions, the hGCAP1 concentration at the elution peak, calculated from UV absorbance at 280 nm ( $M_w/\epsilon = 1.07$  mg/mL), was  $17.7$   $\mu\text{M}$ . Reducing the protein concentration, the SEC peak shifted toward higher  $V_e$  (i.e., lower apparent  $M_w$ ), suggesting the presence of a monomer-dimer equilibrium.

To characterize such equilibrium, we performed six analytical SEC experiments in the presence of  $\text{Ca}^{2+}$  (Figure 1A).  $V_e$  depends on protein apparent  $M_w$  which, in turn, is related to the dissociation constant ( $K_d$ ) of the monomer-dimer equilibrium. Therefore, it is possible to represent the variations of  $V_e$  with protein concentration with an equation depending on 3 free parameters, including  $K_d$  (Figure 1C). Using this analysis, we estimated a  $K_d$  of  $8.8 \pm 0.7$   $\mu\text{M}$  for the calcium-bound hGCAP1 (fitting curve in Figure 1, lower left panel).

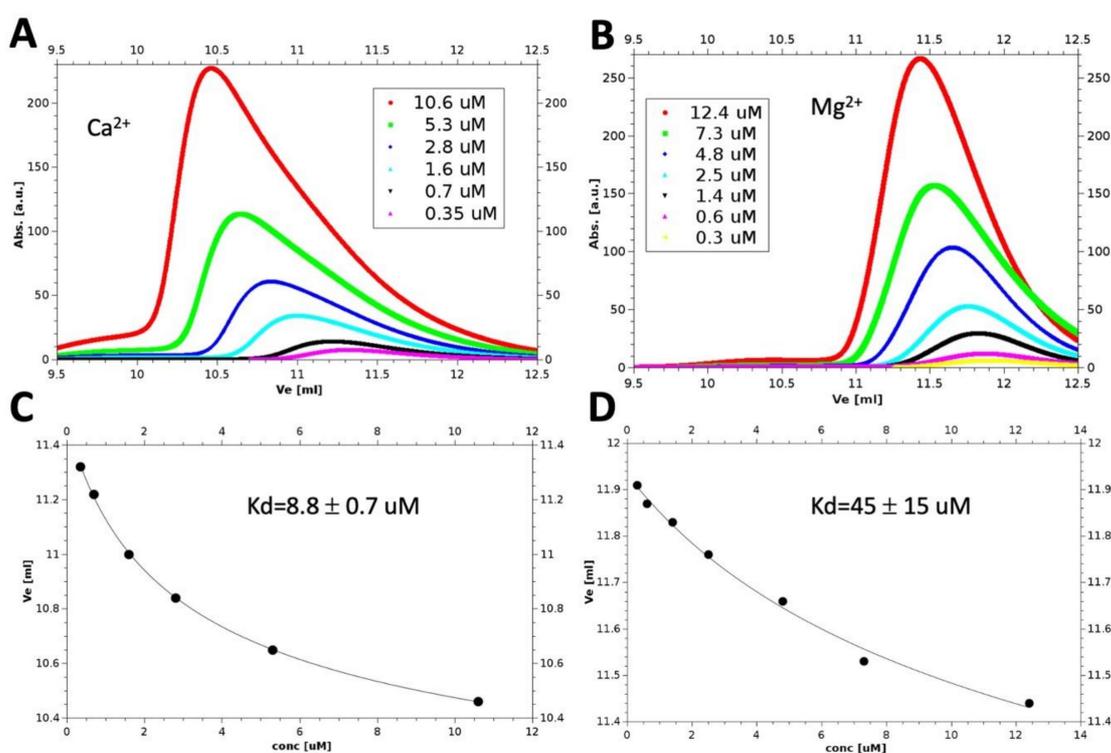


**Figure 1.** Dissociation constants calculated from size exclusion chromatography (SEC) experiments. SEC experiments in presence of  $\text{Ca}^{2+}$  (A) or  $\text{Mg}^{2+}$  (B) at different protein concentrations. In the lower panels (C,D) are reported the corresponding variations of elution volumes ( $V_e$ ) with protein concentration (black dots) together with the 3-parameters theoretical curves fitting the experimental data (black lines).

The same experiment in EGTA/ $\text{Mg}^{2+}$  buffer (Figure 1B) allowed to calculate a higher value for the dissociation constant ( $K_d = 45 \pm 15$   $\mu\text{M}$ ; Figure 1D). These results demonstrate that the  $\text{Ca}^{2+}$  bound protein is more prone to dimerize than the  $\text{Mg}^{2+}$  bound protein.

### 3.4. Monomer-Dimer Equilibrium of hGCAP1 Analysed with Microscale Thermophoresis

We performed additional experiments to determine the hGCAP1 dimer dissociation constant using microscale thermophoresis. We assumed that the labeled protein (with NT-647-NHS fluorescent dye) at low concentration (20 nM) was monomeric. Therefore, the addition of increasing amounts of unlabeled protein-induced changes in labeled protein fluorescence depending on the formation of the dimeric assembly (Figure 2). In this way, we calculated a monomer-dimer dissociation constant for the  $\text{Ca}^{2+}$  bound hGCAP1,  $K_d = 9.4 \pm 1.3 \mu\text{M}$  (Figure 2, blue points/curve) in agreement with the SEC results. The same experiment repeated in the presence of  $\text{Mg}^{2+}$ /EGTA resulted in a  $K_d$  one order of magnitude higher ( $K_d = 77.2 \pm 8.9 \mu\text{M}$ ; Figure 2, red points/curve).

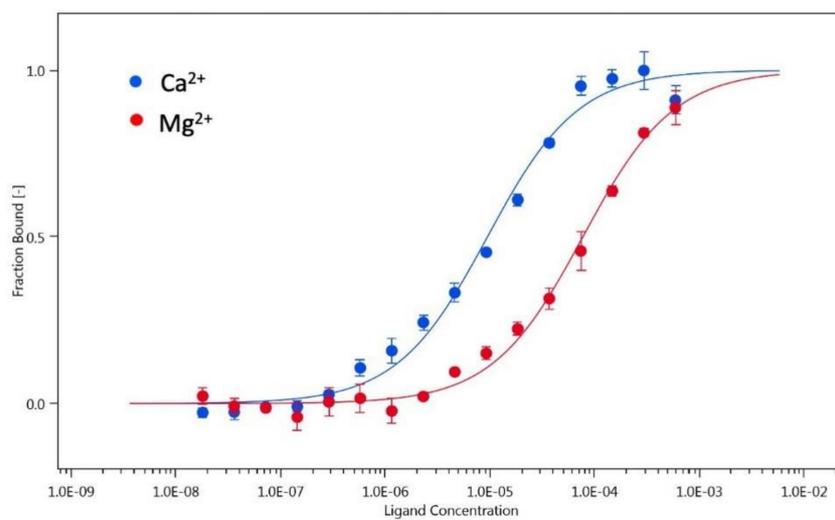


**Figure 2.** Microscale thermophoresis of the hGCAP1 monomer-dimer transition in  $\text{Ca}^{2+}$  and  $\text{Mg}^{2+}$ . Changes in labeled protein fluorescence as a function of unlabeled hGCAP1 concentration in the presence of  $\text{Ca}^{2+}$  (blue points) or  $\text{Mg}^{2+}$  (red points) together with the curves fitting the two experiments (law of mass action) in blue and red, respectively.

### 3.5. Monomer-Dimer Equilibrium Is Affected by Ionic Strength

Additional SEC experiments were performed varying the concentration of apo hGCAP1 (obtained as described in Materials and Methods), in a buffer with low ionic strength (20 mM Tris-HCl, 5 mM 2-mercaptoethanol, pH 8.0). These experiments showed constant values of the elution volumes, indicating the loss of the monomer-dimer equilibrium and the presence of a single quaternary assembly. Multi-angle light scattering coupled with SEC (SEC-MALS) analysis showed an  $M_w$  corresponding to the hGCAP1 monomer ( $M_w \sim 23 \text{ kDa}$ ; Figure 3, red curve). In low ionic strength conditions, hGCAP1 remained monomeric even at high concentration (175  $\mu\text{M}$ ), as shown in dynamic light scattering (DLS) experiments that estimated an  $M_w$  of 24 kDa (18% polydispersion).

Interestingly, the addition of a low amount of calcium (1 mM) to the salt-free buffer was sufficient to induce again the monomer-dimer equilibrium, with a protein molecular weight calculated from MALS of about 29 kDa (Figure 3, blue curve). The slightly higher hydrodynamic radius of the apoprotein (Figure 3, red curve) can be explained by intramolecular repulsive effects due to the protein net charge in the salt-free buffer and by the increased exposition of hydrophobic surface that requires a thicker solvation shell [30].

An analogous result was also observed for chicken GCAP1 (data not shown) demonstrating that the binding of calcium is a determinant factor to promote GCAP1 dimerization.

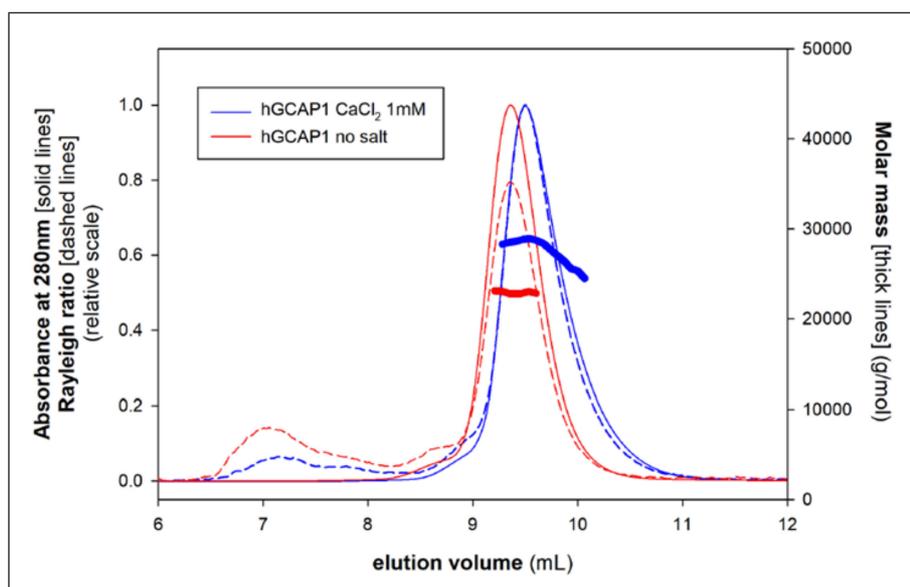


**Figure 3.** Multi-angle light scattering coupled with SEC (SEC-MALS) of hGCAP1 in the salt-free buffer. Without salt hGCAP1 is monomeric ( $M_w$  23 kDa; red curves) and it moves toward the monomer-dimer equilibrium upon the addition of 1 mM  $\text{Ca}^{2+}$  ( $M_w$  ~ 29 kDa, blue curves). The thick lines represent the molar mass measured by MALS (legend on the right) in correspondence to each SEC peak (solid lines; legend on the left); the dashed lines represent the scattering signal (legend on the left).

### 3.6. hGCAP1 Trp Fluorescence in the Different Ion Binding States

hGCAP1 hosts 2 tryptophan residues: Trp21, in the Myr cavity, and Trp94, between EF2 and EF3 hand motifs. The Trp fluorescence measured in the presence of  $\text{Mg}^{2+}$  or EGTA showed similar values of maximum emission wavelength (343.5 and 343.3 nm, respectively). Such values are correlated with significant solvent exposure of tryptophan, as discussed by Vivian and Callis [31], that showed a variation range of maximum emission wavelength between 310 and 350 nm for completely buried or completely exposed Trp, respectively. In the presence of saturating  $\text{Ca}^{2+}$  concentration (5 mM) we registered a 2 nm redshift of the emission peak (345.2 nm), indicating that  $\text{Ca}^{2+}$  binding slightly increases the solvent exposure of Trp (Figure S2). Such evidence suggests a slightly higher hydrodynamic radius of the  $\text{Ca}^{2+}$ -bound form in agreement with the lower elution volumes observed in SEC experiments (Figure 1, upper panels). Similar behavior was observed for bovine GCAP1 which showed a change from 345 to 347 nm upon  $\text{Ca}^{2+}$  addition [32]. Such structural changes induced in GCAP1 by calcium-binding are likely correlated with the promotion of the dimeric assembly as observed for the  $\text{Ca}^{2+}$  bound protein with respect to the  $\text{Mg}^{2+}$  bound moiety.

### 3.7. SAXS Analysis of the hGCAP1 Monomer

The SEC-SAXS analysis of hGCAP1 at low concentration (10.9  $\mu\text{M}$ ) (analyzed using programs PRIMUS 3.0 [18] and ScÅtter 3 (<http://www.bioisis.net/>)) without  $\text{Ca}^{2+}$  (20 mM Tris-HCl pH 7.5, 150 mM NaCl, 5 mM EGTA, 5 mM DTT) showed a  $M_w$ , estimated from scattering intensity relative to water at zero angle ( $I_0 = 18.29 \pm 0.06$ ), of 21.1 kDa [33], compatible with a monomeric assembly ( $R_g = 21.7 \pm 0.1$  Å; Figure 4A). After regularization and real space transformation (program GNOM; ATSAS 3.0.1 [34];  $D_{\text{max}} = 60$  Å; Figure 4B) the superposition of a typical low resolution model (program DAMMIN 5.3 [35]; Figure 4, upper panel) on cGCAP1 crystal structure (pdb-id: 2r2i;  $D_{\text{max}} \sim 50$  Å; Figure 4C) shows that hGCAP1 occupies a slightly larger volume. Anyway, the modest agreement of cGCAP1 with the SAXS data (program CRY SOL [24];  $\chi^2 = 2.62$ ) was greatly improved by the addition of the missing 17 C-terminal residues (with program CORAL 1.1 [36];  $\chi^2 = 1.43$ ; Figure 4D,E).

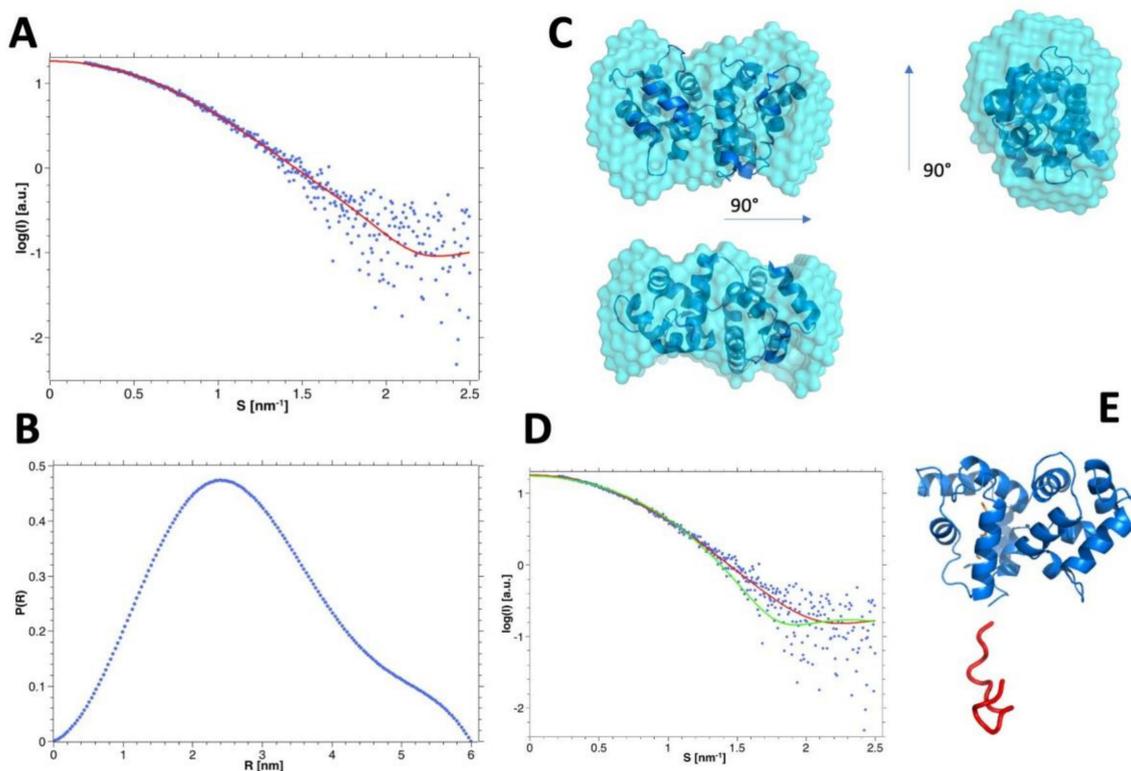


**Figure 4.** SEC-SAXS data of hGCAP1 monomer. (A) experimental SEC-SAXS data of hGCAP1 without  $\text{Ca}^{2+}$  or  $\text{Mg}^{2+}$  at  $10.9 \mu\text{M}$  ( $R_g = 21.5 \text{ \AA}$ ; blue points) with GNOM regularization (red line) and (B) corresponding  $P(R)$  ( $D_{\text{max}} = 60 \text{ \AA}$ ). (C) DAMMIN most typical low-resolution model (cyan surface; ensemble resolution =  $25 \pm 2 \text{ \AA}$ ; superposed to the crystal structure of cGCAP1 (NSD 2.09; pdb-id 2r2i;  $R_g = 19.8 \text{ \AA}$ ; blue cartoons). (D) experimental data fitted with cGCAP1 without C-ter (CRY SOL  $\chi^2 = 2.62$ ; green curve) or with C-ter (added with CORAL; red curve;  $\chi^2 = 1.43$ ). (E) hGCAP1 model obtained adding to the chicken protein (blue cartoons) the C-ter with coral (red cartoon). The pictures of protein structures were prepared with the PyMOL 2.2.0 program (The PyMOL Molecular Graphics System, Version 2.0 Schrödinger, LLC).

### 3.8. SEC-SAXS Evidence of the Monomer-Dimer Equilibrium

We collected SEC-SAXS data of hGCAP1 in different buffers and at different protein concentrations. The SEC absorbance peaks were used to estimate protein concentrations to properly scale the scattering data before averaging and buffer subtraction. By comparing the scattering data extrapolated at zero angles of protein and water as a reference, it is possible to estimate the protein Mw (Table 1). As discussed above, apo hGCAP1 (in EGTA) is monomeric at low concentration ( $10.9 \mu\text{M}$ ). On the contrary, when bound to  $\text{Ca}^{2+}$  or  $\text{Mg}^{2+}$ , hGCAP1 evolves toward different monomer-dimer equilibria whose  $K_d$  depends on the binding state of the EF-hands motifs, as already described.

In particular,  $\text{Ca}^{2+}$  bound protein displays an Mw varying from 35.2 kDa (at  $25.3 \mu\text{M}$ ) to 43.7 (at  $51.1 \mu\text{M}$ ).

**Table 1.** SEC-SAXS parameters for hGCAP1 in different conditions.

Buffer	Conc. [ $\mu\text{M}$ ] <sup>a</sup>	R <sub>g</sub> [Å]	I <sub>0</sub>	Mw (I <sub>0</sub> ) <sup>c</sup> [kDa]	% mon.	D <sub>max</sub> [Å]	Mw (V <sub>c</sub> ) [kDa]	Mw (q <sub>max</sub> ) [kDa]
EGTA	10.9	21.5	18.2	21.1	100	60	29.4	28.2
Mg <sup>2+</sup>	59.4	22.4	32.3	35.9	43	75	29.0	28.8
Ca <sup>2+</sup> /Mg <sup>2+</sup>	25.3	24.1	31.6	35.2	46	76	27.4	27.1
Ca <sup>2+</sup> /Mg <sup>2+</sup>	51.1	24.5	39.2	43.7	9	81	35.2	38.0
Ca <sup>2+</sup> /Mg <sup>2+</sup>	~76 <sup>b</sup>	24.5	-	-	-	81	40.8	45.6

<sup>a</sup> Concentrations based on peak absorbance. <sup>b</sup> This concentration was not measured directly due to experimental problems; therefore, the reported value is estimated, and it does not allow the analysis based on I<sub>0</sub> values.

<sup>c</sup> Mw calculated using the program PRIMUS and relative scale respect to water I<sub>0</sub> (0.0156 for EGTA sample and 0.0162 for the other samples).

The SEC-SAXS data of calcium bound GCAP1 collected at the higher protein concentration (~76  $\mu\text{M}$ ; Table 1), corresponding to a prevalent dimeric assembly (R<sub>g</sub> = 24.5 ± 0.1 Å), were regularized and transformed in real space with the program GNOM (ATSAS 3.0.1) [34]; real space R<sub>g</sub> = 24.8 ± 0.1 Å, D<sub>max</sub> = 80 Å; Figure 5A), and then used to produce several low resolutions models using DAMMIF (ATSAS 3.0.1) with P2 symmetry ([37]; ensemble resolution = 29 ± 2 Å; Figure 5C). These data were also used to select between different possible dimeric assemblies as described in the next paragraph.

### 3.9. Modelling and Selection of Possible Dimeric Assemblies

The three-dimensional structural model for hGCAP1 (201 amino acids, 22.9 kDa) was obtained by homology modeling using the X-ray structure of cGCAP1 (pdb-id: 2r2i, sequence identity of 84%; [38]) as a template. Analysis of the possible protein-protein interfaces hosted in the cGCAP1 crystallographic packing of the chicken protein with the PDBePISA server [39] did not reveal any stable dimeric assembly. However, previous work [15] based on DEER provided structural hints as to the dimeric nature of bovine GCAP1 and defined specific distance-constraints among residues belonging to each monomer, resulting in two alternative dimeric assemblies a symmetric and an asymmetric one.

In view of these lines of evidence, the homology modeled and equilibrated structure of hGCAP1 described by Marino and Dell'Orco [19] was used to produce 12,000 random dimers with rigid body docking using the program ZDOCK 3.0.2 [20]. The dimers were then filtered according to the distance constraints between the 4 residues identified by Lim et al., [15] i.e., His19, Tyr22, Phe73, and Val77 (see Methods) resulting in 36 to 43 filtered poses for each independent docking run obtained by randomizing the initial position of the probe. The three assemblies presenting the highest ZDOCK 3.0.2 score in each independent and randomized docking run (p1, p2, and p3) were significantly different from each other (C $\alpha$ -RMSD values were: 4.48 Å for p1–p2, 14.49 Å for p2–p3 and 12.73 Å for p1–p3). The three best-scored dimers (from now on named dimers d1, d2, and d3) were then fused with a randomly generated C-terminus and subjected to 200 ns all-atom MD simulations sampling a total of 2000 frames (one every 100 ps).

Firstly, we analyzed the agreement of the identified dimers along each respective MD trajectory omitting the highly mobile C-terminal tail (i.e., the last 17 amino acids) of every monomer. The average  $\chi^2$  calculated on the final 50 ns of the MD simulations (Figure S3) shows that dimers d2 and d3 display a comparable agreement with scattering data ( $\langle\chi^2\rangle = 2.79$  and 3.71, respectively), whereas d1 exhibits a poorer agreement ( $\langle\chi^2\rangle = 13.45$ ). The ranking changes when considering in the models also the conformations of C-ter, with d1 and d2 being in comparable agreement with SAXS ( $\langle\chi^2\rangle = 3.02$  and 3.40, respectively) and d3 in disagreement ( $\langle\chi^2\rangle = 13.79$ ) (Figure S4). To take into account also the dynamics of the proteins along with the 3 simulations (including the C-ter) we used the program EOM 2.0 (Ensemble Optimisation Method; [25]) that builds a mixed/dynamical model for every simulation with the weighed contribution of different structural states to fit the SAXS data. Again, the dynamical

analysis confirmed d1 and d2 as the best assemblies ( $\chi^2 = 1.16$  and  $1.17$ , respectively) and d3 as the worst ( $\chi^2 = 2.37$ ) (Figure 5B).

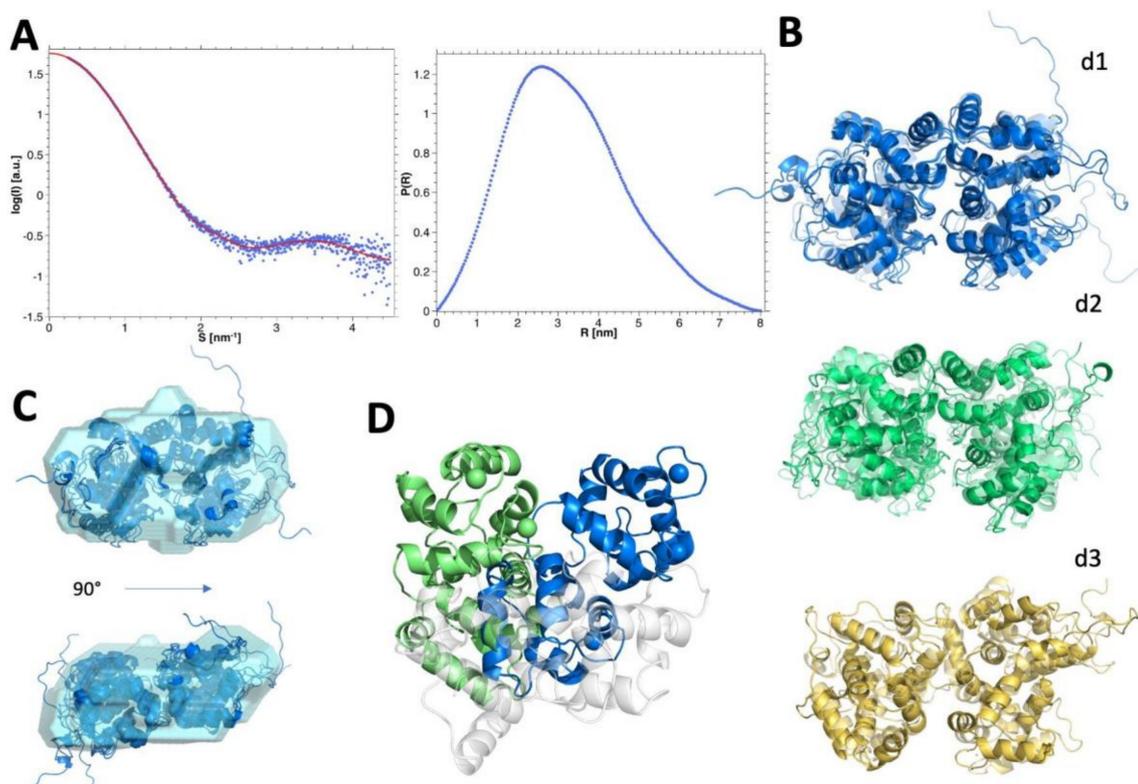


**Figure 5.** SEC-SAXS data of hGCAP1 dimer. (A) GNOM fitting (red line) of the SEC-SAXS data (blue points) at the higher protein concentration and corresponding  $P(R)$ . (B) Dynamical EOM models of the 3 dimeric assemblies—d1-d3—in cartoons with transparency depending on the occupation of each structure on the assembly. (C) Superposition of the dynamical model d1 (blue cartoon) on one of the most representative low-resolution models (DAMMIF, P2 symmetry, ensemble resolution =  $29 \pm 2$  Å, NSD 1.67) depicted as the cyan surface in 2 different orientations. (D) Different orientation of the monomers d1'—blue cartoons and d2'—green cartoons in the static dimeric assemblies (the superposed monomer is shown as white transparent cartoons).

To summarize, the agreement with SAXS data of d1 and d2 improves by adding the C-ter amino acids and it gets even better when protein dynamics are explicitly considered. On the contrary d3—the best dimer in the absence of C-ter—worsens considerably when taking into account the contribution of the C-ter end.

For each MD simulation, the structural conformation showing the lowest  $\chi^2$  with respect to the SAXS data (without C-ter; Table 2) (named d1', d2', d3') was subjected again to rigid-body docking using another version of the ZDOCK algorithm (ZDOCK 2.3) to obtain an estimate of the free energy of binding, using an empirical correlation with the ZDOCK score as explained in [27]. This approach has demonstrated to be useful to predict *in silico* the effects of any point mutation affecting the dimer interface on the relative free energy of binding ( $\Delta\Delta G^0$ ), under the assumption that mutations do not significantly perturb the structure of each interacting molecule. The scores of SAXS and ZDOCK analysis are reported in Table 2.

**Table 2.** Agreement with SAXS data and ZDOCK analysis and for the 3 selected models d1', d2', d3'.

Assembly	'Static' $\chi^2$ with SAXS <sup>a</sup>	'Dynamic' $\chi^2$ with SAXS <sup>b</sup>	ZD-s <sup>c</sup>	Native-Like Poses <sup>c</sup>	Best Ranked Poses <sup>d</sup>
d1'	2.42	1.16	54.4 ± 0.8	22	1
d2'	1.95	1.17	44.5 ± 0.9	24	16
d3'	2.08	2.37	44.9 ± 0.7	16	1

<sup>a</sup>  $\chi^2$  values of selected individual structures along with the MD simulation without the C-ter. <sup>b</sup>  $\chi^2$  values of selected mixed structures along with the MD simulation with the C-ter. <sup>c</sup> Average score of native-like poses (i.e., within 1 Å C $\alpha$ -RMSD with respect to the original complex) from multiple docking runs. <sup>d</sup> Rank of the native-like pose with the highest score out of 12,000 poses.

### 3.10. Computational Analysis of Mutations in hGCAP1 Dimeric Assembly

All the dimers predicted by the rigid-body docking algorithm accounting for shape and electrostatic complementarity and desolvation of residues buried at the dimer interface (ZDOCK 2.3) resulted in high-score poses, and 16–24 of the 12,000 poses reconstituted within 1 Å (C $\alpha$ -RMSD; “native-like” poses; Table 2) with respect to dimers d1', d2', d3' (Table 2). As it has been proven that, in the absence of major conformational changes in either of the interacting protein, a correlation exists between the average docking score of native-like poses and the standard free energy of binding, we performed *in silico* mutations to generate the variants shown to disrupt the dimer and shift the equilibrium toward the monomer, namely F73E, H19R, V77E, and Y22D [15]. Interestingly, for all of the three dimers, the mutations resulted in a lower number of native-like poses still fulfilling the DEER distance constraints (Table 3). The computational analysis of the 12 mutagenized homodimers (ZDOCK 2.3; Table 3), shows for all the structures a shift toward the monomeric form, in line with the experimental results [15], though to a different extent (Table 3). Indeed, for every assembly, the H19R variant has a greater effect on the stability of the dimer. The predicted effects of the four point mutations on the  $\Delta\Delta G^0$  values are high for all the dimers but are especially apparent for d1', for which a 4.5 to 5.8 kcal/mol effect was predicted, which would strongly shift the equilibrium toward the monomeric form.

**Table 3.** Effect of the mutations on Z-dock scores and prediction of the relative free energy of binding.

Assembly	Mutant	Native-Like Poses	$\Delta ZD-s$	$\Delta\Delta G^0$ * [kcal/mol]
D1'	F73E	15	−13.14	5.12
	H19R	12	−14.75	5.75
	V77E	21	−11.62	4.53
	Y22D	17	−12.20	4.76
D2'	F73E	12	−2.65	1.04
	H19R	8	−4.85	1.89
	V77E	9	−4.15	1.62
	Y22D	9	−4.70	1.84

\*  $\Delta\Delta G^0$  was calculated by using an empirical correlation between ZD-s and  $\Delta G^0$  as explained in [27] and in [40].

Considering together the agreement with SAXS data and the overall Z-DOCK results we can select d1 and d2 as the best dimeric assemblies with the lower “dynamical”  $\chi^2$  vs. SAXS data, the highest docking score, and the higher perturbing effect of the mutations on the dimeric assembly. The good agreement of the d1 dynamical model with SAXS data is further shown in the superposition with one of the low-resolution DAMMIF models (NSD 1.67; Figure 5C).

### 3.11. Insights into the Molecular Interface of the Most Likely Dimers d1 and d2

The different orientation between the monomers in the alternative dimeric assemblies d1' and d2' is shown in Figure 5D, evidencing a rotation of about 60°. Molecular dynamics simulations showed

that the interface between dimers d1 and d2 involved persistent electrostatic interactions between the negatively charged residues of the EF2 loop involved in  $\text{Ca}^{2+}$ -coordination, namely D68, D72, and E75, and the positively charged residues of the entering helix of EF3 (Figure S5), namely R93 and K97, although with peculiarities for each dimer. Specifically, dimer d1 exhibited persistent interactions between R93 and D68 (70.6% of the simulation time), R93 and D72 (18.3%), and R93 and E75 (18.7%). Such switching electrostatic interactions hinged on R93 were completely absent in dimer d2, which on the other hand showed electrostatic interactions hinged on K97 (with D68 (7.1%), D72 (72.9%), and E75 (18%)), also negligible in d1.

When an accurate analysis of the static interface of dimers d1' and d2' was performed by Bioluminate (version 3.9.072, Schroedinger), a slightly increased buried solvent accessible surface area for d2' (245.1  $\text{\AA}^2$ ) with respect to d1' (219.4  $\text{\AA}^2$ ) with a similar shape complementarity score (2487 vs. 2541) were measured. Interestingly, F73 was found to be involved in a  $\pi$ -stacking interaction in both interfaces, specifically with Y22 in dimer d1' and with F65 in dimer d2'. Finally, the static analysis confirmed the electrostatic interactions involving D72 specifically with R93 in d1' (salt bridge) and with K97 in d2' (charge-reinforced H-bond), which could contribute to the highest docking score (ZD-s) of the first dimeric assembly (Table 2). In conclusion, both static and dynamic analyses of the dimeric interfaces show a balance of stabilizing interactions, that does not allow to define which one among d1' and d2' is the most representative hGCAP1 dimer.

#### 4. Discussion

SAXS data on hGCAP1 at a low concentration (10.9  $\mu\text{M}$ ) without  $\text{Ca}^{2+}$  or  $\text{Mg}^{2+}$  are compatible with a monomeric protein whose structure is in good agreement with the crystal structure of chicken GCAP1 as long as the C-ter end is included in a loose conformation (causing the increase of the radius of gyration from 19.8 to 21.0  $\text{\AA}$ ).

Purified hGCAP1 analyzed with different experimental techniques shows the equilibrium between monomer and dimer. Since the protein has a theoretical isoelectric point of 4.4 and is negatively charged at physiological pH, we expect a prevailing effect of electrostatic repulsions at low salt concentration shifting the equilibrium towards the monomeric state, as observed in SEC-MALS experiments. The electrostatic repulsion is partially shielded by binding one/two  $\text{Mg}^{2+}$  ions or, to a greater extent, by three  $\text{Ca}^{2+}$  ions. Indeed, we observed that at low salt concentration the addition of a small amount (1 mM) of calcium is sufficient to push the monomeric state toward the monomer-dimer equilibrium. In conditions closer to the physiological state, i.e., at medium salt concentration and in the  $\text{Ca}^{2+}$ -bound state, hGCAP1 displays a monomer-dimer equilibrium with  $K_d \sim 9 \mu\text{M}$ . When the 3 calcium ions are exchanged with one/two  $\text{Mg}^{2+}$  the higher electrostatic repulsion screen decreases the dimerization  $K_d$  ( $\sim 60 \mu\text{M}$ ).

Interestingly, also the chicken protein, despite being monomeric in the crystal structure, displays a similar dynamic monomer-dimer equilibrium (not shown), showing that this property is common to different GCAP1 orthologs.

The shift toward dimeric assembly favored in the presence of  $\text{Ca}^{2+}$  can also explain the protein resistance to trypsin with respect to the unbound state observed in previous works [41,42].

The differences in monomer-dimer equilibrium suggest conformational changes induced by GCAP1 ligation state as observed with Trp fluorescence experiments, that are likely related to GCAP1 regulatory activity on retGC1, as suggested by thorough MD simulations [19].

Using a combination of computational techniques, we produced 3 models of reliable dimeric interfaces compatible with the restrains reported by Lim et al., [15]. In every model, the dimeric interface is based on the N-terminal domain of GCAP1, already known to be involved in both protein dimerization and the interaction with retGC1 [6]. Our docking simulations confirmed the crucial role of the residues identified in bovine GCAP1 by Lim et al. [15] in stabilizing the dimeric assembly, as their in silico substitutions resulted in a dramatic increase of  $\Delta\Delta G^0$  values, compatible with a shift of hGCAP1 to its monomeric form. It is interesting to highlight that the higher destabilization is associated

with the substitution involving H19 for both d1' and d2' (Table 3). The H19Y mutation was recently identified in patients diagnosed with retinitis pigmentosa [13]. Indeed, the mutant showed a profound shift in  $\text{Ca}^{2+}$ -sensitivity of RetGC regulation and, in line with our present observations, its oligomeric equilibrium did not shift to the dimer in the presence of  $\text{Ca}^{2+}$ , thus suggesting a correlation between GCAP1 physiological role and its dimerization.

## 5. Conclusions

Monomer–dimer equilibrium in proteins is determined by a subtle balance between stabilizing and destabilizing forces [43]. Based on our models, only a small accessible surface area is buried on dimer formation (~9% of the total protein surface). Such surface is nonetheless sufficient to create strong electrostatic and shape complementarity between the monomers and suggests a high contribution of the hydrophobic effect to the process of desolvation of the protein–protein interface, which is reflected in the high docking scores (Table 2). The hydrophobic contacts at the GCAP1 dimer interface have been proven to be essential for both its dimerization and for the activation of RetGC, which is itself a dimer, thus suggesting that the GCAP1 dimer may bind to the cyclase target to form a 2:2 complex, whose allosteric regulation of catalytic activity may involve quaternary structural changes in a protein–protein complex [16]. An alternative explanation for the role of bGCAP1 dimerization has been proposed by Lim et al. [15]. In the absence of bRetGC, the dimeric nature of bGCAP1 in the photoreceptor inner segment may prevent its diffusion into the outer segment. The partial overlap of the bGCAP1–bRetGC and bGCAP1–bGCAP1 interface suggests that, as soon as retGC becomes available, a tight intermolecular interaction would occur, which allows the mature RetGC/GCAP1 complex to incorporate in transport vesicles that are then transported to the outer segments, where the complex could then translocate into disk membranes [15]. However, the actual physiological role of GCAP1 dimerization in human photoreceptors is not completely clarified and is only partially compatible with such a hypothesis. Assuming that the intracellular concentration of hGCAP1 is similar to that of bGCAP1 in bovine rod outer segments [44], namely 3.3  $\mu\text{M}$ , our experimentally determined  $K_d$  values would lead to ~33% of hGCAP1 being dimeric at high  $\text{Ca}^{2+}$ , and only ~9% at low  $\text{Ca}^{2+}$ , in the  $\text{Mg}^{2+}$ -bound state. The apparent affinity of hGCAP1 for hRetGC (3.2  $\mu\text{M}$ , see [30]) is 3-fold higher than the affinity of dimerization in the presence of  $\text{Ca}^{2+}$  (9  $\mu\text{M}$ ) and 19-fold higher than that in  $\text{Mg}^{2+}$  (~60  $\mu\text{M}$ ), therefore hGCAP1 would rather bind to its target regulator than to itself under both conditions. Dimerization of hGCAP1 could then rather serve as a regulatory mechanism to prevent an excessive diffusion to the outer segment in the absence of RetGC, and not necessarily a condition to achieve a 2:2 complex. An updated estimate of the intracellular concentration of both GCAP1 and retGC in human photoreceptors is therefore necessary to clear up the actual molecular scenario.

GCAP1 structural changes related to the presence of  $\text{Ca}^{2+}$  or  $\text{Mg}^{2+}$  are reflected in the observed changes of the dimer dissociation constant. Such conformational changes are likely related to the mechanisms of GCAP1 to control the activity of the retGC1 partner, and therefore their investigation here described represents a step forward to dissect the structural bases of the regulatory mechanism of GCAP1.

**Supplementary Materials:** The following are available online at <http://www.mdpi.com/2218-273X/10/10/1408/s1>, Figure S1: Thermal denaturation of hGCAP1 with (green line) and without  $\text{Ca}^{2+}$  (blue line) using circular dichroism spectroscopy; Figure S2: Scaled curves of GCAP1 Trp fluorescence in different conditions: it is possible to note the redshift of the peak corresponding to  $\text{Ca}^{2+}$ -bound protein; Figure S3: Agreement between SAXS data and dimeric models d1, d2 and d3 without the last 8 residues at the C-ter (calculated using program Crysol) along with the 200 ns MD simulations; Figure S4: Agreement between SAXS data and dimeric models d1, d2 and d3 (calculated using program Crysol) along with the 200 ns MD simulation; Figure S5: Orientation of monomer B with respect to monomer A in dimers d1' and d2' and different pattern of electrostatic interactions.

**Author Contributions:** F.B. conducted most of the experiments, and C.B. and A.B. conducted some experiments; V.M. run molecular modeling and MD simulations; D.D. designed the modeling parts and wrote the paper; E.M. contributed to data analysis and wrote the paper; M.M. supervised the work, designed the experiments, collected and analyzed SAXS data and wrote the paper. All authors have read and agreed to the published version of the manuscript.

**Funding:** This work was funded by a grant from Fondazione Telethon–Italy (grant no. GGP16010 to D.D. and M.M.), and by a grant from Instruct-ERIC (grant no. Appid. 586 to M.M.).

**Acknowledgments:** We would like to thank ESRF and all the staff of beamline BM29 and in particular Mark Tully and Martha Brennich for assistance in SAXS data collection. We would like to thank Patrice Vachette for fruitful discussions about SAXS data analysis.

**Conflicts of Interest:** The authors declare no conflict of interest.

## References

1. Koch, K.-W.; Edell'Orco, D. Protein and Signaling Networks in Vertebrate Photoreceptor Cells. *Front. Mol. Neurosci.* **2015**, *8*, 67. [[CrossRef](#)] [[PubMed](#)]
2. Peshenko, I.V.; Cideciyan, A.V.; Sumaroka, A.; Olshevskaya, E.V.; Scholten, A.; Abbas, S.; Koch, K.-W.; Jacobson, S.G.; Dizhoor, A.M. A G86R mutation in the calcium-sensor protein GCAP1 alters regulation of retinal guanylyl cyclase and causes dominant cone-rod degeneration. *J. Biol. Chem.* **2019**, *294*, 3476–3488. [[CrossRef](#)] [[PubMed](#)]
3. Lim, S.; Peshenko, I.V.; Olshevskaya, E.V.; Dizhoor, A.M.; Ames, J.B. Structure of Guanylyl Cyclase Activator Protein 1 (GCAP1) Mutant V77E in a Ca<sup>2+</sup>-free/Mg<sup>2+</sup>-bound Activator State. *J. Biol. Chem.* **2015**, *291*, 4429–4441. [[CrossRef](#)] [[PubMed](#)]
4. Marino, V.; Sulmann, S.; Koch, K.-W.; Dell'Orco, D. Structural effects of Mg<sup>2+</sup> on the regulatory states of three neuronal calcium sensors operating in vertebrate phototransduction. *Biochim. Biophys. Acta (BBA) Bioenerg.* **2015**, *1853*, 2055–2065. [[CrossRef](#)] [[PubMed](#)]
5. Ermilov, A.N.; Olshevskaya, E.V.; Dizhoor, A.M. Instead of Binding Calcium, One of the EF-hand Structures in Guanylyl Cyclase Activating Protein-2 Is Required for Targeting Photoreceptor Guanylyl Cyclase. *J. Biol. Chem.* **2001**, *276*, 48143–48148. [[CrossRef](#)] [[PubMed](#)]
6. Otto-Bruc, A.; Buczyłko, J.; Surgucheva, I.; Subbaraya, I.; Rudnicka-Nawrot, M.; Crabb, J.W.; Arendt, A.; Hargrave, P.A.; Baehr, A.W.; Palczewski, K. Functional Reconstitution of Photoreceptor Guanylate Cyclase with Native and Mutant Forms of Guanylate Cyclase-Activating Protein 1. *Biochemistry* **1997**, *36*, 4295–4302. [[CrossRef](#)]
7. Viviano, J. Evolutionary Interrelationships and Insights into Molecular Mechanisms of Functional Divergence: An Analysis of Neuronal Calcium Sensor Proteins. *J. Phylogenetics Evol. Biol.* **2013**, *1*, 1–8. [[CrossRef](#)]
8. Manes, G.; Mamouni, S.; Hérald, E.; Richard, A.-C.; Sénéchal, A.; Aouad, K.; Bocquet, B.; Meunier, I.; Hamel, C.P. Cone dystrophy or macular dystrophy associated with novel autosomal dominant GUCA1A mutations. *Mol. Vis.* **2017**, *23*, 198–209.
9. Payne, A.M.; Downes, S.M.; Bessant, D.A.; Taylor, R.; Holder, G.E.; Warren, M.J.; Bird, A.C.; Bhattacharya, S.S. A mutation in guanylate cyclase activator 1A (GUCA1A) in an autosomal dominant cone dystrophy pedigree mapping to a new locus on chromosome 6p21.1. *Hum. Mol. Genet.* **1998**, *7*, 273–277. [[CrossRef](#)]
10. Behnen, P.; Dell'Orco, D.; Koch, K.-W. Involvement of the calcium sensor GCAP1 in hereditary cone dystrophies. *Biol. Chem.* **2010**, *391*, 631–637. [[CrossRef](#)]
11. Marino, V.; Scholten, A.; Koch, K.-W.; Dell'Orco, D. Two retinal dystrophy-associated missense mutations in GUCA1A with distinct molecular properties result in a similar aberrant regulation of the retinal guanylate cyclase. *Hum. Mol. Genet.* **2015**, *24*, 6653–6666. [[CrossRef](#)] [[PubMed](#)]
12. Vocke, F.; Weisschuh, N.; Malfatti, S.; Marino, V.; Jacobson, S.G.; Reiff, C.M.; Dell'Orco, D.; Koch, K.-W. Dysfunction of cGMP signalling in photoreceptors by a macular dystrophy-related mutation in the calcium sensor GCAP1. *Hum. Mol. Genet.* **2016**, *26*, 133–144. [[CrossRef](#)] [[PubMed](#)]
13. Abbas, S.; Marino, V.; Weisschuh, N.; Kieninger, S.; Solaki, M.; Dell'Orco, D.; Koch, K.-W. Neuronal Calcium Sensor GCAP1 Encoded by GUCA1A Exhibits Heterogeneous Functional Properties in Two Cases of Retinitis Pigmentosa. *ACS Chem. Neurosci.* **2020**, *11*, 1458–1470. [[CrossRef](#)]
14. Olshevskaya, E.V. Dimerization of Guanylyl Cyclase-activating Protein and a Mechanism of Photoreceptor Guanylyl Cyclase Activation. *J. Biol. Chem.* **1999**, *274*, 25583–25587. [[CrossRef](#)] [[PubMed](#)]
15. Lim, S.; Roseman, G.; Peshenko, I.; Manchala, G.; Cudia, D.; Dizhoor, A.M.; Millhauser, G.; Ames, J.B. Retinal guanylyl cyclase activating protein 1 forms a functional dimer. *PLoS ONE* **2018**, *13*, e0193947. [[CrossRef](#)]
16. Ames, J.B. Dimerization of Neuronal Calcium Sensor Proteins. *Front. Mol. Neurosci.* **2018**, *11*, 397. [[CrossRef](#)]

17. Pierce, B.G.; Wiehe, K.; Hwang, H.; Kim, B.-H.; Vreven, T.; Weng, Z. ZDOCK server: Interactive docking prediction of protein-protein complexes and symmetric multimers. *Bioinformatics* **2014**, *30*, 1771–1773. [[CrossRef](#)]
18. Konarev, P.V.; Volkov, V.; Sokolova, A.; Koch, M.H.J.; Svergun, D.I. PRIMUS: A Windows PC-based system for small-angle scattering data analysis. *J. Appl. Crystallogr.* **2003**, *36*, 1277–1282. [[CrossRef](#)]
19. Marino, V.; Dell’Orco, D. Allosteric communication pathways routed by Ca<sup>2+</sup>/Mg<sup>2+</sup> exchange in GCAP1 selectively switch target regulation modes. *Sci. Rep.* **2016**, *6*, 34277. [[CrossRef](#)]
20. Pierce, B.G.; Hourai, Y.; Weng, Z. Accelerating Protein Docking in ZDOCK Using an Advanced 3D Convolution Library. *PLoS ONE* **2011**, *6*, e24657. [[CrossRef](#)]
21. Abraham, M.; Murtola, T.; Schulz, R.; Páll, S.; Smith, J.; Hess, B.; Lindahl, E. GROMACS: High performance molecular simulations through multi-level parallelism from laptops to supercomputers. *SoftwareX* **2015**, *1–2*, 19–25. [[CrossRef](#)]
22. Huang, J.; Rauscher, S.; Nawrocki, G.; Ran, T.; Feig, M.; De Groot, B.L.; Grubmüller, H.; MacKerell, A.D., Jr. CHARMM36m: An improved force field for folded and intrinsically disordered proteins. *Nat. Methods* **2016**, *14*, 71–73. [[CrossRef](#)] [[PubMed](#)]
23. Marino, V.; Dell’Orco, D. Evolutionary-Conserved Allosteric Properties of Three Neuronal Calcium Sensor Proteins. *Front. Mol. Neurosci.* **2019**, *12*, 50. [[CrossRef](#)] [[PubMed](#)]
24. Svergun, D.; Barberato, C.; Koch, M.H.J. CRY SOL— a Program to Evaluate X-ray Solution Scattering of Biological Macromolecules from Atomic Coordinates. *J. Appl. Crystallogr.* **1995**, *28*, 768–773. [[CrossRef](#)]
25. Tria, G.; Mertens, H.D.T.; Kachala, M.; Svergun, D.I. Advanced ensemble modelling of flexible macromolecules using X-ray solution scattering. *IUCrJ* **2015**, *2*, 207–217. [[CrossRef](#)]
26. Chen, R.; Li, L.; Weng, Z. ZDOCK: An initial-stage protein-docking algorithm. *Proteins Struct. Funct. Bioinform.* **2003**, *52*, 80–87. [[CrossRef](#)]
27. Dell’Orco, D.; De Benedetti, P.G.; Fanelli, F. In silico screening of mutational effects on enzyme-protein inhibitor affinity: A docking-based approach. *BMC Struct. Biol.* **2007**, *7*, 37. [[CrossRef](#)]
28. Tiberti, M.; Invernizzi, G.; Lambrugh, M.; Inbar, Y.; Schreiber, G.; Papaleo, E. PyInteraph: A Framework for the Analysis of Interaction Networks in Structural Ensembles of Proteins. *J. Chem. Inf. Model.* **2014**, *54*, 1537–1551. [[CrossRef](#)]
29. Flinta, C.; Persson, B.; Jörnval, H.; Von Heijne, G. Sequence determinants of cytosolic N-terminal protein processing. *JBIC J. Biol. Inorg. Chem.* **1986**, *154*, 193–196. [[CrossRef](#)]
30. Marino, V.; Cortivo, G.D.; Oppici, E.; Maltese, P.E.; D’Esposito, F.; Manara, E.; Ziccardi, L.; Falsini, B.; Magli, A.; Bertelli, M.; et al. A novel p.(Glu111Val) missense mutation in GUC1A associated with cone-rod dystrophy leads to impaired calcium sensing and perturbed second messenger homeostasis in photoreceptors. *Hum. Mol. Genet.* **2018**, *27*, 4204–4217. [[CrossRef](#)]
31. Vivian, J.T.; Callis, P.R. Mechanisms of Tryptophan Fluorescence Shifts in Proteins. *Biophys. J.* **2001**, *80*, 2093–2109. [[CrossRef](#)]
32. Sokal, I.; Otto-Bruc, A.E.; Surgucheva, I.; Verlinde, C.L.; Wang, C.-K.; Baehr, W.; Palczewski, K. Conformational Changes in Guanylyl Cyclase-activating Protein 1 (GCAP1) and Its Tryptophan Mutants as a Function of Calcium Concentration. *J. Biol. Chem.* **1999**, *274*, 19829–19837. [[CrossRef](#)] [[PubMed](#)]
33. Orthaber, D.; Bergmann, A.; Glatter, O. SAXS experiments on absolute scale with Kratky systems using water as a secondary standard. *J. Appl. Crystallogr.* **2000**, *33*, 218–225. [[CrossRef](#)]
34. Svergun, D.I.; Semenyuk, A.V.; Feigin, L.A. Small-angle-scattering-data treatment by the regularization method. *Acta Crystallogr. Sect. A Found. Crystallogr.* **1988**, *44*, 244–250. [[CrossRef](#)]
35. Svergun, D.I. Restoring Low Resolution Structure of Biological Macromolecules from Solution Scattering Using Simulated Annealing. *Biophys. J.* **1999**, *76*, 2879–2886. [[CrossRef](#)]
36. Petoukhov, M.V.; Franke, D.; Shkumatov, A.V.; Tria, G.; Kikhney, A.G.; Gajda, M.; Gorba, C.; Mertens, H.D.T.; Konarev, P.V.; Svergun, D.I. New developments in the ATSAS program package for small-angle scattering data analysis. *J. Appl. Crystallogr.* **2012**, *45*, 342–350. [[CrossRef](#)]
37. Franke, D.; Svergun, D.I. DAMMIF, a program for rapid ab-initio shape determination in small-angle scattering. *J. Appl. Crystallogr.* **2009**, *42*, 342–346. [[CrossRef](#)]
38. Stephen, R.; Bereta, G.; Golczak, M.; Palczewski, K.; Sousa, M.C. Stabilizing Function for Myristoyl Group Revealed by the Crystal Structure of a Neuronal Calcium Sensor, Guanylate Cyclase-Activating Protein 1. *Structure* **2007**, *15*, 1392–1402. [[CrossRef](#)]

39. Krissinel, E.; Henrick, K. Inference of Macromolecular Assemblies from Crystalline State. *J. Mol. Biol.* **2007**, *372*, 774–797. [[CrossRef](#)]
40. Dindo, M.; Oppici, E.; Dell’Orco, D.; Montone, R.; Cellini, B. Correlation between the molecular effects of mutations at the dimer interface of alanine–glyoxylate aminotransferase leading to primary hyperoxaluria type I and the cellular response to vitamin B6. *J. Inherit. Metab. Dis.* **2017**, *41*, 263–275. [[CrossRef](#)]
41. Rudnicka-Nawrot, M.; Surgucheva, I.; Hulmes, J.D.; Haeseleer, F.; Sokal, I.; Crabb, J.W.; Baehr, A.W.; Palczewski, K. Changes in Biological Activity and Folding of Guanylate Cyclase-Activating Protein 1 as a Function of Calcium. *Biochemistry* **1998**, *37*, 248–257. [[CrossRef](#)] [[PubMed](#)]
42. Marino, V.; Borsatto, A.; Vocke, F.; Koch, K.-W.; Dell’Orco, D. CaF<sub>2</sub> nanoparticles as surface carriers of GCAP1, a calcium sensor protein involved in retinal dystrophies. *Nanoscale* **2017**, *9*, 11773–11784. [[CrossRef](#)] [[PubMed](#)]
43. Sakurai, K.; Oobatake, M.; Goto, Y. Salt-dependent monomer–dimer equilibrium of bovine  $\beta$ -lactoglobulin at pH 3. *Protein Sci.* **2008**, *10*, 2325–2335. [[CrossRef](#)] [[PubMed](#)]
44. Hwang, J.-Y.; Lange, C.; Helten, A.; Hoppner-Heitmann, D.; Duda, T.; Sharma, R.K.; Koch, K.-W. Regulatory modes of rod outer segment membrane guanylate cyclase differ in catalytic efficiency and Ca<sup>2+</sup>-sensitivity. *JBIC J. Biol. Inorg. Chem.* **2003**, *270*, 3814–3821. [[CrossRef](#)]



© 2020 by the authors. Licensee MDPI, Basel, Switzerland. This article is an open access article distributed under the terms and conditions of the Creative Commons Attribution (CC BY) license (<http://creativecommons.org/licenses/by/4.0/>).



Contents lists available at ScienceDirect

## BBA - Molecular Cell Research

journal homepage: [www.elsevier.com/locate/bbamcr](http://www.elsevier.com/locate/bbamcr)

# Missense mutations affecting $\text{Ca}^{2+}$ -coordination in GCAP1 lead to cone-rod dystrophies by altering protein structural and functional properties

Giuditta Dal Cortivo<sup>a,1</sup>, Valerio Marino<sup>a,1</sup>, Francesco Boni<sup>b,c</sup>, Mario Milani<sup>b,c</sup>, Daniele Dell'Orco<sup>a,\*</sup>

<sup>a</sup> Department of Neurosciences, Biomedicine and Movement Sciences, Section of Biological Chemistry, University of Verona, I-37134 Verona, Italy

<sup>b</sup> CNR-IBF, Istituto di Biofisica, Via Celoria 26, I-20133 Milano, Italy

<sup>c</sup> Dipartimento di Bioscienze, Università di Milano, Via Celoria 26, I-20133 Milano, Italy

## ABSTRACT

Guanylate cyclase activating protein 1 (GCAP1) is a neuronal calcium sensor (NCS) involved in the early biochemical steps underlying the phototransduction cascade. By switching from a  $\text{Ca}^{2+}$ -bound form in the dark to a  $\text{Mg}^{2+}$ -bound state following light activation of the cascade, GCAP1 triggers the activation of the retinal guanylate cyclase (GC), thus replenishing the levels of 3',5'-cyclic monophosphate (cGMP) necessary to re-open CNG channels. Here, we investigated the structural and functional effects of three missense mutations in GCAP1 associated with cone-rod dystrophy, which severely perturb the homeostasis of cGMP and  $\text{Ca}^{2+}$ . Substitutions affect residues directly involved in  $\text{Ca}^{2+}$  coordination in either EF3 (D100G) or EF4 (E155A and E155G)  $\text{Ca}^{2+}$  binding motifs. We found that all GCAP1 variants form relatively stable dimers showing decreased apparent affinity for  $\text{Ca}^{2+}$  and blocking the enzyme in a constitutively active state at physiological levels of  $\text{Ca}^{2+}$ . Interestingly, by corroborating spectroscopic experiments with molecular dynamics simulations we show that beside local structural effects, mutation of the bidentate glutamate in an EF-hand calcium binding motif can profoundly perturb the flexibility of the adjacent EF-hand as well, ultimately destabilizing the whole domain. Therefore, while  $\text{Ca}^{2+}$ -binding to GCAP1 per se occurs sequentially, allosteric effects may connect EF hand motifs, which appear to be essential for the integrity of the structural switch mechanism in GCAP1, and perhaps in other NCS proteins.

## 1. Introduction

Rod and cone cells in the retina initiate the visual process by responding to light absorption with a complex biochemical cascade known as phototransduction, which triggers the electrical response of the cell [1]. The dynamics of the cascade are regulated by a diversity of protein-protein, protein-nucleotide and protein-ion interactions [2] and the important interplay between the second messengers  $\text{Ca}^{2+}$  and guanosine 3',5'-cyclic monophosphate (cGMP) ensures a timely recovery of the cascade after the stimulus, as well as the proper kinetics of the reactions underlying light adaptation processes [3,4]. Under normal conditions, the complex formed by the membrane retinal guanylate cyclase 1 (GC1, also known as ROS-GC1 or GC-E [5]) and guanylate cyclase-activating proteins (GCAPs) permits a precise control of the cGMP synthesis. By detecting subtle changes in  $\text{Ca}^{2+}$  concentration and thereby adopting specific conformations, GCAPs control the activity of the target GC1, which is per se insensitive to  $\text{Ca}^{2+}$ . At high  $\text{Ca}^{2+}$  levels, corresponding to few hundred nanomolar in dark-adapted photoreceptors, GCAPs adopt a  $\text{Ca}^{2+}$ -loaded state that inhibits the activity of GC1. Following the light activation of the cascade, however, the concentration of  $\text{Ca}^{2+}$  in the outer segment drops down below 100 nanomolar and  $\text{Ca}^{2+}$  ions dissociate from GCAPs, inducing the switch to a

$\text{Mg}^{2+}$ -bound conformation of the protein [6–9]. This different conformational state is capable of stimulating GC1 activity, thus enhancing the synthesis of cGMP and contributing to the rapid restoring of dark-adapted conditions [3,10]. Of the three different GCAP isoforms expressed in human photoreceptors, so far only GCAP1 has been directly shown to regulate the activity of GC1 [11–13] while GCAP2 was found to be incapable of activating the enzyme [14], probably being involved in other physiological processes [15,16].

Cone (COD) and Cone-Rod (CORD) dystrophies are severe forms of inherited retinal dystrophies characterized by a variety of symptoms including central vision loss, impaired colour vision and photophobia [17–19]; to date more than 20 missense mutations in the gene encoding GCAP1 have been associated with autosomal dominant COD/CORD. Among these, four mutations, namely D100G, E111V and E155A/G affect residues directly involved in  $\text{Ca}^{2+}$  coordination belonging to the loops of either EF3 (D100G, E111V) or EF4 (E155A/G) (Fig. 1A), which constitute respectively the highest- and the lowest affinity site for  $\text{Ca}^{2+}$  binding [10,20,21]. Acidic residues occupy specific positions within an EF-hand motif to achieve the typical pentagonal bipyramid geometry necessary for  $\text{Ca}^{2+}$  coordination by oxygen atoms [22], therefore their substitution with other amino-acids may deeply impact structural and functional properties in  $\text{Ca}^{2+}$  binding proteins. The E111V GCAP1

\* Corresponding author.

E-mail address: [daniele.dellorco@univr.it](mailto:daniele.dellorco@univr.it) (D. Dell'Orco).

<sup>1</sup> These authors equally contributed to this work and should be considered joint first authors.

<https://doi.org/10.1016/j.bbamcr.2020.118794>

Received 11 June 2020; Received in revised form 1 July 2020; Accepted 3 July 2020

Available online 07 July 2020

0167-4889/ © 2020 Elsevier B.V. All rights reserved.

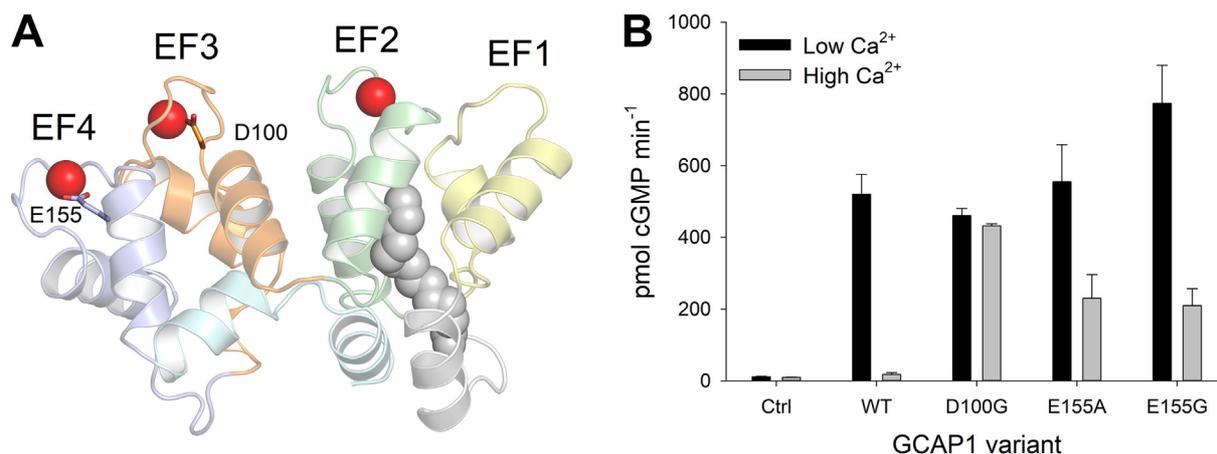


**Fig. 1.** A) The three-dimensional structure of the homology model of  $\text{Ca}^{2+}$ -loaded human GCAP1 is shown as cartoons, where EF-hand motifs EF1 to EF4 are colored in yellow, green, orange and blue, respectively. The N- and C-terminal helices are represented in cyan and grey, respectively,  $\text{Ca}^{2+}$ -ions are shown as red spheres, the myristoyl group is displayed in grey spheres, residues D100 and E155 are shown as sticks, with O atoms highlighted in red. B) Regulation of the Guanylate Cyclase 1 (GC1) by  $5 \mu\text{M}$  GCAP1 variants in the presence of  $\sim 30 \mu\text{M}$  (grey) or  $< 19 \text{ nM}$  (black)  $\text{Ca}^{2+}$ . Data are presented as average  $\pm$  standard deviation of 3 independent replicas, statistical analysis of the differences between variants/signaling states consisted of two-tailed *t*-tests with a significance of 0.05 (see Methods).

variant was recently discovered in a family afflicted by severe CORD and characterized in a thorough biochemical and biophysical study [12]. The D100G variant was found in three family members diagnosed with CORD associated with nystagmus, intraretinal pigment migration, loss of RPE and macular atrophy with a childhood onset, but the characterization has been limited to clinical and electrophysiological phenotypes [23]. The E155G variant was found to be associated with decreased visual acuity with early onset and central macular lesion with pigmentary changes compatible with CORD [24]. Fluorescence titrations and enzymatic assays showed that the apparent affinity of GCAP1-E155G for GC1 ( $\text{EC}_{50}$ ) was similar to that of the WT while the  $\text{IC}_{50}$ , i.e. the concentration of  $\text{Ca}^{2+}$  at which GC activity is half-maximal, was shifted to higher  $\text{Ca}^{2+}$  values ( $\sim 1 \mu\text{M}$ ) [24], consistent with a constitutive activation of the enzyme at physiological conditions. Finally, the E155A variant was discovered more recently in one of 130 unrelated Chinese probands, and the analysis was extended to four generations, leading to the diagnosis of CORD with poor vision, photophobia, myopia, defective colour perception and signs of morphological and functional macular alteration [25]. No biochemical analysis was performed of that variant so far.

In this work, we present a thorough characterization of the structural and dynamical properties of the three GCAP1 variants D100G, E155A and E155G affecting respectively the coordination of  $\text{Ca}^{2+}$  at the EF3 and EF4 loops (Fig. 1). We show that the effects of a single amino acid substitution can dramatically reflect on the correct switch between GC1-activating/inhibiting state of GCAP1. Even when the location of the substitution is the same, such as in the case of the E155A/G variants, the consequences on the protein dynamics can be very specific and propagate far from the initial site leading to different biochemical and colloidal properties that may be relevant for the phenotype observed in the disease.

## 2. Materials and methods

### 2.1. Protein expression and purification

Wild type human GCAP1 was heterologously expressed and purified as described [12]. The D100G and E155G GCAP1 variants were obtained by cloning the respective cDNA of human E6S-GCAP1 (Uniprot entry: P43080) with the point mutation corresponding to the desired substitution into a pET11a plasmid using *NdeI* and *NheI* as restriction sites (Genscript). The E6S point mutation was inserted in order to allow the myristoylation by N-myristoyl-transferase of *Saccharomyces*

*cerevisiae* (yNMT). The E155A point mutation was obtained by site directed mutagenesis using TCGCTGGAAGcATTTATTGAAGGC and CAG TTCACCATCGCCGTT as forward and reverse primers, respectively (Q5 Site-Directed Mutagenesis Kit, New England Biolabs Inc.).

Heterologous expression of GCAP1 variants was obtained co-transforming *E. coli* cells (BL21 DE3) with pET11a (GCAP1) and pBB131-yNMT plasmids. Selection was performed based on antibiotics resistance. GCAP1 variants were purified from inclusion bodies (IB) as previously described [26,27]. Briefly, after IB denaturation using 6 M guanidinium hydrochloride, proteins were renatured by dialysis and purified via Size Exclusion Chromatography (SEC) followed by Anionic Exchange Chromatography (AEC) [26,27]. Protein concentration was measured by Bradford assay [28] using a protein-specific calibration curve optimized following protein quantification by amino acid hydrolysis analysis (Alphalyze). GCAP1 samples used in  $\text{Ca}^{2+}$ -binding assays were washed against decalcified  $\text{NH}_4\text{CO}_3$  and lyophilized, while the remaining samples were washed in 20 mM TRIS pH 7.5, 150 mM KCl, 1 mM DTT, flash-frozen and kept at  $-80^\circ\text{C}$  until use.

### 2.2. Analytical size-exclusion chromatography

The apparent molecular weight of GCAP1 variants was estimated by analytical SEC. A Superose 12 10/300 column (GE Healthcare) was equilibrated with 20 mM TRIS pH 7.5, 150 mM KCl, 1 mM DTT and 500  $\mu\text{M}$  EGTA + 1 mM  $\text{Mg}^{2+}$  or 1 mM  $\text{Mg}^{2+}$  + 500  $\mu\text{M}$   $\text{Ca}^{2+}$ . Seventy to 90  $\mu\text{M}$  of each protein was centrifuged at 16,000 rpm (corresponding to 20,614  $\times g$ ) for 10 min at  $4^\circ\text{C}$ , ions were freshly added and samples were loaded onto the column connected to an FPLC system (AKTA). All the measurements were performed at room temperature. The elution profiles were followed monitoring the absorbance at 280 nm and the elution volumes ( $V_e$ ) were used to measure the distribution coefficient ( $K_d$ ) according to the equation:

$$K_d = (V_e - V_0)/(V_i - V_0)$$

in which  $V_i$  is the total column volume (25 mL) and  $V_0$  is the void volume (8 mL). The MW were determined using the calibration curve described in [29]. Each eluted peak was collected and immediately assayed by Dynamic light scattering.

### 2.3. Dynamic light scattering measurements (DLS)

DLS measurements were performed using a Zetasizer Nano-S (Malvern Instruments) with the same experimental settings as in [30]. The

hydrodynamic radius of the sample corresponding to each peak eluted during analytical gel filtration was estimated at 25 °C, at least 9 measurements were collected, each consisting of 12–15 repetitions. Polydispersion index and protein size are reported as mean  $\pm$  standard error of the mean (s.e.m).

Aggregation propensity was monitored in an independent experiment by measuring the evolution of the mean count rate (MCR) over 10 h of 30  $\mu$ M GCAP1 variant at 37 °C, in the presence of 500  $\mu$ M EGTA + 1 mM Mg<sup>2+</sup> or 1 mM Mg<sup>2+</sup> + 500  $\mu$ M Ca<sup>2+</sup>. Protein samples were filtered using a 20 nm cut-off filter (Anotop) and after 2 min equilibration, one measurement per minute was collected for at least 10 h, each consisting of 6 repetitions.

#### 2.4. Small angle X-ray scattering (SAXS)

One mg of the lyophilized D100G, E155G and E155A variants was resuspended in 20 mM TRIS, pH 7.5, 150 mM KCl, 5 mM MgCl<sub>2</sub>, 5 mM CaCl<sub>2</sub>, 1 mM DTT buffer. Samples were centrifuged at 14,000 rpm for ten minutes in a 5804 centrifuge (Eppendorf®) and the concentration of each protein was measured with a Nanodrop spectrophotometer following the theoretical absorption coefficient at 280 nm, resulting in 0.7 mM, 0.9 mM and 1.1 mM, respectively.

Before SAXS data collection, four serial dilutions of each variant were prepared using the same buffer, and the concentrations measured after 10 min centrifugation at 14,000 rpm. Forty microliters of each sample were loaded in a 96 multi-well plate and incubated at room temperature for about three hours before data collection. During this time, we noticed a tendency to precipitate for the E155G mutant and therefore all the concentrations reported for this sample must be considered as approximate.

SAXS measurements were performed at Diamond Light Source synchrotron (Oxford) in automatic batch mode. Data were collected at B21 beamline operating at 12.4 KeV with a flux of about 1012 photons/s at 10 °C, equipped with a detector Eiger 4 M. 1d SAXS data were averaged and the buffer subtracted using the program *primus* [31]. Data analysis was done using different programs of the *ATSAS package* [32].

SAXS experiments were performed with WT GCAP1 as well; results of such experiments coupled with analytical SEC are presented in detail in another work (manuscript in preparation).

#### 2.5. Guanylate cyclase assay (GC assay)

To test whether amino acid substitutions in GCAP1 affected the regulation of GC1 activity, specific enzymatic assays were performed to monitor the induced synthesis of cGMP. A permanent cell line expressing human GC1 was cultured in DMEM medium supplemented with fetal bovine serum (10% v/v), penicillin (100 units/mL), streptomycin (100  $\mu$ g/mL) and geneticin (500  $\mu$ g/mL), as described in [12,33]. Cells were harvested at 90% confluence, washed with sterile PBS and stored at –80 °C until use. Enzymatic assays were performed on isolated membranes obtained by suspending cells in lysis buffer (10 mM HEPES pH 7.4, 1 mM DTT, protease inhibitor cocktail 1X) and incubated for 20 min on ice. Fifteen up-and-down cycles with a 1 mL syringe on ice were performed and cells were centrifuged for 20 min at 10,000 rpm. The resulting pellets were suspended in 50 mM HEPES pH 7.4, 50 mM KCl, 20 mM NaCl, 1 mM DTT and used for enzymatic activity assays. Maximal and minimal enzymatic activities were assayed incubating 5  $\mu$ M of each GCAP1 variant in the presence of 2 mM K<sub>2</sub>H<sub>2</sub>EGTA or K<sub>2</sub>CaEGTA to obtain < 19 nM (GC1-activating) or ~30  $\mu$ M free Ca<sup>2+</sup> (GC1-inhibiting) in the presence of 1 mM Mg<sup>2+</sup>. The cGMP produced during the assay was quantified by reverse phase chromatography using a monolithic column (Chromolith RP18, Sigma Aldrich). Data are reported as pmol of cGMP produced per minute.

#### 2.6. SDS-PAGE mobility assay

A gel shift assay was performed to assess cation-induced changes in electrophoretic mobility of GCAP1 variants under denaturing conditions [34]. Twenty micromolar of each GCAP1 variant was incubated in the presence of 2 mM EDTA, 1 mM EGTA + 1.1 mM Mg<sup>2+</sup> or 1 mM Mg<sup>2+</sup> + 1 mM Ca<sup>2+</sup> using 20 mM TRIS pH 7.5, 150 mM KCl, 1 mM DTT as working buffer. After 5 min incubation at 25 °C, samples were boiled, loaded onto a 15% polyacrylamide gel and Coomassie blue-stained after each electrophoretic run (200 V, 40–45 min).

#### 2.7. Determination of Ca<sup>2+</sup> binding constants by a chromophoric chelator assay

To assess the Ca<sup>2+</sup>-binding capability of GCAP1 mutants, competition assays were performed in the presence of the chromophoric chelator 5,5'-Br<sub>2</sub>-BAPTA as described in detail in [6,20,35]. Briefly, lyophilized proteins were dissolved in decalcified buffer (20 mM TRIS pH 7.5, 150 mM KCl, 1 mM Mg<sup>2+</sup>, 1 mM DTT; initial [Ca<sup>2+</sup>]: 0.7–1.3  $\mu$ M) in the presence of 24–25  $\mu$ M 5,5'-Br<sub>2</sub>-BAPTA. Absorbance at 263 nm was followed upon sequential additions of 3  $\mu$ M Ca<sup>2+</sup> at room temperature until no change in absorbance was detected. Titrations were performed in triplicate. Data were fitted to theoretical models using CaLigand [36] software to estimate the macroscopic Ca<sup>2+</sup>-binding constant (log K<sub>i</sub>) of each binding site. Macroscopic apparent affinity values (K<sub>d</sub><sup>app</sup>) were extracted from saturation curves obtained for each independent titration from the best fitting curves. Data fitting was performed using a model with three Ca<sup>2+</sup>-binding sites (some of the obtained values were considered unreliable due to intrinsic limitations, see Table 1). Presented data were normalized as follow:

$$Ca^{2+}_{norm} = \frac{[Ca^{2+}]}{[Q] + 3 * [P]}$$

$$y_{norm} = \frac{A_{263} - A_{min}}{A_{max} - A_{min}}$$

where A<sub>263</sub> is the absorbance at 263 nm, [Q] and [P] are the concentration of 5,5'-Br<sub>2</sub>-BAPTA and GCAP1 variant, respectively, measured at the end of each repetition by Bradford assay.

#### 2.8. Circular dichroism spectroscopy and thermal denaturation studies

CD spectra were collected as detailed in [12] using a Jasco J-1500 spectropolarimeter equipped with a Peltier cell holder thermostated at 37 °C. Near UV spectra were recorded between 250 and 320 nm using a 1 cm quartz cuvette with 30  $\mu$ M of each GCAP1 variant in the presence of 500  $\mu$ M EGTA and after sequential additions of 1 mM Mg<sup>2+</sup> and 1 mM Ca<sup>2+</sup>. Far UV spectra were collected between 200 and 250 nm using a 0.1 cm quartz cuvette with 12  $\mu$ M of each GCAP1 variant in the

**Table 1**  
Ca<sup>2+</sup>-binding constants and functional analysis.

	log K <sub>1</sub> <sup>a</sup>	log K <sub>2</sub> <sup>a</sup>	log K <sub>3</sub> <sup>a</sup>	K <sub>d</sub> <sup>app</sup> (nM) <sup>b</sup>	X-fold <sup>c</sup>
WT <sup>d</sup>	7.2 $\pm$ 0.2	4.8 $\pm$ 1.4	4.0 $\pm$ 0.3	63 $\pm$ 24	28.7 $\pm$ 9.3
D100G	5.99 $\pm$ 0.08	2.0 $\pm$ 1.5	6.2 $\pm$ 1.4	1034 $\pm$ 178	0.06 $\pm$ 0.9
E155A	6.3 $\pm$ 0.5	2.5 $\pm$ 0.6	6.2 $\pm$ 0.8	753 $\pm$ 535	1.41 $\pm$ 0.9
E155G	6.3 $\pm$ 0.3	3.8 $\pm$ 1.0	4.4 $\pm$ 0.8	550 $\pm$ 412	2.68 $\pm$ 0.9

<sup>a</sup> Decimal logarithm of the macroscopic Ca<sup>2+</sup>-binding constants after data fitting to a three independent binding sites model obtained by CaLigand [34]. Underlined values are considered poorly reliable being significantly below that of the chelator (5.6).

<sup>b</sup> Apparent K<sub>d</sub> obtained by fitting the saturation curve to a 3-parameter Hill sigmoid. (average  $\pm$  standard deviation, n = 3).

<sup>c</sup> X-fold is calculated as (GC<sub>low, Ca</sub> – GC<sub>high, Ca</sub>) / (GC<sub>high, Ca</sub>)  $\pm$  propagated error.

<sup>d</sup> Raw data are taken from [12].

presence of 300  $\mu\text{M}$  EGTA and after sequential additions of 1 mM  $\text{Mg}^{2+}$  and 600  $\mu\text{M}$   $\text{Ca}^{2+}$ . The spectrum of the solvent (20 mM TRIS pH 7.5, 150 mM KCl, 1 mM DTT) was considered as blank and subtracted. Each spectrum was the mean of 5 accumulations collected setting the scan rate at 50 nm/min, 1 nm bandwidth, 4 s time response.

Thermal denaturation profiles were recorded in the same conditions used for far UV measurements, monitoring the ellipticity at 222 nm in a temperature range between 20 °C and 96 °C (scan rate 90 °C/h). Data was fitted to the following function:

$$\theta_{222}(T) = \frac{(b_n + k_n T) + (b_u + k_u T) \exp[-\Delta G_{nu}(T)]}{1 + \exp\left[\frac{-\Delta G_{nu}(T)}{RT}\right]}$$

where  $n$  and  $u$  refer to the native and unfolded states,  $b$  is the baseline,  $T$  is the temperature,  $k$  is the slope of each state and  $\Delta G_{nu}$  in the Gibbs free energy for folded-to-unfolded transition, which can be expressed in terms of change in enthalpy and heat capacity upon denaturation at constant pressure as follows:

$$\Delta G_{nu}(T) = -\left(\Delta H\left(1 - \frac{T}{T_m}\right)\right) + \Delta C_p\left(T - T_m - T \ln \frac{T}{T_m}\right)$$

## 2.9. Hydrophobicity analysis by 8-Anilino-naphthalene-1-sulfonic acid fluorescence assays

To follow the changes in hydrophobicity of each GCAP1 variant upon cations coordination, 8-Anilino-naphthalene-1-sulfonic acid (ANS) emission spectra were collected using a Jasco FP-750 spectrofluorometer. Two micromolar of each GCAP1 variant were incubated at 37 °C for 5 min in the dark with 30  $\mu\text{M}$  ANS in the presence of 500  $\mu\text{M}$  EDTA and after sequential additions of 1.5 mM  $\text{Mg}^{2+}$  and 1 mM  $\text{Ca}^{2+}$ . Fluorescence emission was monitored between 400 and 650 nm following excitation at 380 nm, excitation and emission bandwidths were fixed to 5 nm. The spectrum of ANS without protein was considered as the reference (Table 2), while the spectrum of the sole buffer (20 mM TRIS pH 7.5, 150 mM KCl, 1 mM DTT, 0.1% DMSO) was considered as a blank and subtracted. Each spectrum shown represents the average of three replicas.

## 2.10. Molecular dynamics simulations

The three-dimensional structure of myristoylated human GCAP1 was obtained by homology modelling based on the  $\text{Ca}^{2+}$ -loaded

chicken GCAP1 template [37] as previously detailed [20]. Mutations D100G, E155A and E155G were introduced in human GCAP1 structure using the "Mutate Residue" tool built in Maestro v. 12.2.012 (Schrodinger) suite by selecting the highest-scored rotamer proposed. Molecular Dynamics (MD) simulations were run on GROMACS v. 2016.1 simulation package [38] using CHARMM36m [39] all-atom forcefield. Parameters for myristoylated Gly were manually introduced and are available upon request. Each variant was subjected to energy minimization and a two-steps equilibration procedure followed by  $5 \times 200$  ns production phase as explained in [40,41]. The Root-Mean Square Fluctuation (RMSF) of Ca and the distances between Ca of the  $\text{Ca}^{2+}$ -coordinating residues of EF3 (D/G100, D102, N104, C106, N108, E111) and EF4 (D144, N146, D148, E150, S152, E/G/A155) were calculated using *gmx rmsf* and *gmx distance* provided by GROMACS package.

## 2.11. Statistical analysis

Data referring to GC1 regulation and hydrodynamic diameter estimation by DLS were subjected to two-tailed  $t$ -tests (p-value = 0.05) to assess the statistical significance of the differences between the observables, where the null hypothesis consisted in no differences between the mean of the measurables.

## 3. Results

### 3.1. D100G and E155A/G GCAP1 variants are unable to completely inhibit GC1

To test the capability of GCAP1 variants to regulate the target enzyme, enzymatic assays were performed (Fig. 1B) by incubating 5  $\mu\text{M}$  of each mutant with GC1-containing membranes in the presence of low (black bars) and high (grey bars)  $[\text{Ca}^{2+}]$ , thus mimicking the conditions of light vs. dark-adapted photoreceptors, respectively. None of the variants showed compromised ability to activate GC1 at low  $\text{Ca}^{2+}$ . Indeed, the activation profiles of D100G and E155A GCAP1 were very similar to that of the WT (two-tailed  $t$ -test, p-values 0.15 and 0.63 respectively), with a rate of cGMP synthesis of approximately 500–550 pmol cGMP/min, while a 1.5-fold increased activation (780 pmol/min, two-tailed  $t$ -test, p-value 0.02) was observed for E155G GCAP1. On the other hand, all three variants failed to induce complete inhibition of GC1 at high  $\text{Ca}^{2+}$  concentration (Fig. 1B, (two-tailed  $t$ -test, p-value < 0.005). To better quantify the dysregulation of the target, the

**Table 2**  
Shape overview and hydrophobic analysis.

		ANS fluorescence		CD spectra analysis			
		$\Delta\lambda^a$	$I/I_{\text{max}}^b$	$\theta_{222}/\theta_{208}$	$\Delta\theta/\theta$ (%) <sup>c</sup>	$T_m$ (°C) <sup>d</sup>	Unfolding (%) <sup>e</sup>
WT	Apo	34.3 ± 3.5	1.00 ± 0.03	0.90	–	54.1 <sup>f</sup>	24.6 <sup>f</sup>
	+Mg <sup>2+</sup>	27 ± 2	0.74 ± 0.03	0.91	2.8	58.0 <sup>f</sup>	30.8 <sup>f</sup>
	+Ca <sup>2+</sup>	26 ± 2	0.70 ± 0.01	0.95	7.7	> 96 <sup>f</sup>	30.4 <sup>f</sup>
D100G	Apo	32.0 ± 2.7	1.00 ± 0.01	0.91	–	52.8	28.0
	+Mg <sup>2+</sup>	32.0 ± 2.7	0.88 ± 0.02	0.92	–0.6	57.2	27.7
	+Ca <sup>2+</sup>	29.3 ± 2.3	0.83 ± 0.02	0.90	0.2	81.5	33.0
E155A	Apo	36.3 ± 2.3	1.00 ± 0.02	0.92	–	53.5	27.6
	+Mg <sup>2+</sup>	34.3 ± 2.3	0.81 ± 0.02	0.89	–1.3	55.9	29.4
	+Ca <sup>2+</sup>	34.3 ± 2.3	0.79 ± 0.03	0.90	–1.1	79	46.3
E155G	Apo	33.7 ± 2.3	1.00 ± 0.01	0.88	–	50.6	24.1
	+Mg <sup>2+</sup>	30.0 ± 2.7	0.79 ± 0.02	0.89	–6.7	50.1	30.1
	+Ca <sup>2+</sup>	23.7 ± 2.3	0.63 ± 0.02	0.90	–0.2	76.3	45.9

<sup>a</sup>  $\Delta\lambda = (\lambda_{\text{ANS}}^{\text{max}} - \lambda_i^{\text{max}}) \pm (\sigma_{\text{ANS}} + \sigma_i)$ .

<sup>b</sup>  $I/I_{\text{max}} = (\text{Int}_i / \text{Int}_{\text{Max}}) \pm [\text{Int}_i / \text{Int}_{\text{Max}} * (\sigma_i / \text{Int}_i + \sigma_{\text{Max}} / \text{Int}_{\text{Max}})]$ .

<sup>c</sup> Calculated as  $(\theta_{222}^{\text{ion}} - \theta_{222}^{\text{EGTA}}) / \theta_{222}^{\text{EGTA}}$ .

<sup>d</sup> Melting temperature estimated by fitting ellipticity at 222 nm as described in Methods.

<sup>e</sup> Percentage of unfolding calculated as  $(\theta_{222}^{96} - \theta_{222}^{20}) / \theta_{222}^{20}$ .

<sup>f</sup> Raw data are taken from [12].

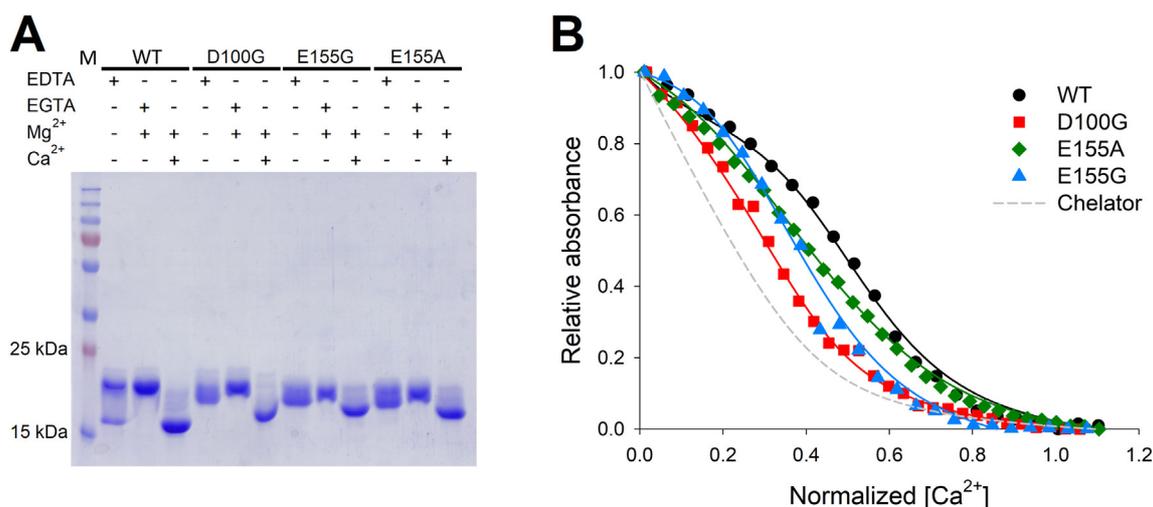


**Fig. 2.** A) Electrophoretic mobility shift of 20  $\mu\text{M}$  GCAP1 variants in the presence of 2 mM EDTA, 1 mM EGTA and 1.1 mM  $\text{Mg}^{2+}$  or 1 mM  $\text{Mg}^{2+}$  and 1 mM  $\text{Ca}^{2+}$ . B) Normalized  $\text{Ca}^{2+}$  titrations of GCAP1 variants in competition with the chromophoric chelator 5,5'-Br<sub>2</sub>-BAPTA in the presence of 1 mM  $\text{Mg}^{2+}$ . Experimental points for WT (black circles), D100G (red squares), E155G (green diamonds) and E155A (blue triangles) are displayed together with the respective optimal curve (solid lines) calculated by computer fitting and the theoretical curve representing a titration of the Chelator alone (grey dashed line). Estimation of the binding constants is reported in Table 1, details about data normalization are described in Methods section.

capability of each GCAP1 variant to activate GC1 at low  $\text{Ca}^{2+}$  as compared to its induced inhibition/inactivation at high  $\text{Ca}^{2+}$  was quantified by the X-fold activation values reported in Table 1. The X-fold value of the D100G variant was  $\sim 500$  times lower than that of WT GCAP1 (0.06 vs 28.7), thus highlighting a complete loss of GC1 switch-off capability, while 20 times (1.41) and 10 times (2.68) lower X-fold values were observed for E155A and E155G variants.

### 3.2. CORD-associated GCAP1 variants present decreased affinity for $\text{Ca}^{2+}$

To test whether the inefficient inhibition of GC1 was associated with perturbed  $\text{Ca}^{2+}$  sensing of GCAP1 variants, we measured their affinity for  $\text{Ca}^{2+}$  by two independent methods, namely SDS-PAGE gel-shift and a competition assay with the chelator 5-5'-Br<sub>2</sub>-BAPTA (Fig. 2). SDS-PAGE gel-shift is a low-resolution technique based on the different electrophoretic mobility shown upon  $\text{Ca}^{2+}$  binding by calcium sensor proteins presenting high affinity for  $\text{Ca}^{2+}$ . In the presence of  $\text{Ca}^{2+}$ , such sensors present higher electrophoretic mobility, most probably due to the residual structure retained in spite of the high temperature and the detergent. The method can thus provide a rough information as to the affinity of the protein for  $\text{Ca}^{2+}$ , since smaller gel shifts often correlate with lower affinity [6,42,43]. Fig. 2A shows the comparison between WT GCAP1 and the CORD-related mutants in the absence of ions (EDTA), in the presence of sole  $\text{Mg}^{2+}$  (EGTA +  $\text{Mg}^{2+}$ ) and in the presence of saturating cations ( $\text{Mg}^{2+}$  +  $\text{Ca}^{2+}$ ). In spite of the excess of EDTA, WT GCAP1 (lane 2) showed a smeared profile with two bands approximately around 22 kDa and 17 kDa, indicative of the partially retained capability to bind  $\text{Ca}^{2+}$  [12,44]. The addition of saturating  $\text{Mg}^{2+}$  led to the formation of a compact band at the theoretical MW of approximately 23 kDa; this shifted to lower MW (17 kDa) after the addition of saturating  $\text{Ca}^{2+}$ , with the appearance of a faint smear above the main band likely due to the co-presence of different  $\text{Ca}^{2+}$ -bound states. None of the three CORD-variants showed a similarly broad gel shift upon addition of cations and changes in mobility were much smaller, indicative of a reduced affinity for  $\text{Ca}^{2+}$  for E155A/G and D100G GCAP1 (Fig. 2A).

$\text{Ca}^{2+}$  titrations in the co-presence of the chromophoric chelator 5-5'-Br<sub>2</sub> BAPTA were performed to measure the affinity for  $\text{Ca}^{2+}$  of each GCAP1 variant (Fig. 2B and Table 1). Original data referring to WT GCAP1 are from ref. [12], but in the present work a 3  $\text{Ca}^{2+}$ -binding sites model was used for the fitting procedure (see Methods). The

titration profile clearly indicated overall stronger propensity to bind  $\text{Ca}^{2+}$  for WT GCAP1 (black circles), as indicated by the lower slope of the curve in the first phase, which represents a higher affinity of  $\text{Ca}^{2+}$  for the protein compared to the chelator (grey dashed line). Titration curves for all three mutants, though to different extent, showed a more pronounced slope in the first phase of the titration, with D100G (red squares) presenting the steepest decrease in absorbance, thus suggesting little competition with the chelator hence, comparatively, the lowest affinity for  $\text{Ca}^{2+}$ . E155A (green diamonds) and E155G (blue triangles) showed titration curves in between those of the WT and D100G, thus suggesting an intermediate apparent affinity for  $\text{Ca}^{2+}$ . Data fitting to a 3 sequential binding sites model returned values for the single macroscopic constants to each binding site ( $\log K_i$ ) reported in Table 1. Constants whose values were found to be significantly low (below 4.0) were considered not reliable for the competition assay, in light of the comparison with the macroscopic binding constant of the chelator  $\log K_Q$  (5.6). Binding of  $\text{Ca}^{2+}$  to the highest affinity site in CORD-variants occurred in each case with a  $\sim 10$ -fold lower affinity compared to WT GCAP1 (compare  $\log K_1$  values). A dramatic loss of affinity was observed especially for the second binding site, while binding to the third site for E155A and D100G appeared to be favored compared to the WT, due to higher  $\log K_3$  values (Table 1). Considering the low accuracy of some of the obtained parameters due to intrinsic experimental limitations, a rigorous comparison between the macroscopic binding constant was de facto unfeasible and we rather focused the analysis on the apparent affinity values ( $K_d^{\text{app}}$ ) obtained by the saturation curves of each GCAP1 variant upon titration with  $\text{Ca}^{2+}$  (Table 1). While WT GCAP1 showed an apparent affinity for  $\text{Ca}^{2+}$  ( $\sim 60$  nM) fully in line with its physiological function in photoreceptors, all other variants displayed  $K_d^{\text{app}}$  values shifted to high nM (E155A/G,  $\sim 550$ – $750$  nM) or low  $\mu\text{M}$  ( $\sim 1$   $\mu\text{M}$ , D100G) values (Table 1) thus indicative of compromised  $\text{Ca}^{2+}$  sensing capability under physiological conditions. It should be noted that in no case was cooperativity of  $\text{Ca}^{2+}$  binding detected for all tested variants, as proved by the slope of the titration curves (Fig. 1B) and by the Hill coefficient of the saturation curves, ranging from 1.00 to 1.05 in all cases.

### 3.3. Point mutations affect structure, hydrophobicity and thermal stability of CORD-GCAP1 variants

CD spectra were collected both in the far (200–250 nm) and near UV

(250–320 nm) regions to monitor changes in secondary and tertiary structure, respectively, upon addition of cations. Far UV spectra (Fig. S1) confirmed that none of the amino acid substitutions perturbed protein secondary structure since all variants displayed the typical spectrum of all  $\alpha$ -helix proteins, characterized by the two minima at 208 and 222 nm. However, small but significant spectral variations could be appreciated, which were quantified by the shape descriptor  $\theta_{222}/\theta_{208}$  and the  $\Delta\theta/\theta$  ratio (Table 2). Coordination of  $\text{Ca}^{2+}$  has been shown to reflect into increased ellipticity signal in the far UV region and into more compact, tightly interacting helices in WT GCAP1 [12,20], which resulted in slight increases of both  $\theta_{222}/\theta_{208}$  and  $\Delta\theta/\theta$  values upon  $\text{Ca}^{2+}$  binding ( $\theta_{222}/\theta_{208} = 0.90$  vs.  $0.95$ ,  $\Delta\theta/\theta = 7.7\%$ ; Table 2). Conversely, the CORD-variants here described showed substantially overlapped spectra in all the tested conditions (Fig. S1), with almost unchanged  $\theta_{222}/\theta_{208}$  values and  $\Delta\theta/\theta$  ratios not exceeding 1%, except for a  $\sim 7\%$  signal decrease observed for E155G upon binding of  $\text{Mg}^{2+}$  (Table 2). In summary, the typical spectroscopic changes previously observed for WT and other GCAP1 variants [20,44], which accompany variations in protein compactness and helix-packing following  $\text{Ca}^{2+}$  binding, were not observed in the present study for mutants affecting  $\text{Ca}^{2+}$ -coordination.

Monitoring the CD signal in the near UV region permits the assessment of structural rearrangements in the microenvironment of the aromatic amino acids upon cation binding, thus allowing insights into protein tertiary structure changes (Fig. 3A–C). While the point mutations affecting  $\text{Ca}^{2+}$  coordination did not alter significantly the overall fold of all GCAP1 variants, a closer look at the spectra revealed subtle changes. Indeed, by comparing the spectra of apo-E155A and apo-E155G (Fig. 3B–C, black solid lines) with  $\text{Mg}^{2+}$ -E155A and  $\text{Mg}^{2+}$ -E155G (Fig. 3B–C, short-dashed blue lines) a significant increase in ellipticity was observed, which was neither observed for WT [12] nor D100G GCAP1 (Fig. 3A). The most significant variation in ellipticity was displayed by all GCAP1 variants when saturating  $\text{Ca}^{2+}$  was added

(long-dashed red lines). While this clearly demonstrates that all variants were capable of binding  $\text{Ca}^{2+}$  thereby changing their conformation, spectral changes were more apparent for E155A GCAP1, both at the phenylalanine band that reached very low ellipticity values, and especially for the tyrosine and tryptophan bands, which were completely negative in this case (Fig. 3B). Minor spectral changes were observed for  $\text{Ca}^{2+}$ -D100G and E155G with respect to the previously characterized  $\text{Ca}^{2+}$ -WT, except for a slight increase in the intensity of the tyrosine and tryptophan bands for E155G.

To assess whether these small but significant structural changes might be accompanied by altered protein hydrophobicity, ANS was used as a convenient probe as its fluorescent properties change upon binding to hydrophobic regions on the protein surface. As already seen for WT and E111V GCAP1 [12], all the mutants were more hydrophobic in the absence of ions (Fig. S2, black solid lines), showing a 32–36 nm blue-shift (Table 2) and increased intensity of fluorescence emission. The addition of 1 mM  $\text{Mg}^{2+}$  (short-dashed blue lines) led to different effects: while no shift in the wavelength of maximum fluorescence ( $\Delta\lambda$ ) with respect to the apo protein was detected for D100G (Fig. S2 left, Table 2), minor red-shifts were observed for E155A and E155G (2 and 3 nm, respectively). The addition of saturating  $\text{Ca}^{2+}$  (long-dashed lines) completed the structural transition, with a more prominent effect for E155G in terms of red-shift (Fig. S2, right  $\Delta\lambda = 10$  nm red-shift) than for D100G ( $\Delta\lambda = 3$  nm red-shift) or E155A (Fig. S2, middle), whose  $\lambda_{\text{max}}$  remained unchanged with respect to the  $\text{Mg}^{2+}$  bound form (2 nm red-shift). Interestingly, the replacement of E155 by A or G exerted different effects in terms of  $I/I_{\text{max}}$  variations, since E155A was characterized by an overall stronger fluorescence emission compared to both E155G and D100G. This, together with the fact that the  $I/I_{\text{max}}$  values for the  $\text{Ca}^{2+}$ -bound form indicate much stronger quenching compared to the  $\text{Mg}^{2+}$ -bound state (Table 2), suggest that hydrophobic residues are somehow more buried in E155A under GC1-activating conditions ( $\text{Mg}^{2+}$ ) compared to the inhibiting state ( $\text{Ca}^{2+}$ ), which

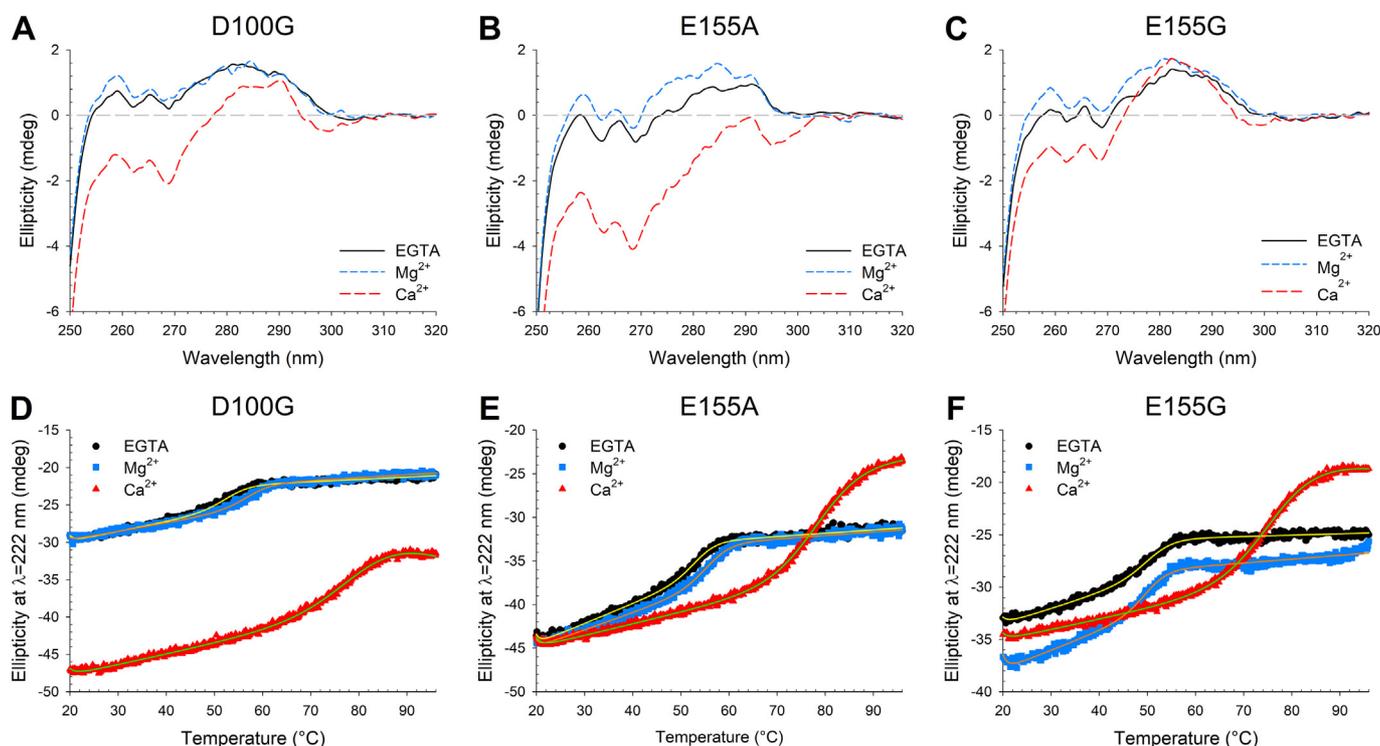


**Fig. 3.** Near UV CD spectra of 30  $\mu\text{M}$  GCAP1 variants A) D100G, B) E155A and C) E155G in the presence of 500  $\mu\text{M}$  EGTA (black, solid line) and after sequential additions of 1 mM  $\text{Mg}^{2+}$  (blue, short-dashed line) and 1 mM  $\text{Ca}^{2+}$  (red, medium-dashed line). Thermal denaturation profiles of 12  $\mu\text{M}$  GCAP1 variants D) D100G, E) E155A and F) E155G in the presence of 300  $\mu\text{M}$  EGTA (black circles), 300  $\mu\text{M}$  EGTA and 1 mM  $\text{Mg}^{2+}$  (blue squares) or 1 mM  $\text{Mg}^{2+}$  and 600  $\mu\text{M}$   $\text{Ca}^{2+}$  (red triangles). Data fitting to the thermodynamic function described in Methods section is shown in yellow, orange and green, respectively; estimated unfolding percentages and melting temperatures are reported in Table 2.

evidently exposes part of the hydrophobic region to the solvent.

In order to assess protein structural stability, thermal denaturation profiles were collected for each GCAP1 variant in the 20–96 °C range by monitoring the ellipticity signal at 222 nm (Fig. 3D–F). A two-state transition function was used for fitting the data to obtain the transition temperature  $T_m$  reported in Table 2 (original data for WT GCAP1 are from ref. [12], but in the present study data were fitted to a different function described in the Methods). The apo-form of all the CORD variants tested were 1 to 4 °C less stable compared to the WT GCAP1. Addition of  $Mg^{2+}$  similarly stabilized both WT and D100G ( $\Delta T_m \sim 4$  °C), while a slightly lower effect ( $\Delta T_m \sim 2$  °C) was observed for E155A. Interestingly, no effect on the  $T_m$  was observed for E155G (Fig. 3F, Table 2). Addition of saturating  $Ca^{2+}$  stabilized all GCAP1 variants (Fig. 3, red triangles), however CORD-GCAP1 variants showed a full transition with  $T_m$  values in the 76–82 °C range, while the transition for WT GCAP1 was incomplete ( $T_m > 96$  °C; see ref. [12]), indicative of significantly higher  $Ca^{2+}$ -induced structure stabilization due to the unperturbed  $Ca^{2+}$  coordination. Although no GCAP1 variant underwent complete thermal denaturation resulting in complete loss of secondary structure, as assessed by the relatively high residual ellipticity at 96 °C, the same heating procedure differently affected the variants in terms of relative unfolding (Table 2). Interestingly, the percentage of unfolding in apo- conditions (24–28%) and in the presence of  $Mg^{2+}$  (28–31%) was similar for all variants, but the addition of saturating  $Ca^{2+}$  led to a major loss of secondary structure when the mutation was localized in EF4 (46%, E155G and E155A) compared to EF3 (33%, D100G).

### 3.4. Oligomeric organization and aggregation propensity of GCAP1 variants

WT GCAP1 forms dimers under conditions mimicking the physiological ones [12,45]. To assess whether the mutations under investigation led to changes in GCAP1 oligomeric state, we performed analytical SEC followed by DLS of the eluted peaks. This allowed us to estimate the apparent MW and the hydrodynamic radius of each

**Table 3**

Analytical size exclusion chromatography and DLS data.

		MW (kDa)	d (nm) <sup>a</sup> [n] <sup>b</sup>	PdI <sup>c</sup>
WT	$Mg^{2+}$	45.9	6.35 ± 0.07 [27]	0.342 ± 0.02
	$Mg^{2+}$ + $Ca^{2+}$	47.8	6.85 ± 0.17 [20]	0.306 ± 0.02
D100G	$Mg^{2+}$	44.9	6.86 ± 0.11 [30]	0.434 ± 0.02
	$Mg^{2+}$ + $Ca^{2+}$	47.8	7.05 ± 0.24 [9]	0.272 ± 0.03
E155A	$Mg^{2+}$	44.2	7.80 ± 0.08 [32]	0.311 ± 0.02
	$Mg^{2+}$ + $Ca^{2+}$	42.8	8.80 ± 0.10 [37]	0.295 ± 0.02
E155G	$Mg^{2+}$	44.3	6.35 ± 0.07 [52]	0.381 ± 0.01
	$Mg^{2+}$ + $Ca^{2+}$	44.8	7.15 ± 0.18 [19]	0.217 ± 0.02

<sup>a</sup> Average ± s.e.m. as assessed from the intensity of scattered light.

<sup>b</sup> Number of measurements.

<sup>c</sup> Polydispersity index ± s.e.m.

variant, respectively. Analytical SEC profiles (Fig. 4A–C) highlighted the presence of one prevailing peak for all the variants in all the tested conditions (Fig. 4), with only small differences observed when elution occurred in the presence of the sole  $Mg^{2+}$  or both  $Mg^{2+}$  and  $Ca^{2+}$ . Based on a calibration line built with globular proteins of known molecular mass, we concluded that all GCAP1 mutants displayed an apparent MW (43–48 kDa) compatible with a dimeric protein under the tested conditions (Table 3). DLS of the samples eluted from analytical SEC revealed monodispersed distributions of intensity peaks compatible with a single prevailing oligomeric state. Quantitative analysis (Table 3) showed for all variants an average hydrodynamic size around 7 nm, compatible with a dimeric protein, which increased in size when switching from the  $Mg^{2+}$ -bound to the  $Ca^{2+}$ -bound state. Interestingly, while the change in hydrodynamic diameter of both E155A and E155G GCAP1 (0.8–1 nm, p-value <  $10^{-6}$ ) significantly exceeded that of the WT (0.6 nm, p-value =  $2 \cdot 10^{-4}$ ), D100G GCAP1 did not display any significant increase in size upon  $Ca^{2+}$  binding within the experimental error (p-value = 0.46). Moreover, it is noteworthy that the hydrodynamic diameter of E155A was significantly larger compared to any

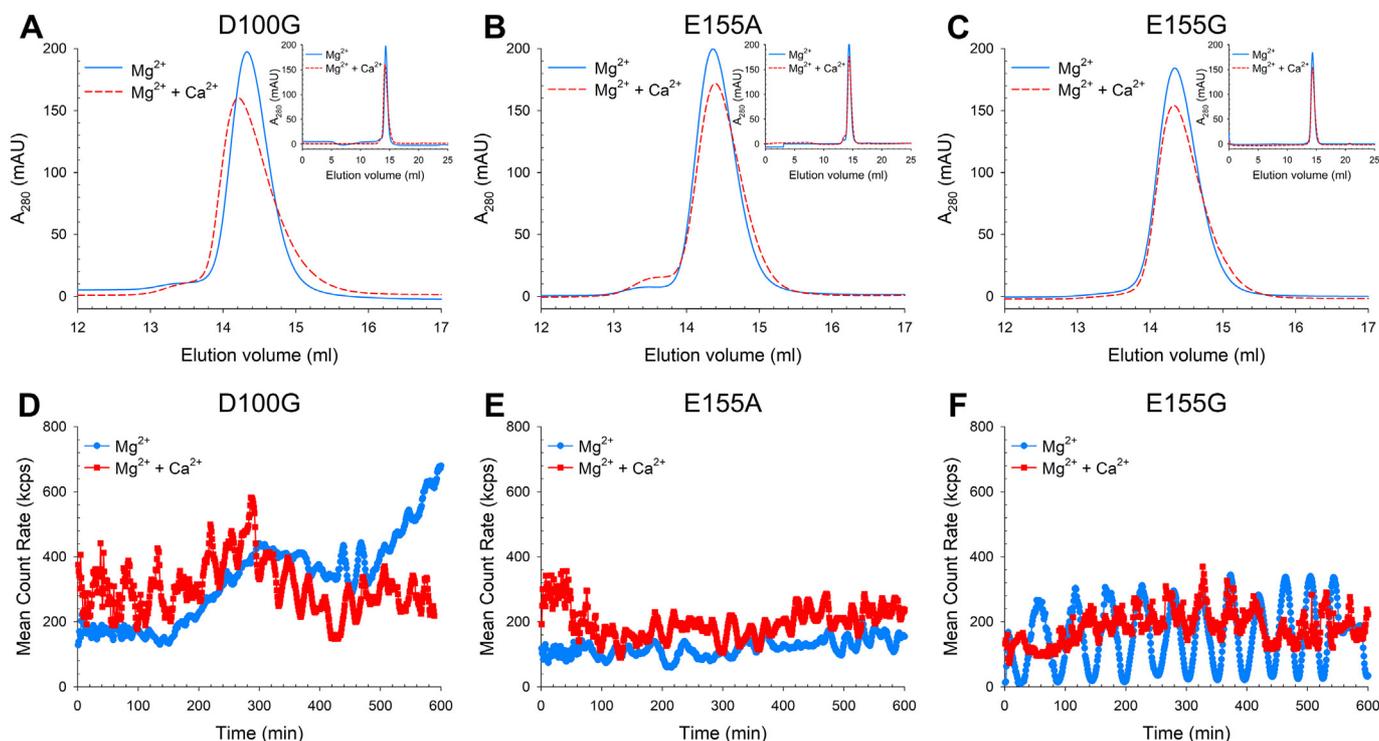


**Fig. 4.** Analytical gel filtration peaks of GCAP1 variants A) D100G, B) E155A and C) E155G in the presence of 500  $\mu M$  EGTA and 1 mM  $Mg^{2+}$  (blue, solid line) or 1 mM  $Mg^{2+}$  and 1 mM  $Ca^{2+}$  (red, dashed line). Insets show raw chromatograms. Mean count rate evolution over 10 h of GCAP1 variants D) D100G, E) E155A and F) E155G in the presence of 500  $\mu M$  EGTA and 1 mM  $Mg^{2+}$  (blue circles) or 1 mM  $Mg^{2+}$  and 1 mM  $Ca^{2+}$  (red squares).

other GCAP1 variant (7.8 nm in the presence of  $Mg^{2+}$  (p-value <  $10^{-19}$ ) and 8.8 nm in both  $Mg^{2+}$  and  $Ca^{2+}$  (p-value <  $10^{-16}$ ), that is 1.5 and 2 nm larger than WT GCAP1, respectively).

Time-resolved DLS experiments were run at 37 °C for at least 10 h to check for the stability of the colloidal dispersion and results are reported in Fig. 4D–F. Except for  $Mg^{2+}$ -D100G, which after an initially stable phase of ~180 min showed a bi-phasic, non-monotonic increase of MCR indicative of the formation of larger aggregates, none of the variants showed clear aggregation trends at the working concentration (30  $\mu$ M), although fluctuations were present in every case. In particular,  $Mg^{2+}$ -E155G (Fig. 4F) displayed unusually regular fluctuations of ~50 min periodicity over the ten-hour experimental time frame.

### 3.5. Multimeric assemblies of GCAP1 variants revealed by small angle X-ray scattering

To shed light on the untypical DLS profiles that suggest variations in the oligomeric state of GCAP1 variants, we performed SAXS experiments in the presence of saturating  $Mg^{2+}$  and  $Ca^{2+}$ . The scattering data of the 3 variants showed an estimated MW growing with the protein concentration, indicating a propensity of all the samples to form multimeric assemblies. In particular, D100G showed a MW compatible with dimer/trimer, E155A with trimer/tetramer, and E155G with monomer/dimer assemblies (Table 4). The scattering curves of D100G and E155A mutants at low protein concentrations (~65  $\mu$ M) displayed a similar trend (Guinier plot  $R_g = 34.2$  and  $36.0$  Å, respectively), with similar apparent trimeric assembly (MW Bayesian = 62.4 and 67.1 kDa, respectively), and with the respective Kratky plots indicating compact globular assemblies (maximum protein dimension,  $D_{max} \sim 115$  Å). On the contrary, the E155G mutant (at 26  $\mu$ M) showed a prevalent monomeric state (MW Bayesian = 21.2 kDa) with extended conformation (Guinier plot  $R_g = 30.4$  Å,  $D_{max} = 92$  Å), in line with a Kratky plot indicating a partially flexible protein. After calculating the particle distance distribution function  $P(r)$  (with scattering vector up to  $0.27$  Å<sup>-1</sup>) with the program *gnom* [47] we built different 3D models of the E155G monomer using the program *damcif* [48] (Ensemble Resolution  $36 \pm 3$  Å). One of the most representative models is shown in Fig. 5, ( $\chi^2 = 0.674$ ) superimposed to the crystal structure of chicken GCAP1 (pdb: 2r2i [37]) for comparison. The low resolution SAXS model of E155G displayed an extended conformation, different from the crystal structure of chicken GCAP1 (pdb 2r2i) and suggestive of a rather independent behavior of the 4 EF hands motifs. Such model pointed to a high level of perturbation of the protein fold likely induced by the E155G mutation.

**Table 4**  
SAXS data for GCAP1 CORD variants.

	Conc. [ $\mu$ M]	Bayesian Mw <sup>b</sup> [kDa]	$R_g$ (Guinier plot) [Å]	$R_g$ (from P (r)) [Å]	$D_{max}$ [Å]
D100G	32	55.6	$35.1 \pm 0.2$	34.3	104
	65	62.4	$34.2 \pm 0.2$	33.9	108
	137	62.4	$34.3 \pm 0.1$	33.7	106
	273	62.4	$34.9 \pm 0.2$	34.8	125
E155A	64	67.1	$36.0 \pm 0.2$	36.2	125
	129	76.4	$37.5 \pm 0.2$	38.7	139
	245	91.2	$38.5 \pm 0.1$	40.8	150
	449	94.2	$39.1 \pm 0.1$	40.3	130
E155G	26 <sup>a</sup>	21.2	$30.4 \pm 0.2$	29.8	92
	54 <sup>a</sup>	27.6	$31.4 \pm 0.1$	31.3	103
	109 <sup>a</sup>	27.6	$31.7 \pm 0.1$	32.8	115
	209 <sup>a</sup>	28.9	$34.3 \pm 0.1$	34.2	113

<sup>a</sup> These are estimations of the concentrations due to protein precipitation.

<sup>b</sup> See Ref. [46].

### 3.6. Protein flexibility and $Ca^{2+}$ -coordination investigated by molecular dynamics simulations

All-atom MD simulations spanning 1  $\mu$ s timeframe were run to investigate the dynamic properties of  $Ca^{2+}$ -loaded GCAP1 variants. The  $C\alpha$  root-mean square fluctuation (RMSF) index reports on the intrinsic protein flexibility over the simulated timeframe and permits precise comparisons between each variant at the level of individual amino acids and cation bound. A plot of the  $C\alpha$ -RMSF as a function of the residue number is reported in Fig. S3. The profile clearly shows that the EF3-EF4 motifs and their interconnecting regions overall constituting the C-terminal domain were significantly more flexible for E155A/G and D100G GCAP1 compared to WT GCAP1. No significant changes in flexibility were observed for the variants at the N-terminal domain, except for the  $\alpha$ N helix that displayed slightly increased flexibility in E155A-GCAP1 (Fig. S3, Fig. 6). Beside the transient helix  $\alpha$ T connecting EF3 with EF4, which showed intrinsically high flexibility in all GCAP1 variants (Fig. S3 and Fig. 6), major alterations in structural rigidity were detected in EF3 for D100G-GCAP1 (Fig. S3), which showed doubled RMSF in the EF3  $Ca^{2+}$ -binding loop compared to the WT, with subsequent increased mobility of the coordinated  $Ca^{2+}$  ion (Fig. 6). Interestingly, while the flexibility of the EF4  $Ca^{2+}$ -binding loop was similarly increased in E155A/G GCAP1, and the  $Ca^{2+}$  ion also showed higher mobility, both A/G substitutions in the EF4 bidentate cation coordinator also resulted in a significantly increased flexibility of the adjacent EF3 loop (Fig. S3, Fig. 6). Conversely, the D100G substitution in EF3 left the flexibility of the EF4 loop substantially unaltered.

MD simulations further permitted to quantitatively assess the distortion of the geometry of  $Ca^{2+}$ -coordination in EF3 and EF4 following amino acid substitutions. Fig. 7 (for numerical values see Tables ST1 and ST2) reports on the average distance between the  $C\alpha$  atoms of the 6 amino acids directly participating in  $Ca^{2+}$ -coordination in the canonical EF-hand via pentagonal bipyramidal oxygen-coordination. The analysis highlighted a significant geometrical perturbation of the EF3 cation binding loop in D100G mostly ascribable to a ~1 Å increase in the distance between E111 and D/G100, N104-/D108/E111 and D102/E111 (Table ST1). No significant alterations in the EF3 coordination geometry were observed for E155A and E155G GCAP1 compared to the WT (Table ST1, Fig. 7). The situation was different for EF4, where the largest structural distortions were observed. While the D100G substitution did not cause any significant alteration of the  $Ca^{2+}$  coordination geometry in EF4 (Table ST2), both E155A and E155G substitutions dramatically increased the distance between N146 and S152 above 3 Å and brought up to 4 Å that between N146 and E/G/A155 (Table ST2). Both substitutions led to prominent structural distortions, but the E155G mutation caused other average distances, beside those mentioned, to exceed 2 Å, namely that between D144 and E150 (2.4 Å vs 1.4 Å for E155A) and that between D144 and S152 (2.3 Å vs 1.7 Å for E155A). Overall, the E155G variant generated a larger distortion in the EF4 loop conformation, which resulted in a more opened-up  $Ca^{2+}$ -binding moiety compared to E155A (Fig. 6).

## 4. Discussion

GCAP1 has been associated with severe forms of COD-CORD but a recent work found that two patients diagnosed with retinitis pigmentosa reported mutations in the gene encoding for GCAP1, which altered the activation of the target GC, thus potentially expanding the association of GCAP1 to rod-cone dystrophies too [49]. It is reasonable to expect that mutations localized in the  $Ca^{2+}$ -binding loop may result in alteration of GCAP1 structural and functional properties that may reflect into alterations of target enzymatic activity, since GC1 per se is unable to sense  $Ca^{2+}$ , but it apparently integrates and processes information regarding  $Ca^{2+}$  sensing by GCAPs by its dimerization domain [50]. However, a thorough biochemical and biophysical investigation is necessary to elucidate differences among substitutions affecting the

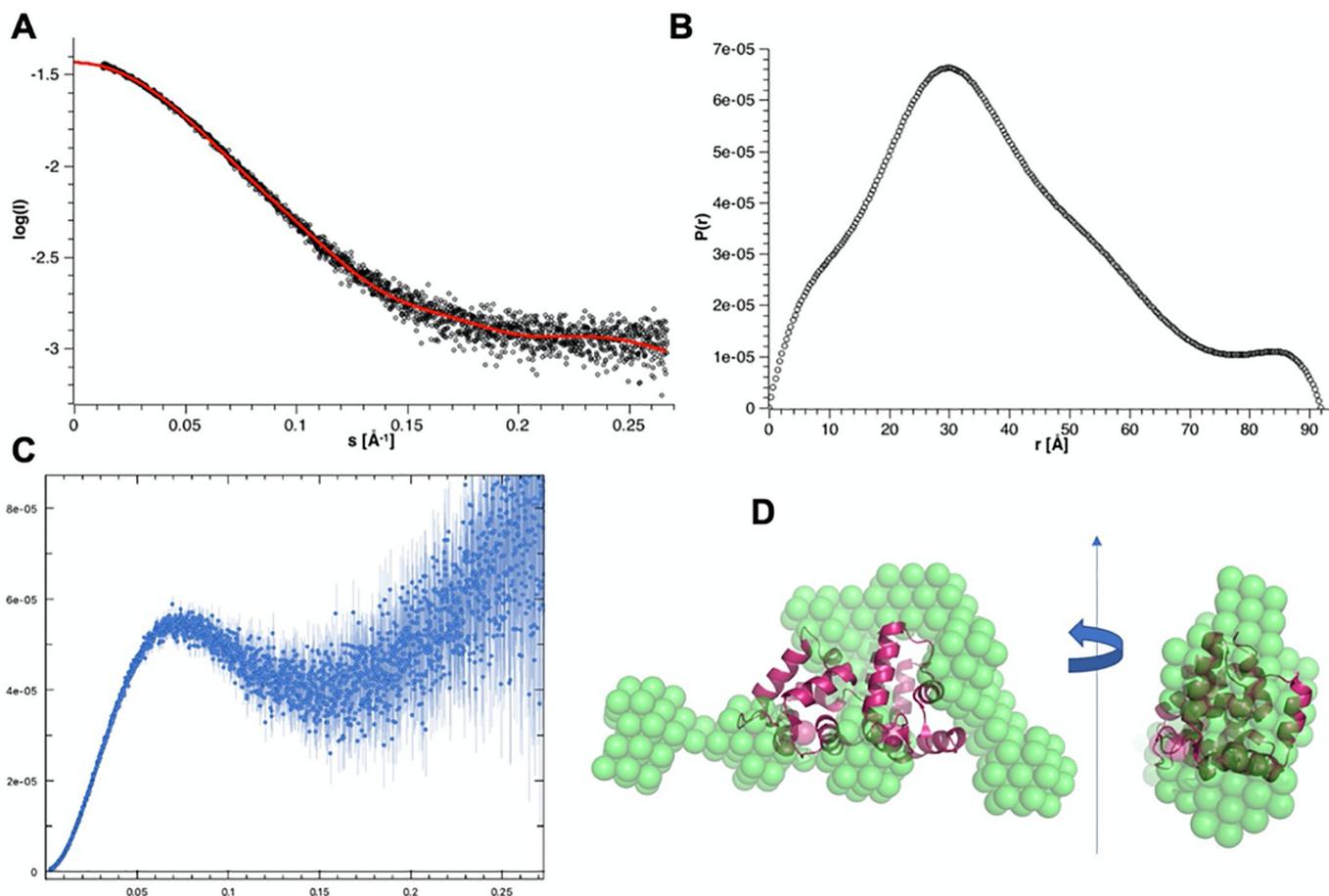


Fig. 5. SAXS data of E155G mutant: A) the scattering data (black circles) were analyzed with the program *gnom* (red curve) obtaining the B) distance distribution function  $P(r)$ ; C) Kratky plot showing a partially flexible structure; D) most representative low resolution model (in 2 orientations) obtained by *dammit* ( $\chi^2 = 0.674$ ; green spheres) superimposed to the crystal structure of WT chicken GCAP1 (purple cartoons) for comparison of overall dimensions.

highest (EF3) and lowest (EF4) affinity  $\text{Ca}^{2+}$ -binding sites [21].

Comparison of the target-regulatory capacity of the GCAP1 mutants affecting  $\text{Ca}^{2+}$ -coordination analyzed in this study indeed highlighted important differences. The virtually inexistent difference in GC1 X-fold activation between low and high  $\text{Ca}^{2+}$  levels displayed by D100G strongly suggests that the structural and functional integrity of EF3 is a crucial requirement for achieving GC1-inhibition, as initially demonstrated by Dizhoor and colleagues [8,9,51]. This is reflected by the dramatic loss of affinity for  $\text{Ca}^{2+}$  for this variant (Table 1), the highest among the three variants analyzed in this study. However, caution should be taken when inferring a direct correlation between GC1-dysregulation and loss in  $\text{Ca}^{2+}$  affinity since GCAP1 variants that have been characterized previously, namely L84F [27] and L176F [44] resulted in severe perturbation of GC1 catalytic activity without substantial alteration of  $\text{Ca}^{2+}$  binding.

While the D100G substitution essentially blocks the GC1 target in a constitutively active state, similarly to what was previously observed for the D100E substitution [20,52], it is interesting to notice that substituting the E155 residue with an alanine or a glycine resulted in a significantly different functional effect. Indeed, E155G GCAP1 resulted in enhanced activation of GC1 at low  $\text{Ca}^{2+}$  (Fig. 1), but the analysis of thermal denaturation data suggest that this variant was also the most unstable one among all the tested cation-bound states (Table 2); the binding of  $\text{Mg}^{2+}$  in particular did not increase protein stability, at odds with other variants.

Surprisingly, thermal denaturation studies showed that upon heating  $\text{Ca}^{2+}$ -bound E155G/A GCAP1 variants reached a  $\sim 1.5$ -fold higher level of unfolding compared to both WT and D100G variants

(Table 2), despite the latter mutant showed the largest decrease of affinity for  $\text{Ca}^{2+}$  (Table 1). Hence, there is no direct correlation between  $\text{Ca}^{2+}$  affinity and structural stability for these variants, and the structural effects induced by the e E155A/G mutations observed in near UV CD spectra (Fig. 3B and C) and highlighted by MD simulations (Fig. 5) rather point to a finer structural explanation. Indeed, substituting the side chain of E155, that is the twelfth residue participating in  $\text{Ca}^{2+}$ -coordination in EF4, causes the loss of the bidentate  $\text{Ca}^{2+}$  ligand which, by its carboxyl group, provides two of the seven oxygens that build up the pentagonal bipyramid geometry. Evidently, substitution of the bidentate  $\text{Ca}^{2+}$  ligand leads to a major structural destabilization, in line with the results from MD simulations. Interestingly, distortion of the EF4  $\text{Ca}^{2+}$  binding loop upon E155 substitution for A or G perturbed the flexibility of EF3 too (Fig. 6), but not its  $\text{Ca}^{2+}$  coordination geometry (Fig. 7, Table ST1). A similar result was recently observed for the E111V substitution in EF3 [12], where MD simulations suggested that replacing the bidentate  $\text{Ca}^{2+}$  ligand in EF3 enhances the flexibility of the adjacent EF4 loop too, in the absence of any other amino acid modification. Therefore, although  $\text{Ca}^{2+}$  binding to both bovine [20] and human [11,12] GCAP1 orthologs is sequential and occurs without cooperativity, EF3 and EF4 motifs appear to be joint by an allosteric communication mechanism mediated by their respective bidentate residues E111 and E155, which affect the mobility of the adjacent  $\text{Ca}^{2+}$  binding loop.

Binding of  $\text{Ca}^{2+}$  caused an increase in hydrodynamic diameter for all three GCAP1 variants as assessed by DLS (Fig. 4, Table 3) suggesting that all three variants are more compact in their  $\text{Mg}^{2+}$ -bound form, in line with what was previously observed for bovine GCAP1 [7]. The

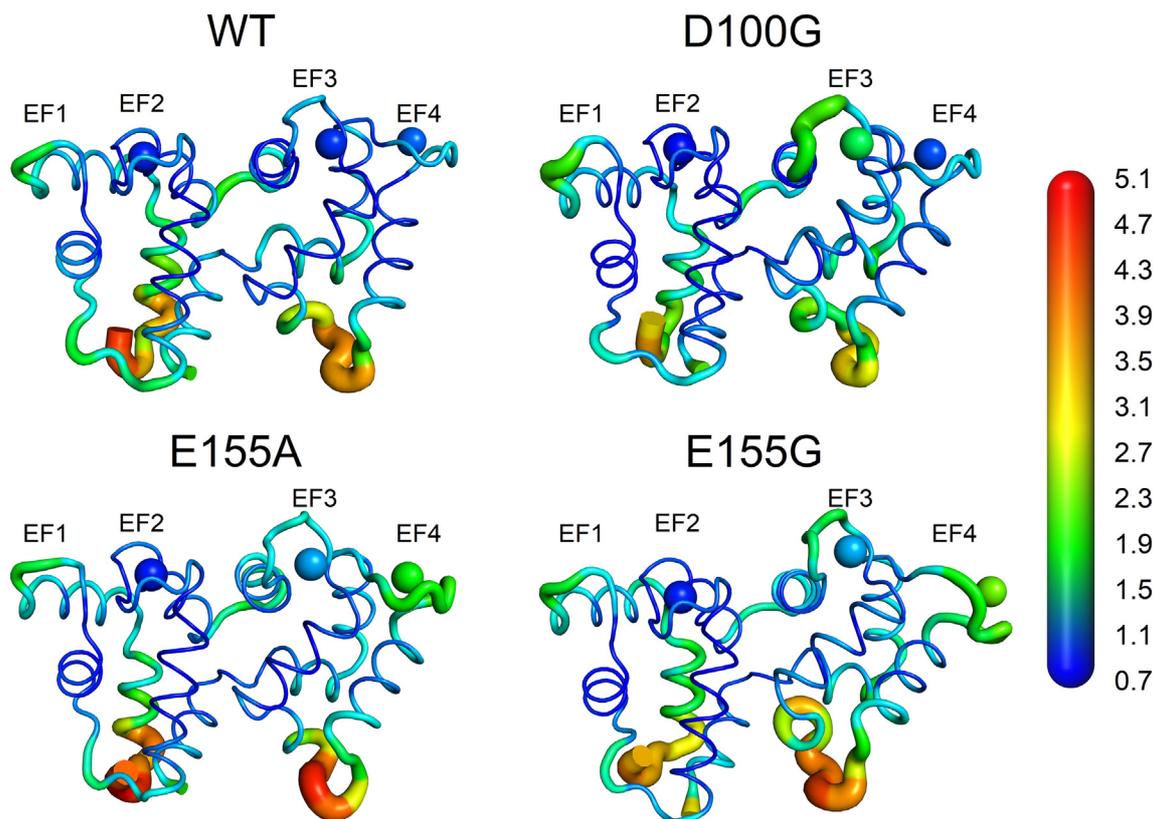


**Fig. 6.** Projection of the Root-Mean Square Fluctuation (RMSF) calculated on  $C\alpha$  over 1  $\mu$ s MD simulations on the three-dimensional structure of  $Ca^{2+}$ -loaded GCAP1 WT (top left), D100G (top right), E155A (bottom left), E155G (bottom right). Protein structure is shown as tubes with radius proportional to the RMSF,  $Ca^{2+}$  ions are represented as spheres. Proteins and ions are colored in a blue-to-red palette according to their RMSF, spanning between 0.7 and 5.1 Å (see Fig. S3).

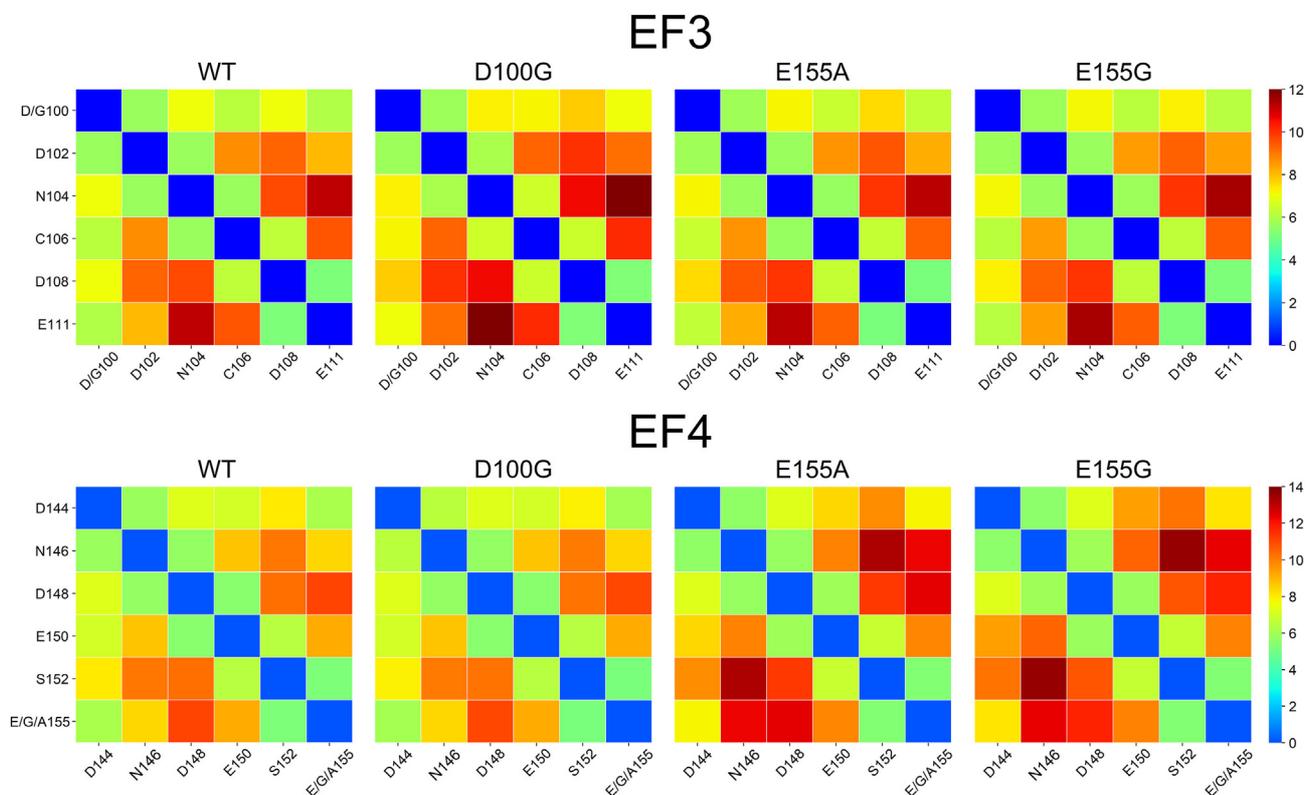


**Fig. 7.** Average distance between  $C\alpha$  of the residues involved in  $Ca^{2+}$ -coordination in EF3 (top panels) and EF4 (bottom panels) of  $Ca^{2+}$ -loaded GCAP1 WT, D100G, E155A and E155G (bottom right). The average distances (reported together with their standard deviation in Table ST1 and Table ST2, respectively) are calculated over 1  $\mu$ s MD trajectories and represented in a blue-to-red scale (0 to 12 Å and 0 to 14 Å, respectively).

significantly higher hydrodynamic size of E155A (Table 3) was in line with the larger rearrangement in the microenvironment of the aromatic residues observed in near UV CD spectra (Fig. 3B). Fluorescence experiments using the hydrophobic probe ANS (Fig. S2) suggest that the solvent accessible surface of this variant is particularly hydrophobic in all cation-bound states, with larger burial of hydrophobic residues in the GC1-activating ( $Mg^{2+}$ -bound) state. On the other hand, deleting the side chain in residue E155 by the E155G substitution rather exerted a dynamic distortion effect appreciable by the augmented flexibility of the  $Ca^{2+}$  binding loops as assessed by MD simulations (Fig. 6).

The SAXS data shown a tendency for all the mutants to form higher order quaternary assemblies beyond the monomer in the copresence of  $Mg^{2+}$  and  $Ca^{2+}$ , at increasing concentration. This evidence was more pronounced for E155A and to a minor extent for D100G and E155G. At low protein concentration the SAXS data indicated for the E155G monomer a highly dynamical structure compatible with a semi-independent behavior of the four EF hand motifs. Such structure could be the ultimate result of the initial fold perturbation showed by the RMSF analysis of MD simulation data, which refers to a shorter timeframe.

We can also speculate that the unequal tendency to form higher order quaternary assemblies could be related to different levels of structural perturbation induced by the mutations. Following this reasoning, despite the similarity in the two scattering curves, we could assign a higher level of structural perturbation to the E155A mutant than to the D100G mutant.

## 5. Conclusions

In conclusion, all three CORD-associated GCAP1 variants led to severe alteration of GC1 catalytic activity, blocking the enzyme in a constitutively active state, a characteristic that was observed in all COD/CORD GCAP1 variants analyzed so far [17,18]. The permanent synthesis of cGMP in the absence of light stimulus can lead to a dysregulation of the second messenger homeostasis and thus trigger cell death as a result of both increased levels of cGMP and/or increased levels of intracellular  $Ca^{2+}$  [53,54] as a consequence of the unphysiological opening of CNG channels [17]. On a more general note, this work confirms the fundamental role of  $Ca^{2+}$ -coordination in ensuring the optimal structural/functional switch of GCAP1 from GC1-inhibitor to activator state and shows that individual amino acid substitutions can lead to significantly altered functionality. Moreover, when analyzed together with the previously characterized E111V variant [12] our data on E155A/G substitutions suggest that beside the expected local effects, mutation of the bidentate glutamate in an EF-hand calcium binding motif can profoundly perturb the flexibility of the adjacent EF-hand as well, ultimately destabilizing the whole domain. This interesting finding could have general implications for calcium sensor proteins, whose ability to regulate intracellular targets ultimately depends on the integrity of the structural switch mechanism induced by  $Ca^{2+}$ -binding.

## Abbreviations

cGMP	guanosine 3',5'-cyclic monophosphate
GC1	guanylate cyclase 1
GCAP	guanylate cyclase-activating protein
COD	cone dystrophies
CORD	cone-rod dystrophies
RPE	retinal pigmented epithelium
yNMT	N-myristoyl-transferase from <i>S. cerevisiae</i>
IB	inclusion bodies
SEC	size exclusion chromatography
AEC	anionic-exchange chromatography
TRIS	tris(hydroxymethyl)aminomethane
DTT	dithiothreitol
DLS	dynamic light scattering

EGTA	ethyleneglycoltetraacetic acid
MCR	mean count rate
SDS-PAGE	sodium dodecylsulphate polyacrylamide gel electrophoresis
EDTA	ethylenediaminetetraacetic acid
Br <sub>2</sub> -BAPTA	5,5'-Dibromo-1,2-bis(2-aminophenoxy)ethane-N,N,N',N'-tetraacetic acid
CD	circular dichroism
ANS	8-Anilinonaphthalene-1-sulfonic acid
DMSO	dimethyl sulfoxide
MD	molecular dynamics
RMSF	Root-Mean Square Fluctuation
WT	wild type
SAXS	Small Angle X-ray Scattering

## CRedit authorship contribution statement

**Giuditta Dal Cortivo**:Data curation, Formal analysis, Investigation, Visualization, Writing - review & editing.**Valerio Marino**:Data curation, Formal analysis, Investigation, Visualization, Writing - review & editing.**Francesco Boni**:Investigation, Data curation, Writing - review & editing.**Mario Milani**:Supervision, Formal analysis, Funding acquisition, Writing - review & editing.**Daniele Dell'Orco**:Conceptualization, Formal analysis, Funding acquisition, Writing - review & editing, Writing - original draft.

## Declaration of competing interest

The authors declare that they have no known competing financial interests or personal relationships that could have appeared to influence the work reported in this paper.

## Acknowledgements

We would like to acknowledge Centro Piattaforme Tecnologiche of the University of Verona for providing access to the spectroscopic and computational facilities. We would like to thank Diamond LightSource for beamtime (proposal mx20221), and the staff of beamline B21 (and in particular Dr. Katsuki Inoue) for assistance in SAXS data collection.

This work was funded by a grant from Fondazione Telethon-Italy (grant no. GGP16010 to DDO and MM).

## Appendix A. Supplementary information

Supplementary information to this article can be found online at <https://doi.org/10.1016/j.bbamcr.2020.118794>.

## References

- [1] E.J. Pugh, T. Lamb, Phototransduction in vertebrate rods and cones: molecular mechanisms of amplification, recovery and light adaptation, in: D. Stavenga, W. DeGrip, E.J. Pugh (Eds.), Handbook of Biological Physics, Elsevier Science BV, Place Published, 2000, pp. 183–255.
- [2] K.W. Koch, D. Dell'Orco, Protein and signaling networks in vertebrate photoreceptor cells, *Front. Mol. Neurosci.* 8 (2015) 67.
- [3] K.W. Koch, D. Dell'Orco, A calcium-relay mechanism in vertebrate phototransduction, *ACS Chem. Neurosci.* 4 (2013) 909–917.
- [4] K.W. Koch, T. Duda, R.K. Sharma,  $Ca^{2+}$ -modulated vision-linked ROS-GC guanylate cyclase transduction machinery, *Mol. Cell. Biochem.* 334 (2010) 105–115.
- [5] D. Sharon, H. Wimberg, Y. Kinarty, K.W. Koch, Genotype-functional-phenotype correlations in photoreceptor guanylate cyclase (GC-E) encoded by GUCY2D, *Prog. Retin. Eye Res.* 63 (2018) 69–91.
- [6] D. Dell'Orco, S. Sulmann, S. Linse, K.W. Koch, Dynamics of conformational  $Ca^{2+}$ -switches in signaling networks detected by a planar plasmonic device, *Anal. Chem.* 84 (2012) 2982–2989.
- [7] V. Marino, S. Sulmann, K.W. Koch, D. Dell'Orco, Structural effects of  $Mg^{2+}$  on the regulatory states of three neuronal calcium sensors operating in vertebrate phototransduction, *Biochim. Biophys. Acta* 1853 (2015) 2055–2065.
- [8] I.V. Peshenko, A.M. Dizhoor, Guanylyl cyclase-activating proteins (GCAPs) are

- Ca<sup>2+</sup>/Mg<sup>2+</sup> sensors: implications for photoreceptor guanylyl cyclase (RetGC) regulation in mammalian photoreceptors, *J. Biol. Chem.* 279 (2004) 16903–16906.
- [9] I.V. Peshenko, A.M. Dizhoor, Ca<sup>2+</sup> and Mg<sup>2+</sup> binding properties of GCAP-1. Evidence that Mg<sup>2+</sup>-bound form is the physiological activator of photoreceptor guanylyl cyclase, *J. Biol. Chem.* 281 (2006) 23830–23841.
- [10] A.M. Dizhoor, E.V. Olshevskaya, I.V. Peshenko, Mg<sup>2+</sup>/Ca<sup>2+</sup> cation binding cycle of guanylyl cyclase activating proteins (GCAPs): role in regulation of photoreceptor guanylyl cyclase, *Mol. Cell. Biochem.* 334 (2010) 117–124.
- [11] S. Abbas, V. Marino, L. Bielefeld, K.W. Koch, D. Dell'Orco, Constitutive activation of guanylate cyclase by the G86R GCAP1 variant is due to "locking" cation- $\pi$  interactions that impair the activator-to-inhibitor structural transition, *Int J Mol Sci* 21 (2020).
- [12] V. Marino, G. Dal Cortivo, E. Oppici, P.E. Maltese, F. D'Esposito, E. Manara, L. Ziccardi, B. Falsini, A. Magli, M. Bertelli, D. Dell'Orco, A novel p.(Glu111Val) missense mutation in GUCA1A associated with cone-rod dystrophy leads to impaired calcium sensing and perturbed second messenger homeostasis in photoreceptors, *Hum. Mol. Genet.* 27 (2018) 4204–4217.
- [13] I.V. Peshenko, A.V. Cideciyan, A. Sumaroka, E.V. Olshevskaya, A. Scholten, S. Abbas, K.W. Koch, S.G. Jacobson, A.M. Dizhoor, A G86R mutation in the calcium-sensor protein GCAP1 alters regulation of retinal guanylyl cyclase and causes dominant cone-rod degeneration, *J. Biol. Chem.* 294 (2019) 3476–3488.
- [14] D. Dell'Orco, G. Dal Cortivo, Normal GCAPs partly compensate for altered cGMP signaling in retinal dystrophies associated with mutations in GUCA1A, *Sci. Rep.* 9 (2019) 20105.
- [15] S. Lopez-Begines, A. Plana-Bonamaiso, A. Mendez, Molecular determinants of guanylate cyclase activating protein subcellular distribution in photoreceptor cells of the retina, *Sci. Rep.* 8 (2018) 2903.
- [16] N. Lopez-del Hoyo, L. Fazioli, S. Lopez-Begines, L. Fernandez-Sanchez, N. Cuenca, J. Llorens, P. de la Villa, A. Mendez, Overexpression of guanylate cyclase activating protein 2 in rod photoreceptors in vivo leads to morphological changes at the synaptic ribbon, *PLoS One* 7 (2012) e42994.
- [17] P. Behnen, D. Dell'Orco, K.W. Koch, Involvement of the calcium sensor GCAP1 in hereditary cone dystrophies, *Biol. Chem.* 391 (2010) 631–637.
- [18] L. Jiang, W. Baehr, GCAP1 mutations associated with autosomal dominant cone dystrophy, *Adv. Exp. Med. Biol.* 664 (2010) 273–282.
- [19] G. Manes, S. Mamouni, E. Herald, A.C. Richard, A. Senechal, K. Aouad, B. Bocquet, I. Meunier, C.P. Hamel, Cone dystrophy or macular dystrophy associated with novel autosomal dominant GUCA1A mutations, *Mol. Vis.* 23 (2017) 198–209.
- [20] D. Dell'Orco, P. Behnen, S. Linse, K.W. Koch, Calcium binding, structural stability and guanylate cyclase activation in GCAP1 variants associated with human cone dystrophy, *Cell. Mol. Life Sci.* 67 (2010) 973–984.
- [21] S. Lim, I. Peshenko, A. Dizhoor, J.B. Ames, Effects of Ca<sup>2+</sup>, Mg<sup>2+</sup>, and myristoylation on guanylyl cyclase activating protein 1 structure and stability, *Biochemistry* 48 (2009) 850–862.
- [22] S.M. Gagne, M.X. Li, B.D. Sykes, Mechanism of direct coupling between binding and induced structural change in regulatory calcium binding proteins, *Biochemistry* 36 (1997) 4386–4392.
- [23] E. Nong, W. Lee, J.E. Merriam, R. Allikmets, S.H. Tsang, Disease progression in autosomal dominant cone-rod dystrophy caused by a novel mutation (D100G) in the GUCA1A gene, *Doc. Ophthalmol.* 128 (2014) 59–67.
- [24] S.E. Wilkie, Y. Li, E.C. Deery, R.J. Newbold, D. Garibaldi, J.B. Bateman, H. Zhang, W. Lin, D.J. Zack, S.S. Bhattacharya, M.J. Warren, D.M. Hunt, K. Zhang, Identification and functional consequences of a new mutation (E155G) in the gene for GCAP1 that causes autosomal dominant cone dystrophy, *Am. J. Hum. Genet.* 69 (2001) 471–480.
- [25] L. Huang, S. Li, X. Xiao, X. Jia, W. Sun, Y. Gao, L. Li, P. Wang, X. Guo, Q. Zhang, Novel GUCA1A mutation identified in a Chinese family with cone-rod dystrophy, *Neurosci. Lett.* 541 (2013) 179–183.
- [26] J.Y. Hwang, K.W. Koch, Calcium- and myristoyl-dependent properties of guanylate cyclase-activating protein-1 and protein-2, *Biochemistry* 41 (2002) 13021–13028.
- [27] V. Marino, A. Scholten, K.W. Koch, D. Dell'Orco, Two retinal dystrophy-associated missense mutations in GUCA1A with distinct molecular properties result in a similar aberrant regulation of the retinal guanylate cyclase, *Hum. Mol. Genet.* 24 (2015) 6653–6666.
- [28] M.M. Bradford, A rapid and sensitive method for the quantitation of microgram quantities of protein utilizing the principle of protein-dye binding, *Anal. Biochem.* 72 (1976) 248–254.
- [29] R. Vallone, G. Dal Cortivo, M. D'Onofrio, D. Dell'Orco, Preferential binding of Mg<sup>2+</sup> over Ca<sup>2+</sup> to CIB2 triggers an allosteric switch impaired in usher syndrome type 1J, *Front. Mol. Neurosci.* 11 (2018) 274.
- [30] V. Marino, A. Borsatto, F. Vocke, K.W. Koch, D. Dell'Orco, CaF<sub>2</sub> nanoparticles as surface carriers of GCAP1, a calcium sensor protein involved in retinal dystrophies, *Nanoscale* 9 (2017) 11773–11784.
- [31] P.V. Konarev, V.V. Volkov, A.V. Sokolova, M.H.J. Koch, D.I. Svergun, PRIMUS: a windows PC-based system for small-angle scattering data analysis, *J. Appl. Crystallogr.* 36 (2003) 1277–1282.
- [32] D. Franke, M.V. Petoukhov, P.V. Konarev, A. Panjkovich, A. Tuukkanen, H.D.T. Mertens, A.G. Kikhney, N.R. Hajizadeh, J.M. Franklin, C.M. Jeffries, D.I. Svergun, ATASAS 2.8: a comprehensive data analysis suite for small-angle scattering from macromolecular solutions, *J. Appl. Cryst.* 50 (2017) 1212–1225.
- [33] J.Y. Hwang, C. Lange, A. Helten, D. Hoppner-Heitmann, T. Duda, R.K. Sharma, K.W. Koch, Regulatory modes of rod outer segment membrane guanylate cyclase differ in catalytic efficiency and Ca<sup>2+</sup>-sensitivity, *Eur. J. Biochem.* 270 (2003) 3814–3821.
- [34] J. Viviano, A. Krishnan, H. Wu, V. Venkataraman, Electrophoretic mobility shift in native gels indicates calcium-dependent structural changes of neuronal calcium sensor proteins, *Anal. Biochem.* 494 (2016) 93–100.
- [35] S. Linse, Calcium binding to proteins studied via competition with chromophoric chelators, *Methods Mol. Biol.* 173 (2002) 15–24.
- [36] I. Andre, S. Linse, Measurement of Ca<sup>2+</sup>-binding constants of proteins and presentation of the Caligator software, *Anal. Biochem.* 305 (2002) 195–205.
- [37] R. Stephen, G. Bereta, M. Golczak, K. Palczewski, M.C. Sousa, Stabilizing function for myristoyl group revealed by the crystal structure of a neuronal calcium sensor, guanylate cyclase-activating protein 1, *Structure* 15 (2007) 1392–1402.
- [38] M.J. Abraham, T. Murtola, R. Schulz, S. Páll, J.C. Smith, B. Hess, E. Lindahl, GROMACS: high performance molecular simulations through multi-level parallelism from laptops to supercomputers, *SoftwareX* 1 (2015) 19–25.
- [39] J. Huang, S. Rauscher, G. Nawrocki, T. Ran, M. Feig, B.L. de Groot, H. Grubmüller, A.D. MacKerell Jr., CHARMM36m: an improved force field for folded and intrinsically disordered proteins, *Nat. Methods* 14 (2017) 71–73.
- [40] V. Marino, D. Dell'Orco, Allosteric communication pathways routed by Ca<sup>2+</sup>/Mg<sup>2+</sup> exchange in GCAP1 selectively switch target regulation modes, *Sci. Rep.* 6 (2016) 34277.
- [41] V. Marino, D. Dell'Orco, Evolutionary-conserved allosteric properties of three neuronal calcium sensor proteins, *Front. Mol. Neurosci.* 12 (2019) 50.
- [42] A. Astegno, V. La Verde, V. Marino, D. Dell'Orco, P. Dominici, Biochemical and biophysical characterization of a plant calmodulin: role of the N- and C-lobes in calcium binding, conformational change, and target interaction, *Biochim. Biophys. Acta* 1864 (2016) 297–307.
- [43] S. Sulmann, D. Dell'Orco, V. Marino, P. Behnen, K.W. Koch, Conformational changes in calcium-sensor proteins under molecular crowding conditions, *Chemistry* 20 (2014) 6756–6762.
- [44] F. Vocke, N. Weisschuh, V. Marino, S. Malfatti, S.G. Jacobson, C.M. Reiff, D. Dell'Orco, K.W. Koch, Dysfunction of cGMP signalling in photoreceptors by a macular dystrophy-related mutation in the calcium sensor GCAP1, *Hum. Mol. Genet.* 26 (2017) 133–144.
- [45] S. Lim, G. Roseman, I. Peshenko, G. Manchala, D. Cudia, A.M. Dizhoor, G. Millhauser, J.B. Ames, Retinal guanylyl cyclase activating protein 1 forms a functional dimer, *PLoS One* 13 (2018) e0193947.
- [46] N.R. Hajizadeh, D. Franke, C.M. Jeffries, D.I. Svergun, Consensus Bayesian assessment of protein molecular mass from solution X-ray scattering data, *Sci. Rep.* 8 (2018) 7204.
- [47] D.I. Svergun, Determination of the regularization parameter in indirect-transform methods using perceptual criteria, *J. Appl. Crystallogr.* 25 (1992) 495–503.
- [48] D. Franke, D.I. Svergun, DAMMIF, a program for rapid ab-initio shape determination in small-angle scattering, *J. Appl. Crystallogr.* 42 (2009) 342–346.
- [49] S. Abbas, V. Marino, N. Weisschuh, S. Kieninger, M. Solaki, D. Dell'Orco, K.W. Koch, Neuronal calcium sensor GCAP1 encoded by GUCA1A exhibits heterogeneous functional properties in two cases of retinitis pigmentosa, *ACS Chem Neurosci* 11 (10) (2020) 1457–1470.
- [50] P. Zagel, D. Dell'Orco, K.W. Koch, The dimerization domain in outer segment guanylate cyclase is a Ca<sup>2+</sup>-sensitive control switch module, *Biochemistry* 52 (2013) 5065–5074.
- [51] I.V. Peshenko, A.M. Dizhoor, Activation and inhibition of photoreceptor guanylyl cyclase by guanylyl cyclase activating protein 1 (GCAP-1): the functional role of Mg<sup>2+</sup>/Ca<sup>2+</sup> exchange in EF-hand domains, *J. Biol. Chem.* 282 (2007) 21645–21652.
- [52] V.B. Kitiratschky, P. Behnen, U. Kellner, J.R. Heckenlively, E. Zrenner, H. Jagle, S. Kohl, B. Wissinger, K.W. Koch, Mutations in the GUCA1A gene involved in hereditary cone dystrophies impair calcium-mediated regulation of guanylate cyclase, *Hum. Mutat.* 30 (2009) E782–E796.
- [53] M. Kulkarni, D. Trifunovic, T. Schubert, T. Euler, F. Paquet-Durand, Calcium dynamics change in degenerating cone photoreceptors, *Hum. Mol. Genet.* 25 (2016) 3729–3740.
- [54] M. Power, S. Das, K. Schütze, V. Marigo, P. Ekstrom, F. Paquet-Durand, Cellular mechanisms of hereditary photoreceptor degeneration - Focus on cGMP, *Prog Retin Eye Res* (2019) 100772.